Study of Bound State QED :

Precision Measurement

of

the Orthopositronium Decay Rate

Ph. D. thesis

Osamu Jinnouchi

March 2001

Department of Physics
Faculty of Science, University of Tokyo

Abstract

This thesis reports a new precise measurement of the vacuum decay rate of ortho-positronium, $\lambda_{\text{o-Ps}}$. The measurements have been carried out with two different types of SiO_2 powder, yielding a consistent result with each other. The combined value is $\lambda_{\text{o-Ps}} = 7.0396 \pm 0.0012(stat.) \pm 0.0011(sys.)\ \mu s^{-1}$, where the first error is the statistical error, and the second represents the systematic error.

The new value is consistent with the theoretical QED prediction. The obtained value favors non-logarithmic $O(\alpha^2)$-corrected value which is recently calculated using nonrelativistic quantum electrodynamics (NRQED), rather than the value corrected up to $O(\alpha)$.

The present result agrees well and 1.8 times more precise than the previous measurement in 1995 that utilizing the SiO_2 powder, and significantly disagrees with the other high precision gas and cavity measurements by 5.6 σ and 3.8 σ discrepancy.

When you have eliminated
all which is impossible,
then whatever remains,
however improbable,
must be the truth.

Sherlock Holmes,
The Adventure of The Blanched Soldier

Acknowledgements

First, I would like to express my gratitude to Prof. Tomio Kobayashi (ICEPP Univ. of Tokyo) for providing me with this work. Without his continuous encouragement and warm guidance, I could not have finished this study.

I would like to acknowledge the late Prof. Shuji Orito for giving me the chance that I should take over this work. The studies relating to the orthopositronium lifetime measurements had been the theme of his research group.

I would like to thank Prof. Toshio Hyodo (Univ. of Tokyo), Dr. Yasuyuki Nagashima (Univ. of Tokyo) and Dr. Haruo Saito for their useful suggestions and information on the o-Ps properties, especially on the o-Ps thermalization and Stark shift.

I gratefully acknowledge Masahiro Ikeno (KEK) and Osamu Sasaki (KEK) for provinding us a new special TDCs, the high-performance and the stability of it were the most important key for the success of this experiment.

In particular I would like to thank Masami Chiba (Tokyo Metropolitan Univ.) for many useful information and discussions on the o-Ps decay rate.

I would like to express sincere gratitude to A. Kohinata and T. Mizutani (Nippon Aerosil Ltd.) for the generous supply of the silica powders and for their valuable information about the characters of the products. I would also like to thank Yusuke Imajyo (SEIKO EG & G) for supporting this work from the beginning, namely the design of the setups, especially the NaI(Tl) detectors. Sincere gratitude is expressed to T. Yamada and M. Matsumoto (Japan Radioisotope Association) for the preparation of the several gamma-ray sources and the positron sources.

I would like to thank all the people of International Center for Elementary Particle Physics (ICEPP) at University of Tokyo, Sachio Komamiya, Toshinori Mori, Tetsuro Mashimo, Satoshi Mihara, Wataru Ootani and Jun Yashima, for their useful suggestions and encouragement.

Thanks also go to Mitsuhiro Yoshida, Daisuke Toya, Yuuichi Katori, Hajime Nanjyo, Hajime Nishiguchi, Takehiro Nagashima and Yoshio Nakamura, for many discussions and joyful research life. I specially thank Kenji Ozone; he administers our computational environment and always introduce a brand new Linux system. Thanks to the people who is now working in another place, Kensuke Homma (Hiroshima Univ.), Soushi Tsuno (Tsukuba

Univ.), Kouji Satou (Tsukuba Univ.), Satoshi Matsuura (Fujitsu) and Taichi Niki (Sony). I couldn't enjoy my research life without them. Thanks to all members of the secretarial staffs for their kindly support. Great thanks go to Reiko Yahata, Yuko Nozaki and Makiko Shioya for their official support for my research and for their warmhearted encouragement.

Special thanks go to Kazumi Hasuko for giving me the many experimental knowledge, and sparing his time for proofreading of this thesis.

I would like to especially thank Koji Yoshimura, he taught me how the researchers can enjoy his work throughout his life. Also we discuss about the positronium for many times.

I would also like to thank Andrzej Czarnecki for our good friendship. He visited ICEPP when he had just finished his calculations of the p-Ps decay rate. I've learned a great deal talking with him.

I wish to express my great appreciation to Shoji Asai for his continuous assistance and guidance at this work. He wrote his Ph. D. thesis in 1995, and I took over his work. I've learned a lot from him, not to mention about the positronium, whole knowledge as to the experimental physics.

Great gratitude goes to my parents, Raizo and Kuniyo Jinnouchi, and elder brother Tsuyoshi and younger sister Megumi for their continuous encouragement and appreciation to my research life.

Finally I thank my wife, Miho, for all her love and support.

Contents

List of Figures

List of Tables

Chapter 1

Introduction

The study of hydrogen-like systems has played a major role in the modern physics, especially in the development of Quantum ElectroDynamics (QED). The main concern has changed from the basic understanding of the spectrum in terms of the quantum mechanics, through refinements such as relativistic, spin orbit, and QED contributions, and finally reached the precision test of relativistic two-body system, such as positronium, muonium, and quarkonium.

High precision calculations of the QED in bound state system are quite different from that of the free particles. The renormalization theory in QED for free particle system is a perfectly well-defined procedure by expanding in terms of the number of photons, except its complex and lengthy characteristics at its implementation. It requires refinements in perturbative analysis.

On the other hand, precision calculations of nonrelativistic bound state physics are essentially nonperturbative. Although they involves kernels which can be written in terms of Feynman diagrams, the fine structure constant α's enter the wave functions and the particle propagators in a nonperturbative way. Thus one cannot simply count powers of α in a given kernel in order to determine its ultimate contribution to the calculation. Typically, a kernel includes some leading order terms accompanying an infinite series of smaller terms. Therefore, in the bound state calculation there is no simple correlation between the importance of an amplitude and the number of photons. The kernels can often be grouped together in such a way that their leading order terms cancels. Thus it is important to note that the formal development of bound state theory is not at all mechanical, and there are many routes to a correct answer.

Fortunately, the ultimate work involved in algebra and integrals is order of magnitude simpler than that of the perturbative calculation of the free particle such as the electron $g-$factor. This is because most calculations of the bound state physics are two-loop level at most, instead of four-loop level of free particle.

In spite of the fact that the bound state theory is nonperturbative, it is possible to make use of small parameter such as α to develop expression in increasing order of smallness. Recent development of this nonrelativistic effective field theory, called nonrelativistic quantum electrodynamics (NRQED), enables the calculations of the bound state system.

Positronium (Ps), an electron-positron bound state, offers unique opportunities for testing our understanding of bound states in the framework of NRQED. Because its constituents are much lighter than any other known charged particles such as muons, or pions by a factor of about 200, the spectrum and the decay rate of positronium can be calculated with very high precision. Therefore comparison of theoretical predictions with experimental values gives an opportunity to test the validity of this effective theory with high accuracy.

Ground states of Ps can be classified into two states depending on the sum of spins of the electron and positron; parapositronium (p-Ps) with total spin 0, and orthopositronium (o-Ps), which is a triplet with total spin 1. The p-Ps is slightly lighter than o-Ps owing to the spin-spin interaction, and this difference of masses yields the splitting in spectroscopy. One of the most accurate tests of bound state theory is a measurement of this hyperfine splitting (HFS). Other high precision energy interval measurements are reviewed in [1].

Other quantities which can be measured with high precision are the decay rates of positronium in singlet and triplet ground-states, e.g. p-Ps and o-Ps. For p-Ps the most recent result [2] is in good agreement with the latest calculation [3] which involves up to $O(\alpha^2)$ radiative corrections. On the other hand, the situation for o-Ps is not clear. The most reliable calculation of the o-Ps decay rate has been finished recently in the framework of NRQED [4] up to an order α^2,

$$\lambda_{\text{o-Ps}}^{\text{theory}} = 7.039\ 934(10)\ \mu s^{-1}, \tag{1.1}$$

where result is obtained in 1.4-*ppm* accuracy. Nevertheless there are other activities which varies from the former result indicating about 70-*ppm* level uncertainty on the theoretical side.

Experimentally, the situation is not clear either. Precise experiments of the Ann Arbor group found,

$$\lambda_{\text{o-Ps}}^{\text{exp}}\ (\text{gas measurement}) = 7.0514(14)\ \mu s^{-1}\ [5], \tag{1.2}$$

$$\lambda_{\text{o-Ps}}^{\text{exp}}\ (\text{vacuum measurement}) = 7.0482(16)\ \mu s^{-1}\ [6], \tag{1.3}$$

which differ from Eq. (1.1) by 8.2 σ and 5.2 σ respectively. This discrepancy between the theory and experiments has been known as the 'orthopositronium lifetime puzzle.' Nevertheless the somewhat less precise Tokyo measurement,

$$\lambda^{\rm exp}_{\text{o-Ps}}\ (\mathrm{SiO_2}\ \text{measurement}) = 7.0398(29)\ \mu s^{-1}\ [7], \tag{1.4}$$

agrees well with the theoretical prediction, and differs from the former experiments by 4.0 σ and 2.9 σ. This measurement took directly the thermalization effect of o-Ps into account for the first time; now that the main systematic problems in the previous measurements are believed to be related to the thermalization. However there has been some practical difficulties in a timing system of the Tokyo group, and the error size of about 400 *ppm* derives no information as to the $O(\alpha^2)$ contribution from the NRQED.

In this context, it is strongly desired to carry out a new measurement which perfectly takes the thermalization effect into account and also reduce the experimental error to about 200-*ppm* level. In this thesis, the new precision measurements of the decay rate of orthopositronium will be described; the timing system is drastically improved from the last measurement [7]. This improvement makes it possible to discuss over the $O(\alpha^2)$ contribution in the framework of NRQED.

This thesis is organized as follows. Chapter 2 contains an overview of the bound state QED physics, especially on the positronium which is the main theme of the thesis. The theoretical descriptions of p-Ps and o-Ps follows, then the historical problems relating to the decay rate of orthopositronium is discussed. Chapter 3 describes the experiment. At first technical background of the present measurement is described, then the detailes of the experimental apparatus follows. Also the Monte Carlo simulation used in the analysis is explained there. Chapter 4 provides the data analysis. The calibration of the detectors, the procedures of the analysis are explained in detail. The results of the analysis, estimation of the varieties of systematic errors are discussed as well. Finally in Chapter 5, the results of analysis and the estimation of the systematic errors are summarized. The experimental results are presented there.

Chapter 2

Physics

This chapter provides a brief review of the bound state QED physics. The main focus is on the positronium, the bound state of e^- and e^+. An overview of the historical problem relating to the decay rate measurement of ortho-positronium will follow.

2.1 Positronium

Positronium (Ps), the bound state of the electron (e^-) and the positron (e^+) is a pure leptonic state. Since it is effectively free from hadronic and weak interaction effects, and bound purely by the electromagnetic interaction, Ps is considered as the best testing ground for QED, in particular, for studying the relativistic and non-relativistic bound state formalism in quantum field theory.

2.1.1 Overview of Positronium Properties

The Ps consists of two fermions like hydrogen atom, and the Ps wave functions are classified on the analogy of the hydrogen, namely according to the principal quantum number n, a sum of the orbital angular momentum ℓ and the spin angular momentum s, and its projection on a quantization axis m, Almost every issue in this thesis focuses on the ground state cases, that is, $n = 1$ and $\ell = 0$. In this condition, the Ps can be simply classified according to the total spin s as in Table. 2.1. Since the fermion systems with

Total Spin s	Projection m	State	C parity	Name
0	0	singlet	even	parapositronium (p-Ps)
1	0, ± 1	triplet	odd	orthopositronium (o-Ps)

Table 2.1: The classification of Ps according to their quantum numbers.

the orbital momentum, ℓ and spin angular momentum, s, have a parity of

$(-1)^{\ell+s}$ under a charge-conjugation transformation (C), the o-Ps and p-Ps have a odd and even C parities respectively. On the other hand, the system consisting of several photons have a C parity of $(-1)^n$, where n is a number of photons in the system. Due to the C-invariance of the electromagnetic interaction, the decay modes of the Ps are restricted as,

$$\text{o-Ps} \to n\gamma, \ \ n = 3, 5, 7, 9 \cdots$$
$$\text{p-Ps} \to n\gamma, \ \ n = 2, 4, 6, 8 \cdots$$

Because a single photon decay mode is prohibited by an energy momentum conservation, the lowest order decay channel of o-Ps is 3γ. As a number of photon corresponds to the number of electromagnetic vertex, the increase of decay photon contributes one power of α to the decay rate. In addition, the phase space of the final state is getting smaller as number of final state photon increases.

Five-photon decay branching ratio of o-Ps has been already calculated [8],

$$\begin{aligned} BR_{th}(\text{o-Ps} \to 5\gamma) &= \Gamma(\text{o-Ps} \to 5\gamma)/\Gamma(\text{o-Ps} \to \gamma\gamma\gamma) \\ &= 0.19(1)\,(\alpha/\pi)^2 \\ &\simeq 1.0 \times 10^{-6}. \end{aligned} \tag{2.1}$$

This theoretical expectation have been confirmed to be consistent with the measurement [9] within a experimental error,

$$BR_{ex}(\text{o-Ps} \to 5\gamma) \simeq 2.2^{+2.6}_{-1.8} \times 10^{-6}. \tag{2.2}$$

Thus we can simply neglect the influence of the 5γ decay contribution to the total width. This is also the case with p-Ps, where the 4γ contribution can be neglected. From the above reasons, o-Ps and p-Ps mostly decays into 3γ's and 2γ's respectively, and these relations suggest that the decay rate of p-Ps is approximately 10^3 times higher than the decay rate of o-Ps, and this facilitates the separation of the o-Ps events from that of the p-Ps.

2.2 Theoretical Description of o-Ps and p-Ps Decay Rate

Theoretical expression for o-Ps and p-Ps decay rate (or the reciprocal value of the lifetime), known at present, can be written in the form of perturbation,

$$\begin{aligned} \lambda_{\text{o-Ps}} &= \lambda_o^{(0)} \left[1 + A_o \left(\frac{\alpha}{\pi}\right) + B_o \left(\frac{\alpha}{\pi}\right)^2 \right. \\ &\left. + C_o\ \alpha^2 \ln\frac{1}{\alpha} + D_o\ \frac{\alpha^3}{\pi} \ln^2\frac{1}{\alpha} + E_o\ \frac{\alpha^3}{\pi} \ln\frac{1}{\alpha} + \cdots \right], \end{aligned} \tag{2.3}$$

$$\lambda_{\text{p-Ps}} = \lambda_p^{(0)} \left[1 + A_p \left(\frac{\alpha}{\pi}\right) + B_p \left(\frac{\alpha}{\pi}\right)^2 + C_p\, \alpha^2 \ln\frac{1}{\alpha} + D_p\, \frac{\alpha^3}{\pi} \ln^2\frac{1}{\alpha} + E_p\, \frac{\alpha^3}{\pi} \ln\frac{1}{\alpha} + \cdots \right], \quad (2.4)$$

where $\lambda_o^{(0)}$, $\lambda_p^{(0)}$ are the lowest order decay width of the o-Ps and p-Ps respectively. The higher order terms, whose coefficients are expressed as A, B, C, D, E, will be discussed in the following sections, and the ellipses denote unknown higher order terms which are neglected in this thesis.

2.2.1 The Lowest Order Decay Width

The lowest order calculations have been done for o-Ps firstly by Öre and Powell [10], and confirmed later by other authors [11, 12]. For p-Ps the plain calculation can be found in many primers, for instance in [13]. The lowest order decay width is given as,

$$\lambda_o^{(0)} = \frac{2(\pi^2-9)m_e\alpha^6}{9\pi} = 7.211\,17\ \mu s^{-1}\ (138.67\ ns) \quad (2.5)$$

$$\lambda_p^{(0)} = \frac{m_e\alpha^5}{2} = 8\,032.5\ \mu s^{-1}\ (124.49\ ps), \quad (2.6)$$

where m_e is the electron mass. The α^3 powers in each width are originated from a flux factor, which is a square of the wave function at the Ps origin in center of mass frame. The remaining α^3 contribution for the o-Ps (in case of p-Ps, α^2) is attributed to the number of decay photons in the Feynman diagram.

2.2.2 $O(\alpha)$ Correction

The $O(\alpha)$ corrections originate from the single photon exchange processes.

- The o-Ps case
  Many authors have evaluated the one-loop contributions to the decay width of o-Ps, and they seems to be in good agreement within the high accuracy. The most accurate result of $O(\alpha)$ corrections for o-Ps decay rate was obtained in [14] which evaluated them in an analytical form. The diagrams are shown in the Fig. 2.1(a)–(f), the obtained value is,

  $$A_o = -10.286\,606(10),$$

  which results in -2.389% large correction to $\lambda_o^{(0)}$. The calculations by some of the authors are summaries in the table 2.2.

year	A_o	Error	Reference
1977	-10.348	0.070	[15]
1983	-10.282	0.003	[16]
1992	-10.286 6	0.000 6	[17]
1996	-10.286 606	0.000 010	[14]

Table 2.2: The summary of $O(\alpha)$ correction

The evaluation of $O(\alpha)$ corrections on the energy spectrum of the emitted photon are carried out as well. This corrections are almost flat for the photon-energy, and the relative variation from the lowest order spectrum does not exceed 0.3% around 511 keV as shown in Fig. 2.2. Therefore the uncertainty of the energy spectrum due to the $O(\alpha)$ correction is expected to be small.

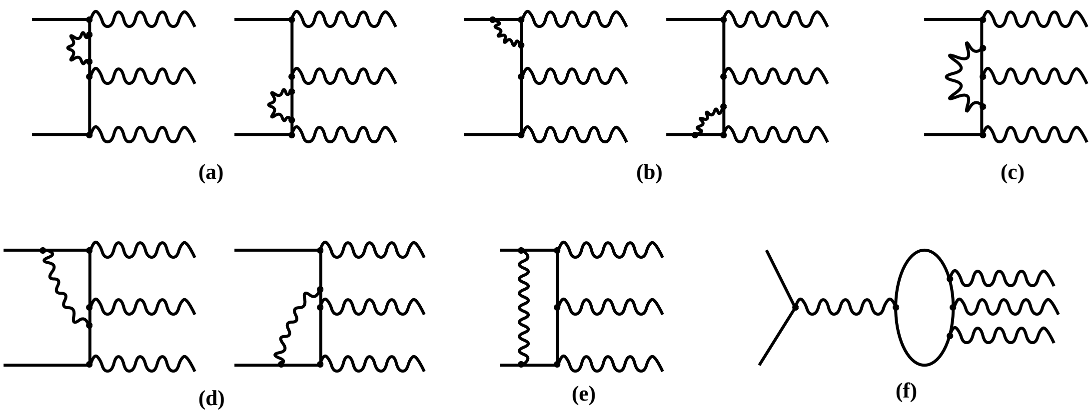

Figure 2.1: Graphs contributing to the o-Ps decay amplitudes through order-α. Each figure represents (a) self-energy, (b) outer-vertex, (c) inner-vertex, (d) double-vertex, (e) ladder, and (f) annihilation contributions.

- The p-Ps case

  For p-Ps, the value of $O(\alpha)$ correction term was calculated analytically in [18], the obtained value is,

$$A_p = -\left(5 - \frac{\pi^2}{4}\right).$$

This correction effects the decay width by -0.59% relative to the lowest order decay rate, $\lambda_p^{(0)}$.

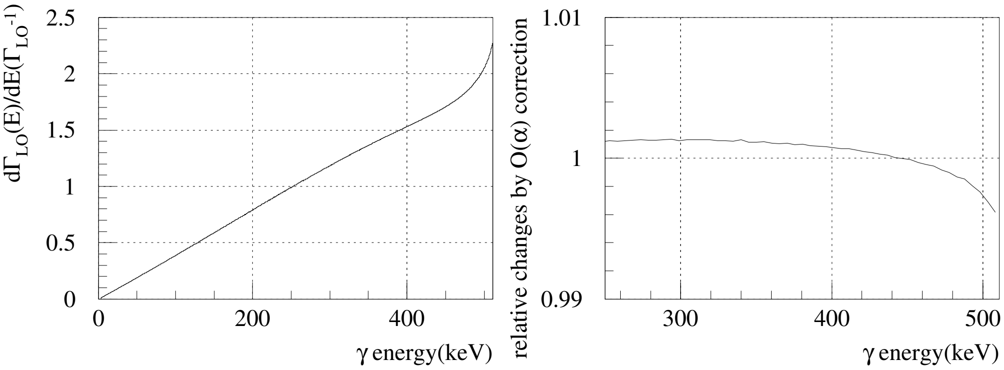

Figure 2.2: (a) The lowest order energy spectrum of a 3γ decay. (b) The relative change of the energy spectrum by the $O(\alpha)$ correction.

2.2.3 $\alpha^2 \ln(\alpha^{-1})$, $\alpha^3 \ln^2(\alpha^{-1})$, $\alpha^3 \ln(\alpha^{-1})$ Contributions

The logarithmic corrections can be considered as the relativistic effects in the wave function of positronium. It diverges at small distances logarithmically and is cut off at $\sim m_e$ where the annihilation occurs.

The logarithmic two-loop corrections, and the leading logarithmic corrections at three-loop are already obtained by analytical evaluation in some articles. As the size of $\ln(\alpha^{-1})$ is actually about 5, the $O(\alpha^2 \ln(\alpha^{-1}))$ correction is as important as the $O(\alpha^2)$ corrections. The already known coefficients are summarized in table 2.3

	Coefficient	correction to $\Gamma^{(0)}$	reference
for o-Ps			
C_o	$-1/3$	$-87\ ppm$	[19, 20, 21]
D_o	$-3/2$	$-4.5\ ppm$	[22, 23]
E_o	$+5.517$	$+3.4\ ppm$	[24, 25]
for p-Ps			
C_p	$+2$	$+522\ ppm$	[20]
D_p	$-3/2$	$-4.5\ ppm$	[23]
E_p	-7.919	$-4.8\ ppm$	[24, 25]

Table 2.3: The summary of the logarithmic contribution

2.2.4 $O(\alpha^2)$ Correction

The calculation of the $O(\alpha^2)$ correction to the decay rate of Ps is very complicated if the traditional bound-state methods is employed within the context of quantum field theory such as *Bethe-Salpeter analysis*. This is because each term in a traditional expansion has contribution from both nonrelativistic and relativistic momenta. To overcome these inconsistencies, a new and simpler procedure has been developed for the bound state calculations; then it can be applied to the calculations of coefficients B_o and B_p. This analysis is based on a rigorous nonrelativistic reformation of QED called *Nonrelativistic Quantum Electrodynamics* (NRQED).

In this framework of the effective field theory, the $O(\alpha^2)$ correction terms can be separated into nonrelativistic (soft) parts and relativistic (hard) parts.

The soft contributions come from the typical momenta region of the QED bound state systems which is order of $k \sim m\alpha$ where m is the reduced mass of Ps, and thus they are sensitive to the details of the bound state dynamics. In the theory, infinite number of nonrenormalizable interactions are suppressed by a factor of $1/\Lambda$ where Λ is an appropriate cutoff scale; in this case it is natural to take the cutoff scale as being the reduced mass of the system. On the other hand, the hard contributions arise as the relativistic momenta $k \sim m$ which can be treated with the traditional way.

- The o-Ps case
  A complete calculation of B_o had not been performed until quite recently. Only some partial results on the non-logarithmic $O(\alpha^2)$ corrections had been carried out [26, 27, 28].

  Recent theoretical efforts have focused on a more complete evaluation of this corrections, with the result $B_o = 44.52(26)$ [4]; this contributes to the lowest calculation by 240.3(1.4) *ppm*. Note that the light-by-light scattering diagrams have been omitted in this calculations, nevertheless they are considered to affect the calculation highly unlikely.

- The p-Ps case
  A complete calculation of B_p has been reported recently in [3], which was followed by the detailed description by the same authors [29], where the non-logarithmic part of the correction was found to be small as,

  $$B_p = 1.75(30). \qquad (2.7)$$

  This small correction has a 9.5(1.6)-*ppm* contribution to the lowest order calculation, and as will be mentioned later, a comparison with the most recent experimental result [2] gives a excellent agreement.

2.2.5 Another Correction

There are some other types of corrections being proposed for the o-Ps decay rate, which do not belong to any terms in Eq. (2.3).

- The biding effects [30, 31] — This effect is introduced to consider the non-perturbative nature corrections, while maintaining the analyticity and gauge invariance of the procedure. The calculation is introduced from the fact that the electrons in the intermediate stage are always in their off mass-shell; the mass M of the bound state and the mass m of the constituent electrons are different. Then the electron propagator in $e^+e^- \to 3\gamma$ decay amplitude is corrected by this gap. As a consequence, p-Ps and o-Ps decay rates receive the corrections of $O(\alpha^4)$ and $O(\alpha^2)$, respectively. While the correction for p-Ps is negligibly small for the present experimental precision, the biding energy correction for o-Ps affects by a non-negligible size, $-5\pi^2/4 \approx 12.34$ [31].
  This leads to a reduction of the decay rate by 67 *ppm*.

2.2.6 Summary of the QED Prediction

As already mentioned, the calculation of p-Ps decay rate which has been recently obtained [3, 29] up to a non-logarithmic $O(\alpha^2)$ correction, gives a excellent agreement with the precision measurement [2]. The theoretical prediction is,

$$\lambda_{\mathrm{p-Ps}}^{theory} = 7\,989.50(2)\ \mu s^{-1} \tag{2.8}$$

whereas the measured value is,

$$\lambda_{\mathrm{p-Ps}}^{exp} = 7\,990.0 \pm 1.7\ \mu s^{-1}. \tag{2.9}$$

Thus so far there is a consensus among the theorists that a new approach referred to as NRQED makes a great success as far as the p-Ps is concerned.

On the contrary, the decay rate of o-Ps is not verified by the experiments more than a $O(\alpha)$ level; verification of this level has been done by the latest measurements by the Tokyo group with about 400-*ppm* precision measurement [7], nevertheless no measurement has been done to test the $O(\alpha^2)$ level corrections hitherto.

Table 2.4 shows the summary of the calculation of o-Ps decay rate reviewed in the previous sections. Except for the last line of the table, that is the non-logarithmic $O(\alpha^2)$ term, the calculations are confirmed by several authors, indicating a reliance of the results. Since the value B_o has just been obtained by the recent work, it should need to be verified by the other calculations. Thus it would be premature to be convinced of the result now. In addition, there exists another effects which do not belong to the perturbative form, which could affect the decay rate by -67-*ppm* size.

terms	correction (ppm)	decay rate (μs^{-1})	lifetime (ns)
tree level	0.0	7.211 169	138.6738
$A_o\ (\frac{\alpha}{\pi})$	-23893.9	7.038 866	142.0683
$C_o\ \alpha^2 \ln(1/\alpha)$	-87.3	7.038 236	142.0811
$D_o\ (\alpha^3/\pi) \ln^2(1/\alpha)$	-4.5	7.038 204	142.0817
$E_o\ (\alpha^3/\pi) \ln(1/\alpha)$	+3.4	7.038 228	142.0812
$B_o\ (\frac{\alpha}{\pi})^2$	240.2	7.039 960	142.0463

Table 2.4: Summary of QED calculation for o-Ps decay rate

To summarize, it must be admitted that estimation of higher order terms are yet very vague and the calculation still possesses $50 - 100$ *ppm* uncertainty. In this thesis the following value is referred to as the $O(\alpha^2)$ corrected QED prediction.

$$\Gamma_{o-Ps} = 7.039\,960\ \mu s^{-1}. \tag{2.10}$$

Comparison between the theory and the experiments will be performed with this decay rate as a reference value.

2.3 Experimental Overview of the o-Ps Decay Rate

As mentioned in Sec. 1, the significant discrepancy between the theory and the measurement had existed obviously since later half of 1970's. The techniques employed and the obtained result are briefly reviewed in this section. The differences between the methods, accompanying problems will be discussed as well.

2.3.1 Chronology of the Measurement

Before starting we must decide how to describe the decay rate of o-Ps. In this thesis, it is expressed as the decay rate per a micro second, i.e. λ_o (μsec^{-1}) in conformity with the many articles.

The history of the o-Ps decay rate measurements are summarized in Table 2.5 with the corresponding lifetimes. As can be seen in the columns, the employed methods were classified into three types, the Cavity experiments, the Gas experiments, and the Powder experiments. In all the experiments, a positron was injected into a target material in order to form o-Ps, the time interval between the positron injection and the detection of γ-rays emitted from o-Ps decay were measured. This basic idea were common to all the measurements.

The Gas experiments are the most popular and the earliest techniques, which were performed by using positron sources to form Ps in gases at various pressures, and the decay rate of the vacuum was estimated by extrapolation to zero density of the gas.

In the Cavity experiments, Ps was formed in the vacuum container by allowing the slow positron beam to hit the surface of the MgO-lined cavity. The intrinsic decay rate in the vacuum was estimated by extrapolation to infinite cavity size. The extrapolated values, in this case, are the surface area of the cavity container divided by volume, (S/V), or the effective beam aperture size divided by volume, (A'/V), or both of them.

In the Powder experiments, Ps was formed in SiO_2 powders using positron sources as in the gas experiments. Ordinary powder experiments are performed at various powder density, and the extrapolation to zero density yields the o-Ps decay rate which is similar to the way that the gas experiments use.

Another type of powder experiment, appeared in 1995 [7, 32], was quite different from all the previous experiments, because it no longer used extrapolation. In that powder experiment, the measurements were performed incorporating the thermalization process of o-Ps, which will be discussed at later section.

In Fig. 2.3, these values are plotted in chronological order to see easily the historical change of the measured value and its precision.

The historical relation between the theoretical value and the precision measurements in the early years are well summarized in reference [33], which we will follow in a brief review.

index	Year	Decay rate (μs^{-1})	Total error (μs^{-1})	(ppm)	Method	Lifetime (nsec)	Reference
1	1968	7.275	0.015	2062	gas(Freon)	137.70	[34]
2	1976	7.104	0.006	844	SiO_2 powder	140.77	[35]
3	1976	7.09	0.02	2821	cavity	141.04	[36]
4	1978	7.056	0.007	992	gas(Freon, isobutane)	141.72	[37]
5	1978	7.067	0.021	2972	SiO_2 powder	141.50	[37]
6	1978	7.050	0.013	1844	cavity	141.84	[38]
7	1978	7.121	0.012	1685	cavity	140.41	[39]
8	1978	7.045	0.006	852	gas	141.94	[40]
9	1982	7.051	0.005	709	gas(isobutane)	141.84	[41]
10	1987	7.031	0.007	996	cavity	141.22	[42]
11	1987	7.0516	0.0013	184	gas(isobutane, N_2,etc.)	141.81	[43, 33]
12	1989	7.0514	0.0014	199	gas(N_2, Ne)	141.82	[5]
13	1990	7.0482	0.0016	227	cavity	141.88	[6, 44]
14	1995	7.0398	0.0029	412	SiO_2 powder	142.05	[7, 32]

Table 2.5: The history of the o-Ps decay rate measurements

- *The first stage*

  The first measurement of o-Ps was performed in 1968 [34]. In those days theory and experiment agreed at 0.2% level of accuracy. In 1976 two experiments are performed, which resulted in the large discrepancy between the theory and experiments. This caused the reevaluation of both the theory and old experiments.

- *The second stage*

  After the new calculation in 1977 [15], the new precision experiments also drastically improve the measurement. In the group of Michigan(which is sometimes referred to as 'Ann Arbor'), the cavity and the gas experiments represented a remarkable progress, especially the gas experiments are carried out for a various gases to check the gas independency. Here again, the discrepancy with the theory motivated a further investigation on both the theory and experiments.

- *The third stage*

  In order to clarify the discrepancy, the reduction of the experimental error to the 200-*ppm* level was aimed at, which was achieved by the two types of measurements, the Cavity [6] and the Gas [43, 5] experiments around the beginning of 1990's. The obtained results from these measurements were found to be consistently shorter than the theoretical prediction by a 1000-*ppm* level. This discrepancies had been called *orthopositronium lifetime puzzle*, and aroused various discussions for the physical interpretations.

  Since most measurements resulted in the higher decay rates (shorter lifetimes) than the theoretical prediction, it was respected that there might be some unknown rare decay channels for the o-Ps to compensate the discrepancy. The exotic decay modes had been searched for in that period, which will be reviewed in the next section.

- *The fourth stage*

  In 1995, a new measurement was performed in our laboratory (Tokyo group) using SiO_2 powder for the o-Ps formation [7]. The method employed there was essentially different from the previous measurements, because the new technique involve the 'thermalization process' of o-Ps into the measurement for the first time. The thermalization of o-Ps is considered as the main source of systematic error for all the other previous measurements.

  As can be seen from Fig. 2.3, the new method yielded a result being consistent with the QED prediction, although the error of the measurement was somewhat large (410 *ppm*). It excluded the other previous measurements [43, 5, 6] by 2.9–4.1 experimental standard deviations.

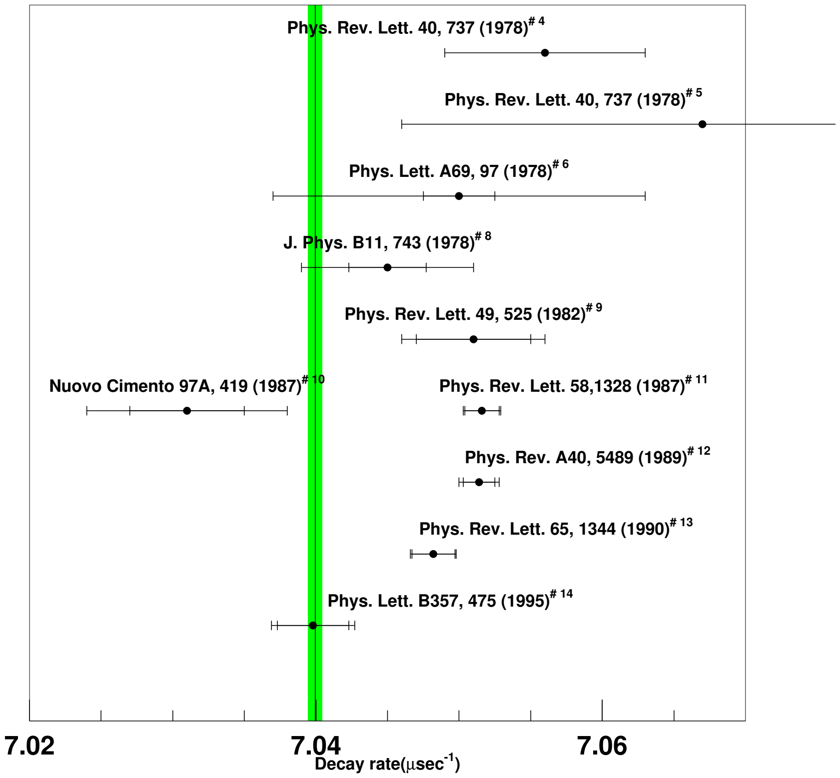

Figure 2.3: The chronology of the o-Ps decay rate measurement. The number on the right shoulder of each item indicates a corresponding index number in Table 2.5. Vertical band represents the $O(\alpha^2)$-corrected NRQED prediction of 7.039 960 μs^{-1} with its uncertainty of ± 70 ppm. Note that the theoretical value obtained in 2000 gives a great agreement with the experimental value in 1995. The inside small line on each error bar represents a error solely due to statistics.

2.3.2 Review of the Exotic Decay Modes

As is evident from Fig. 2.3, before 1995 the measured decay rate with less than 230 ppm errors were consistently larger than the theoretical prediction. This tendency was considered as the possible indication for a presence of the new decay channels. In this respect, the slow decay rate of o-Ps (a factor of 1100 slower than parapositronium) makes the o-Ps an attractive and promising hunting field in searching for exotic processes beyond the standard model. Various exotic decay modes were explored by several groups, resulted in no evidence so far for a any new candidate. A good review of these exotic modes is found in [32]. In this thesis only the brief summary is re-arranged.

- o-Ps$\rightarrow \gamma\ X^0$
  The o-Ps decays into a single photon and a long-lived weakly interacting particle X^0. The observation is carried out in the manner that o-Ps is decaying into a single photon with a well defined energy with an anti-coincidence that another photon is not detected. The contribution from this decay mode had been confirmed to be below 1 *ppm* (90% C. L.) [45, 46].

- o-Ps$\rightarrow \gamma\ \Phi^0$
  The o-Ps decays into a single photon and a short-lived neutral spin-0 boson, Φ^0, which decays into two photon immediately. If the mass of Φ^0 boson is under 1000 keV/c^2, the energy of the first emitted photon is so defined that it allows us to search a peak within an inclusive 3γ energy spectrum. This mode was excluded with 400 *ppm* (90% C. L.) [47, 48], under 900 keV/c^2 m_{Φ^0} region, and excluded by 200 *ppm* (90% C. L.) [49] in the mass range from 847 to 1013 keV/c^2.

- o-Ps$\rightarrow \gamma\gamma\ \gamma^\dagger$
  The o-Ps decays into two photons and a weakly interesting neutral vector boson, $\gamma^\dagger$. In this case, it is difficult to search experimentally, since the γ-rays from this three-body decay would not show any peak. Instead the p-Ps dacaying into $\gamma\ \gamma^\dagger$ (in this case two-body nature enables the peak hunting method) was searched for. Then its upper limits is converted to the hypothesized o-Ps decay. The exotic three body decay of o-Ps is limited under 6.2 *ppm* ($m_{\gamma^\dagger} < 200$ keV/c^2, 90% C. L.) and 17 *ppm* ($m_{\gamma^\dagger} < 1022$ keV/c^2, 90% C. L.) [50].

- o-Ps$\rightarrow$ invisible
  The o-Ps decays into exotic weakly interacting particles. The search was performed by measuring the energy deposited in a hermetic photon detector for each positron from ^{22}Na stopping in an aerogel target. The upper limit of 2.8 *ppm* (90% C. L.) is obtained [51].

- o-Ps$\rightarrow 2\gamma$
  The o-Ps decays into 2γ mode forbidden by space-rotational and by charge-conjugation invariance. Measurement was performed using a high energy-resolution detector i.e. germanium detector, in order to discriminate the expected sharp peak of the two photon decay from the broader peak of the pick-off annihilations. The decay was limited by a 230 *ppm* level (90% C. L.) [52, 53].

- o-Ps$\rightarrow 4\gamma$
  The o-Ps decays into 4γ mode. This mode is also forbidden by charge-conjugation in QED. An upper bound on the branching ratio of 8 *ppm* (68% C. L.) was obtained [54].

Above modes are all restricted to a low level.

These facts also support the conclusion of the measurement in 1995 [7] that it is more likely the discrepancy was due to the thermalization effect of o-Ps, rather than attributing them to the exotic decay modes of o-Ps, or other unknown effects.

Chapter 3

Experiment

Measuring the intrinsic decay rate of o-Ps in vacuum would be quite easy if it were not for annihilation effect between the positron constituting the o-Ps and the electron of the target materials. This phenomenon called as the pick-off annihilation is the dominant background in all the o-Ps decay rate measurements regardless of their method. Therefore how to deal with this background events determines the accuracy of the experimental value.

Firstly this chapter describes the method which is adopted in this measurement. The method called as the direct 2γ correction methodinvolves all the information from the thermalization of o-Ps. Then the detailed descriptions on the experimental apparatus will follow.

3.1 Theory of the Experiment

3.1.1 Pick-off Rate

In all the o-Ps decay rate measurements, positrons from the β^+ source are injected into the target materials to form Ps. These materials such as gases, oxide powders (e.g. SiO_2) or cavities whose inside walls are coated by oxide materials (MgO or Al_2O_3), serve as the source of electrons constituting the o-Ps. The o-Ps continues to collide with the surrounding target materials, and inevitably cause the pick-off annihilation with the atomic electrons inside the target materials, and this can be observed as a two-photon decay. It also occurres that the electron of the o-Ps exchange itself with the opposite spin electrons of the target materials, and this conversion from o-Ps to p-Ps resulting to the rapid annihilation into two photons, which is referred to as *spin-flip*. In this measurement this spin-flip events are also regarded as the pick-off annihilation.

If no pick-off annihilation exists, the measured time-spectrum which is defined as the distribution of time intervals between the positron injection and the detection of γ rays emitted from o-Ps decay, simply obeys the exponential law, that is, the decay probability at the time t, $dN(t)/dt$, is expressed as

$$\frac{d}{dt}N(t) = N_0 \exp(-\lambda_{3\gamma}t) + C, \tag{3.1}$$

where $\lambda_{3\gamma}$ is the intrinsic decay rate of o-Ps and C represents the flat spectrum of accidental events.

Taking account of the pick-off effect, the observed o-Ps decay rate in media, λ_{obs} will be the sum of the intrinsic decay rate of o-Ps into 3γ's, $\lambda_{3\gamma}$, and the pick-off annihilation rate into 2γ's, λ_{pick},

$$\lambda_{obs}(t) = \lambda_{3\gamma} + \lambda_{pick}(t). \tag{3.2}$$

Since the o-Ps energy varies with time, the pick-off rate is described as a function of time. This time dependence of λ_{obs} can be depicted with the thermalization of o-Ps which will be discussed in Sec. 3.1.3.

3.1.2 Systematic Problem with the Extrapolation

Phenomenologically, the pick-off rate can be expressed as,

$$\lambda_{pick}(t) = n\sigma_a v(t), \tag{3.3}$$

where n is the density of the target materials, σ_a is the annihilation cross section, and v is the velocity of the o-Ps. In the previous experiments using extrapolation methods, the pick-off rate was assumed to be proportional to only the density of the materials. Therefore the observed decay rate, λ_{obs} was measured at some points varying the density of the target materials, and then extrapolation to zero density asuumed to yield the intrinsic decay rate of o-Ps in vacuum. In this extrapolation process, there might be a large uncertainty due to the assumption that λ_{pick} depend linearly on the density of target materials, or to the inverse of the cavity's size in case of the cavity experiment. Some refutations against this assumptions can be found,

- This assumption is valid as far as the collisions between the o-Ps and the molecules of the target materials are simply elastic. This is an ideal case. But in practice, the energy loss mechanism fractionally obeys to the inelastic law, and the multiple scattering at the surface of materials also disturbs the linear dependence assumption.

- As can be seen in Eq. (3.3), λ_{pick} also depends on the velocity of the o-Ps and on the kinetic energy of the o-Ps. In extrapolation method, time dependence of the o-Ps energy had been ignored to be small enough on the assumption that *the thermalization process of o-Ps* at energies below 1 eV to the ultimate room temperatures of 0.03 eV, takes no more than one hundred *nsec*. Thus the pick-off rate is assumed to be converged to a constant value after one hundred *nsec* of the o-Ps formation.

This assumption is based on the fact that the collision cross-sections between the o-Ps and the target materials are large enough, and the thermalization of o-Ps proceeds quickly within a hundred *nsec*. Recent measurements [55, 56] clearly showed the collision cross-sections are significantly smaller than previously considered.

The time-spectrum fitting is carried out with the simple exponential function Eq. (3.1) for the extrapolation method. Start time, t_{start}, of the fit region is stepped out successively in order to determine the observed decay rate at certain target condition. In recent measurements, fast t_{start} values are used; the Cavity experiment [6], typically adopted $t_{start} = 170\ ns$ for all runs, and in the Gas experiment [5], they used $t_{start} = 180\ ns$ for all gases except the lowest pressure Ne and neopentane runs. These fast t_{start} values must have resulted in the larger decay rates especially in the lower density limit, because the decay rate would not have converged to an asymptotic value in such a fast time.

Therefore it is proved that the assumptions are no longer valid and the thermalization process must be taken into accout.

3.1.3 Thermalization Process in SiO_2 Powder

Since the fractional energy loss of o-Ps per collision with SiO_2 powder and the collision rate are dependent on its energy, time dependence of the average kinetic energy of o-Ps at time t, $\overline{E(t)}$, is derived from the Boltzmann equation, and expressed as in [57, 58],

$$\frac{d}{dt}\overline{E(t)} = -\sqrt{2m_{Ps}\overline{E(t)}}\left(\overline{E(t)} - 3k_BT\right)\sum_{j=0}^{\infty} a_j \left(\frac{\overline{E(t)}}{k_BT}\right)^{j/2}, \qquad (3.4)$$

where m_{Ps} is the mass of o-Ps, T is the room temperature, and the k_B is the Boltzmann constant. In the equation, the asymptotic value of $\overline{E(t)}$ is replaced with $3k_BT$, instead of $\frac{3}{2}k_BT$ for the ideal gas. In the last term, the momentum transfer cross section of the SiO_2 is expanded in terms of $\overline{E(t)}$, and expressed as the coefficients a_j which stands for the effect from the effective mass at the surface of the SiO_2 grains, $\overline{M}$, and the mean distance between the grains, $\overline{L}$. As a consequence of this thermalization of o-Ps, the pick-off annihilation rate changes in accordance with $\overline{E(t)}$ in Eq. (3.4). Since the pick-off rate is proportional to the average velocity of the o-Ps as can be seen in Eq. (3.3), the ratio of the pick-off rate to the intrinsic o-Ps decay rate, i.e. $\theta(t) \equiv \lambda_{pick}(t)/\lambda_{3\gamma}$ is deduced to obey the following differential equation,

$$\frac{d}{dt}\theta(t) = -C\left(\theta(t)^2 - \theta_\infty^2\right)\sum_{j=0}^{\infty} a_j\theta(t)^j, \qquad (3.5)$$

where $\theta_\infty \equiv \theta\ (t \to \infty)$, $a_j\ (j = 0, 1, 2, \cdots)$, and C are constant values.

It is well known from the measurement in 1995 [7] that it takes about 600 ns for o-Ps to be well thermalized in low-density SiO_2 powders; this powder is the same type as used in the present measurement (named Powder I in Sec. 3.2.2). Therefore it is strongly required that the pick-off rate λ_{pick} is measured directly as a function of time, so that one can obtain the intrinsic decay rate of o-Ps without any ambiguity due to the thermalization.

Once obtained the precise thermalization function, the pick-off rate $\lambda_{pick}(t)$ contains all the information about the thermalization process. Then the population of o-Ps at time t, $N(t)$, is expected to obey the following differential equation,

$$\frac{d}{dt}N(t) = -(\lambda_{3\gamma} + \lambda_{pick}(t))\ N(t), \tag{3.6}$$

the solution of this equation is,

$$N(t) = N_0\ \exp\left(-\int_0^t\ (\lambda_{3\gamma} + \lambda_{pick}(t'))\ dt'\right). \tag{3.7}$$

The measured time spectrum, $N_{obs}(t)$ is expected to be,

$$\begin{aligned}
N_{obs}(t) &= \varepsilon\lambda_{obs}(t)N(t) \\
&= (\varepsilon_{3\gamma}\lambda_{3\gamma} + \varepsilon_{pick}\lambda_{pick}(t))\ N(t) \\
&= \epsilon_{3\gamma}\lambda_{3\gamma}\left(1 + \frac{\epsilon_{pick}}{\epsilon_{3\gamma}}\frac{\lambda_{pick}(t)}{\lambda_{3\gamma}}\right) \\
&\qquad \times N_0 \exp\left(-\lambda_{3\gamma}\int_0^t\left(1 + \frac{\lambda_{pick}(t')}{\lambda_{3\gamma}}\right)dt'\right),
\end{aligned} \tag{3.8}$$

where ε_{pick} and $\varepsilon_{3\gamma}$ are the detection efficiencies for the pick-off annihilations and 3γ decays respectively.

In practice, as the time spectrum is obtained with the time-to-digital converter (TDC) as a time interval between the start pulse (β^+ injection) and the stop pulse (γ detect), other complications arise from the detectors and electronics.

Finally we obtain the following form,

$$N_{obs}(t) = e^{-R_{stop}t}\left[\left(1 + \frac{\varepsilon_{pick}}{\varepsilon_{3\gamma}}\frac{\lambda_{pick}(t)}{\lambda_{3\gamma}}\right)N_0 \exp\left(-\lambda_{3\gamma}\int_0^t\left(1 + \frac{\lambda_{pick}(t')}{\lambda_{3\gamma}}\right)dt'\right) + C\right]. \tag{3.9}$$

The constant term C arises from an accidental hit whose β-start does not correspond to the γ-stop (o-Ps) event.

Another factor $\exp(-R_{stop}t)$ in Eq. (3.9) comes from the fact that the TDC always accept the first γ hit as a stop signal. The size of the term is determined by the random counting rate R_{stop}, which is proportional to a strength of the positron source.

The detail description of the expected time spectrum is described in the appendix A of reference [32].

Note that the energy distribution of photons from the 3-body γ-decay is continuous below the steep edge at 511 keV as shown in Fig. 2.2 (a), whereas the final state of the pick-off annihilation is 2-body; a behavior producing the 511-keV monochromatic peak.

If the energy and timing information are simultaneously measured with a high energy resolution γ-ray detector, such as germanium detector, $\lambda_{pick}(t)/\lambda_{3\gamma}$ can be determined from the energy spectrum of the emitted photon.

Providing the ratio is determined as a function of time, it includes all the information about the o-Ps thermalization. Then the intrinsic decay rate of o-Ps, $\lambda_{3\gamma}$, can be directly obtained by fitting the observed time spectrum with Eq. (3.9); an approach which precludes any ambiguity due to the thermalization process.

This technique called *the direct 2γ correction method* involves the thermalization function $\lambda_{pick}(t)/\lambda_{3\gamma}$ into the fitting procedure as described above. Since the practical size of the pick-off ratio is around 1% for the low-density SiO_2 powder, the error propagated from $\lambda_{pick}(t)$ to the final result, $\lambda_{3\gamma}$ is well suppressed by a factor of about 100.

Furthermore this method gets rid of the any extrapolation procedure. Thus there is no need to assume the linear dependence nor the o-Ps behavior at the surface of material.

3.1.4 Measurement in 1995

In 1995, the direct 2γ correction methodwas used for the first time. They carried out two independent measurements with two different types of SiO_2 powder as a target material, and obtained the consistent result from two runs. The measurement directly took into account the thermalization process and the obtained value is consistent with the $O(\alpha^2)$ QED prediction as in Sec. 2.3.1.

However there were several remaining problems,

- The larger experimental error (410 *ppm*) compared with the other previous measurements (180-230 *ppm*).

- The measured functions, $\lambda_{pick}(t)/\lambda_{3\gamma}$, for two runs (different types of powder) were similar and consistent within a statistical error as in Fig. 3.1. In order to clarify the powder independence of the method, the systematic test should have been performed, that is, the powders with entirely different thermalization characters should have been used.

- The decay rates at 220 *ns* fitting start time were adopted as a resultant value for both runs. Because the decay rates were sytematically

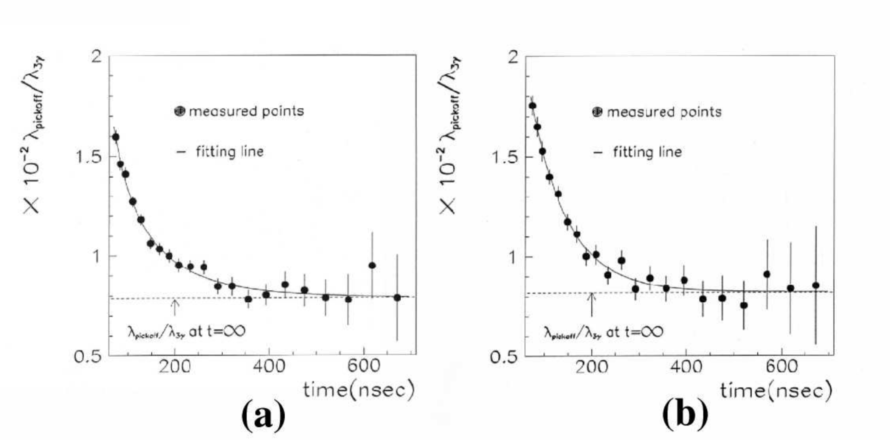

Figure 3.1: The $\lambda_{pick}(t)/\lambda_{3\gamma}$'s are plotted as a function of time (from the measurement in 1995 [32]). Two figures represent the two different powders, (a) powder 1 and (b) powder 2.

increasing before 200 ns as in Fig. 3.2 (in the figure, the decay rates are expressed in the lifetime form, thus they decreased instead.). The origin of these phenomena were not understood at that time, and clear explanation was needed to prove the validity of the direct 2γ correction method.

In order to clear up above problems, the following trials are performed in the present measurement.

- Two types of SiO_2 powders with quite different o-Ps thermalization features are prepared; this will be the systematic test for the direct 2γ correction method.

- In order to investigate the origin of the systematic increasing of the decay rate before fitting start time of 200 ns, the timing system of the entire setup is thoroughly improved. If the decay rates are obtained without dependence on the fitting start time before 200 ns, the statistical accuracy will be considerably improved.

3.2 Description of Apparatus

In this experiment, two longtime measurements are performed. These runs, referred to as 'RUN I' and 'RUN II', have collect the date for about six month each. Some property of experimental setup, e.g. the type of powder, the number of detectors, e.t.c., has been changed between the RUN's. Following sections will describe the experimental setups, concerning these differences.

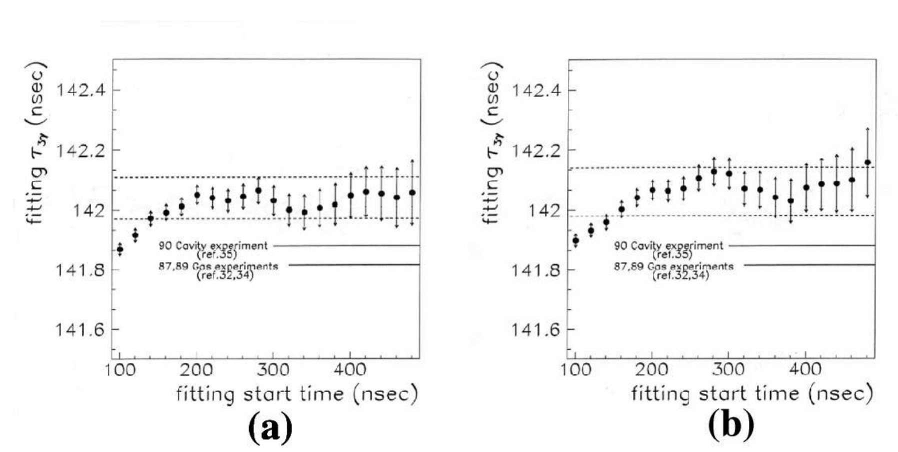

Figure 3.2: The fitted lifetimes (decay rate^{-1}) of o-Ps are plotted as a function of fitting start time (from the measurement in 1995 [32]).

3.2.1 Radioactive Source and Positronium Formation assembly

The ^{22}Na positron source (545 keV Max) is placed at the center of the setup which can be seen in Fig. 3.3. The diameter of the source is 2 mm and sandwiched between two sheets of plastic scintillators (NE104). The source is held by a cone made of aluminized mylar. The scintillators are 100 μm thick for each, and mylar is 25 μm thick corresponding to a area density of about 17 mg/cm^2 in total. The mass attenuation coefficient for the ^{22}Na spectrum is 22 mg/cm^2, thus about the half of the positrons can path through the scintillators and the aluminized mylar without being absorbed. The strength of the source is approximately $0.033 - 0.029\ \mu C_i$ ($0.027 - 0.024\ \mu C_i$) for RUN I (RUN II); Owing to a comparatively long radioactive half-life of ^{22}Na, stable strength of the source is available during two runs. Due to this faint strength of source, we can well suppress the accidental background contributions during the measurements.

The cone is placed at the center of a cylindrical vacuum container of diameter 50 mm made of 1 mm thick glass. This container is filled with silica powder (SiO_2 whose character will be discussed in Sec. 3.2.2), and is evacuated to 5×10^{-2} (6×10^{-2}) Torr for RUN I (RUN II).

The positrons emitted from the source deposit energy of 50-100 keV on the scintillators while passing. After passing through the cone, the positron slows down by colliding iteratively with electrons of the SiO_2 powder, from an energy scale of a few hundreds keV to an atomic energy scale of about 10 eV. The time needed for this process is estimated to be a sub-$nsec$, as the range of positron is known to be about 1 cm.

The scintillation γ's emitted from the plastic scintillators are reflected

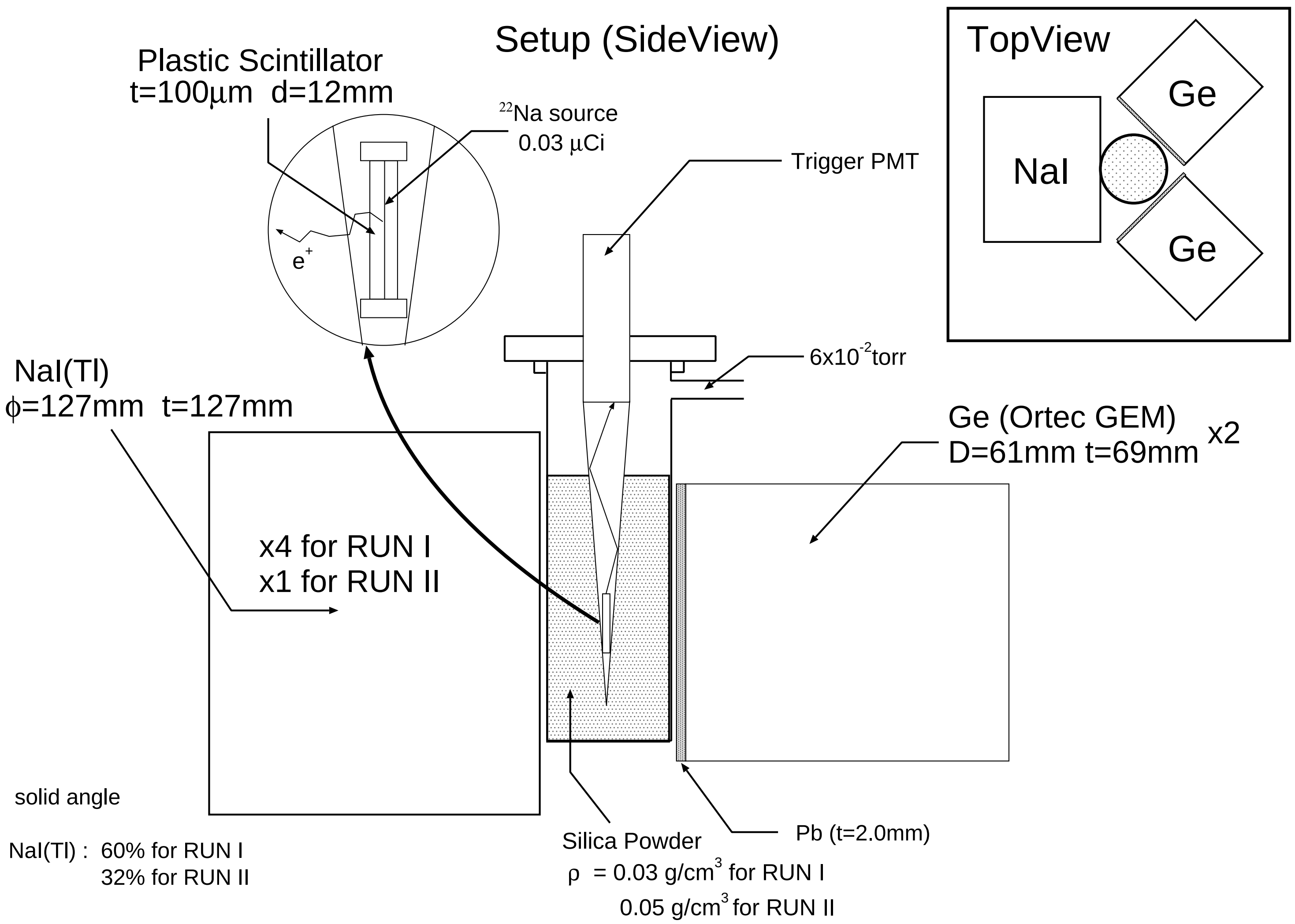

Figure 3.3: Schematic diagram of apparatus.

iteratively on the inside surface of the aluminized mylar and collected by a 1/2-*inch* photomultiplier (Hamamatsu H-3165-04). The pulse from the photo-tube makes the trigger signal to a whole data acquisition system, and from now on the photo-tube will be referred to as trigger PMT.

3.2.2 Characteristics of SiO_2 powders

In this thesis, two types of SiO_2 powders are used as a target materials; the place where the o-Ps can be formed efficiently. To be exact, these powders are amorphous silicon dioxides provided by Nippon Aerosil Ltd., and commonly have following characteristics.

- A chain-like agglomeration of primary grains makes 3-dimensional network structures. These structures makes higher class of group whose size is about several μm, referred to as the aggregate or agglomerate.
- It is reported that an in-uniformity in density of the powder is not observed within an error of a few % level. Thus one can expect the uniformity of the powder inside the container is good enough.
- Roughly speaking there are two types of SiO_2 powders available that users can choose in accordance with their purpose of usage, the hydrophile and the hydrophobe. In this measurement, the hydrophile is used for RUN I and the hydrophobe is used for RUN II. Since water content of the powder surely increase the pick-off annihilation probability at surface of the grains, it is better to use the hydrophobe rather than the hydrophile. Approximately 82 % of the hydroxyl groups ($-$OH); or referred here as $-Si(OH)_3$ instead, has been substituted with the tri-methyl-silyl groups ($-Si-(CH_3)_3$) in hydrophobic processing for Powder II. Furthermore, to remove a water absorbed at the surface of grains, the SiO_2 powder is heated for 4 hours long under the condition of the atmospheric pressure, in $130°C$, just before evacuation of the container.

The characteristics of two powders are summarized in table 3.1. The surface

	Powder I	Powder II
Grade (code name)	300CF	R812
primary grain size (nm)	7	7
surface area (m^2/g)	300 ± 30	260 ± 30
density (g/cm^3)	0.03	0.05
mean distance (nm)	340	200
process	hydrophile	hydrophobe

Table 3.1: Characteristics of two powders used in the measurement

area of the grain is estimated by the BET method which utilizing the physical adsorption of nitrogen gas on the surface of SiO_2 powders [59]. The mean distance between the grains $\overline{L}$ has been calculated with the assumption of uniform size and spacial distributions of the grains as,

$$\overline{L} = \frac{4}{3}\left(\frac{\rho_0}{\rho} - 1\right) R, \tag{3.10}$$

where ρ_0 is the bulk density of amorphous silica ($2.20\, g/cm^3$), ρ is the density of the powder, and R is the mean radius of the primary grains. Because the pick-off rate is proportional to the collisional frequency between the o-Ps and the grains, it strongly depends on this mean distance $\overline{L}$ (in this case, it doesn't depend only on the density of the powder, but also on the primary grain size.). Therefore two different powders each having their own mean grain distance, is expected to yield a difference in pick-off ratio, which can be clearly seen in the analysis section.

3.2.3 Environments

Evacuation

A evacuation of the SiO_2 container is performed through the two exhaust pipes sticking out of the side near the trigger PMT. one is connected to a rotary pump (EDWARDS E2M5) through a filter which is for a powder confinement, the other is connected to a Pirani gauge directly for a pressure measurement. The container is evacuated to $5(6) \times 10^{-2}$ mbar for RUN I (RUN II), in order to reduce the probability that the o-Ps collides with atmospheric molecules, especially O_2. Since O_2 has two unpaired electron spins, it can convert the o-Ps into the p-Ps via spin-exchange collisions [58] which has been already explained in Sec. 3.1.1 as a *spin-flip*. The pick-off decay rate of o-Ps in 1 atm of oxygen was observed to be about $35\,\mu s^{-1}$ [60], thus assuming a scalablity about the pressure dependence of pick-off rate, one can expect $35 \times 10^{-4} \mu s^{-1}$ increase of pick-off rate in the air pressure of 1.0×10^{-1} mbar. This corresponds to $\lambda_{pick}/\lambda_{3\gamma} = 0.05\%$ which is much smaller than 0.8% of powder pick-off ratio. Hence we can neglect the final systematic errors due to this evacuation.

Magnetic field

Due to the Zeeman effect, the mixing between the o-Ps ($m = 0$) and the p-Ps can occur in the presence of a magnetic field. This mixing easily disturb the decay rate measurement of o-Ps. The absolute strength of magnetic field around the positronium formation assembly is measured with 3-Axis Hall Teslameter [61] to be $|m| \simeq 0.5 \pm 0.1$ $Gauss$ which is almost consistent with the terrestrial magnetism of 0.3 $Gauss$. This feeble field hardly contributes to the mixing of the two states, and estimated to be 3×10^{-11} [62], which is extremely small and the observed o-Ps can be considered to be a pure o-Ps state.

3.2.4 Detectors

In this experiment, two types of γ-ray detectors are used for the detection of o-Ps decays. One type is the germanium semiconductor detector, and the other is the NaI(Tl) scintillator. These detectors are used for different purposes according to their features. Two germanium detectors are used throughout two long runs, while four (one) NaI(Tl) scintillators are used for RUN I (RUN II).

Germanium detectors

Two P-type high-purity coaxial germanium detectors (Ortec GEM 38195-P-plus series) are used in both RUN I and RUN II. Ge detectors are used to precisely determine the thermalization, i.e. $\lambda_{pick}(t)/\lambda_{3\gamma}$ as a function of time. The design of Ge detectors is shown in Fig. 3.4, where the size of

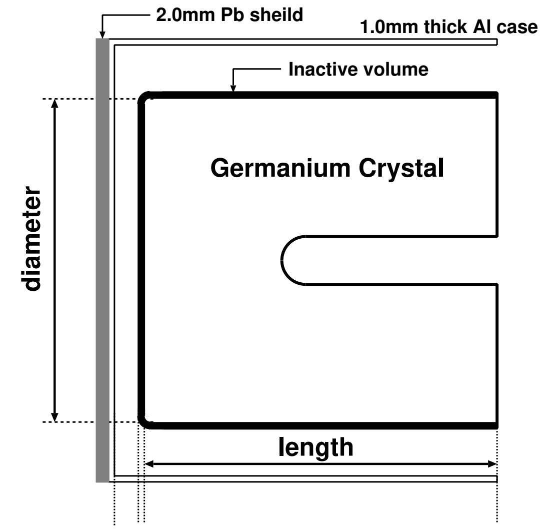

Figure 3.4: Schematic diagram of germanium detector.

crystals are bit different between them, and summarized in table 3.2. From now on, they are referred to as GE0 and GE1. As a P-type Ge detector, the lithium-diffused layer which is denoted as inactive volume in Fig. 3.4 has been formed over the outer surface of crystal. The layer is about 700 μm-thick.

The energy resolutions at several energy points are measured using line-γ peaks from the major γ-ray sources: ^{152}Eu, ^{137}Cs and ^{85}Sr. These values, as

	Ge 0	Ge 1
Serial Number	28-TP 10070	28-TP 10096
Length(mm)	73.8	67.4
Diameter(mm)	58.3	60.3

Table 3.2: Crystal size of germaniums

plotted in Fig. 3.5, are fitted with linear function. The results of fit are good enough such that they can be used for smearing of the energy distribution from the Monte Carlo simulation. Throughout the measurement, lead sheets of 2.0 mm-thickness are placed in front of the two detectors as seen in Fig. 3.4. They suppress events such that two or three low-energy γ's from an o-Ps 3γ decay, simultaneously hit one of the germanium detectors and behave as a high energy γ.

The absolute peak efficiencies with the lead shield in front are measured using ^{152}Eu. It has various line-γ peaks and their relative strength are well known and can be found in the data sheets [63]. The line-γ peaks are measured by placing ^{152}Eu at the center of the o-Ps formation assembly. Then the absolute peak efficiency curve is obtained by dividing each peak count by relative peak strength. On the other hand, the efficiencies are estimated by Monte Calro simulation assuming the same setup geometry. As shown in Fig. 3.6, the measurement and the simulation shows a good agreement throughout the whole energy range.

The solid angles as to the point source are about 5.7% and 6.0% (of 4π) for Ge0 and Ge1 respectively.

NaI(Tl) scintillators

Four large cylindrical NaI(Tl) scintillators (Scionix 127A127/5) are used to simultaneously measure the time and energy information from an each decay. As described in Fig. 3.7, size of the crystals are 127 mm $(\phi) \times$ $127mm$ (t) each, and each crystals are connected to 5-$inch$ photomultipliers (EMI-9390) to convert an optical information into a electrical signals.

Because they have much higher efficiencies compared to Ge detectors, while also having better time response function, the obtained time spectrum can be fit for o-Ps decay rate determination.

Four NaI(Tl) detectors are arranged as in Fig. 3.8 for the RUN I, their locations are optimized to totally obtain the highest solid angles of 31.7%, 10.0%, 10.0% and 8.1% (of 4π), where the number indices are referred to as in Fig. 3.8. The leads sheets of 2.0 mm are placed in front of the NaI-1, NaI-2 in the same manner as the Ge detectors, in order to suppress the Compton scattered low-energy photons to enter the detectors.

On the other hand, only one NaI(Tl) scintillator (NaI-0) is used in RUN

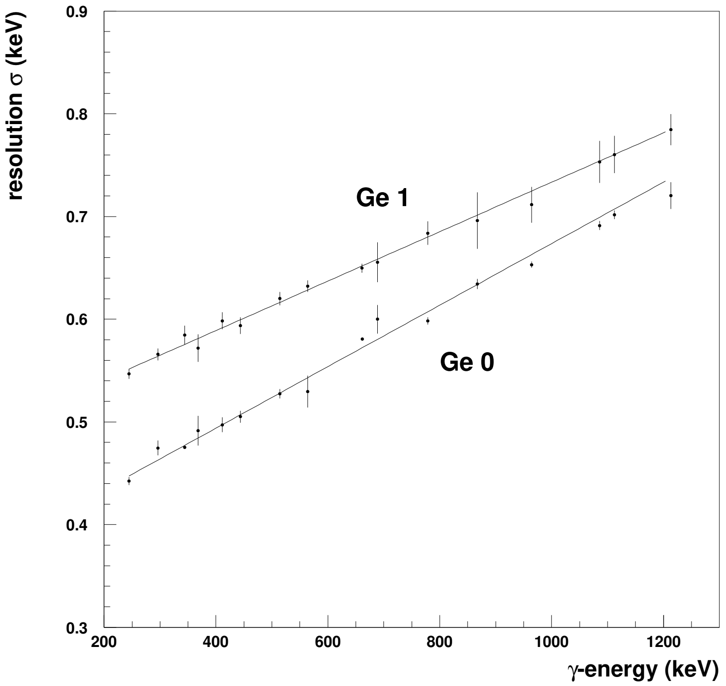

Figure 3.5: The energy resoluton of the Ge detectors as a function of the incident γ-energy. Energy resolution is expressed as the one standard deviation in keV unit. Obtained functions are, for Ge 0 : $\sigma = 0.374(2) + 0.299(3) \times 10^{-3} \times \text{energy}$, for Ge 1 : $\sigma = 0.493(5) + 0.291(9) \times 10^{-3} \times \text{energy}$

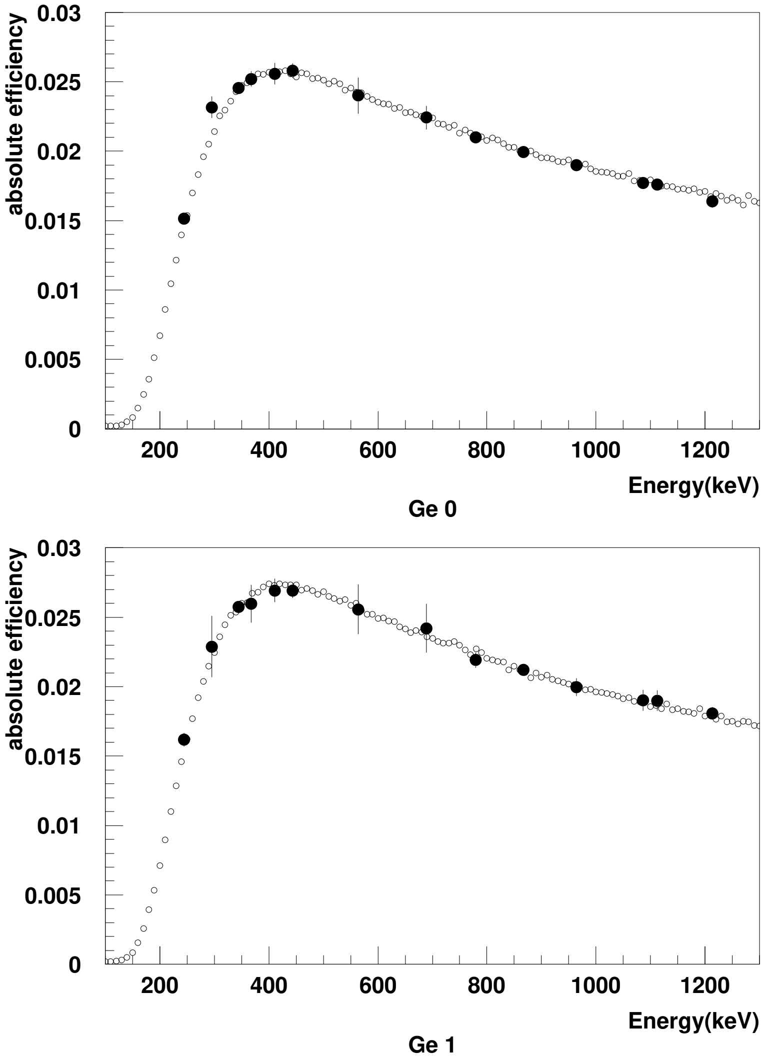

Figure 3.6: The absolute peak efficiency of the germanium detectors. Measured data using the ^{152}Eu source are plotted with large closed circles as a function of incident γ-ray energy. The small open circles represent the estimated relative efficiencies calculated with the Monte Calro simulation. The result of the MC are normalize so as to fit to the data.

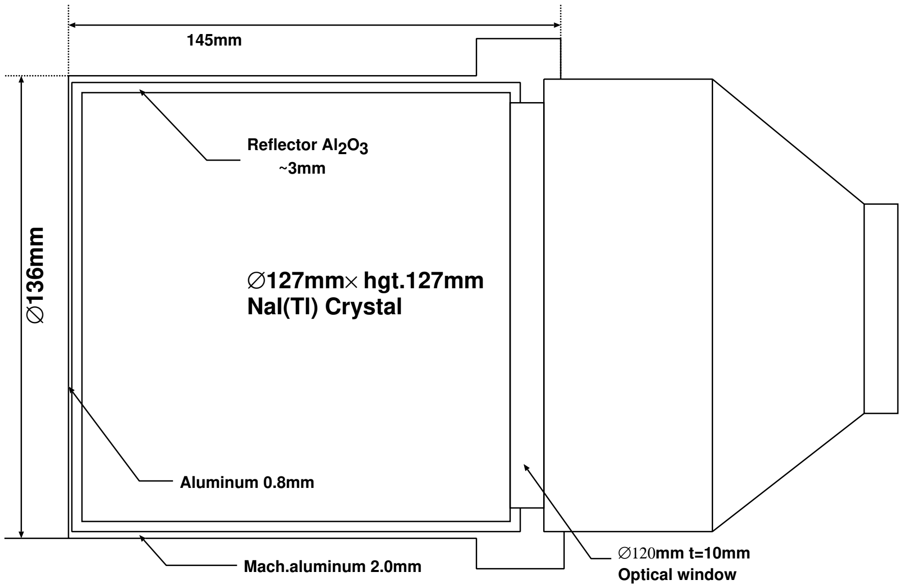

Figure 3.7: Schematic diagram of NaI scintillator.

II, because the cross-talk effects between the each NaI's have been a serious problem during the RUN I, which cause the large cutting inefficiency of the data ; this will be discussed at Sec. 4.3.2 in detail. To gain the solid angle as far as possible, position of the NaI-0 doesn't change from the RUN I.

The energy resolutions are measured using line-γ peaks from several γ-ray sources: $^{22}\mathrm{Na}, ^{137}\mathrm{Cs} and ^{133}\mathrm{Ba}$. These values are summarized in table 3.3, and is used in smearing the NaI(Tl) energy spectrum from the Monte Carlo simulation in the same manner as the Ge detectors.

Source	Energy (keV)	Resolution in σ (keV)			
		NaI-0	NaI-1	NaI-2	NaI-3
^{133}Ba	31.0	6.09	7.08	5.72	6.28
^{133}Ba	81.0	7.29	9.29	7.20	8.34
^{133}Ba	356.0	18.74	18.25	16.89	21.22
^{22}Na	511.0	21.18	25.07	22.11	31.96
^{137}Cs	662.0	21.99	24.42	21.37	32.02
^{22}Na	1274.5	35.42	36.59	30.60	60.23

Table 3.3: Energy resolution of the NaI(Tl) scintillator

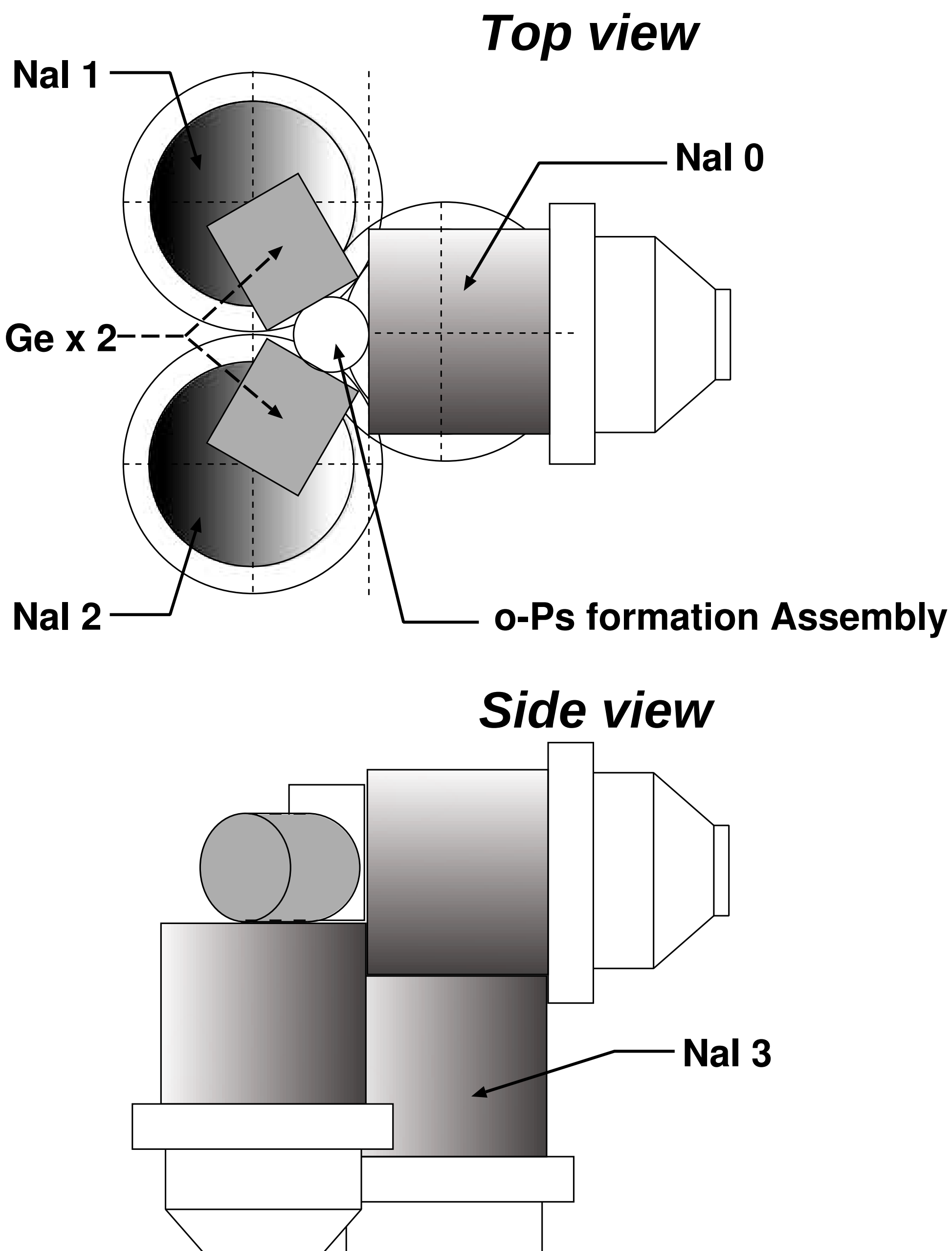

Figure 3.8: Geometrical location of the four NaI(Tl).

3.2.5 Electronics

The trigger and the data readout system is mainly consist of the clusters of NIM standard modules and the CAMAC data acquisition system. The data acquisition is performed with Linux operating system, which has been nowadays become a standard facility system operating for the CAMAC system. Between the Run I and II, the used electronics especially some of the modules are exchanged in accordance with the number of detectors employed.

For each detector component, the energy and timing information are taken, with which the highly statistical time spectrum can be finally produced.

Data flow

Figure 3.9 shows the data-flow of the total system. It mainly consists of three part, the trigger section, the NaI(Tl) section, and the Ge section. Each section has a *latch veto* structure where the gate-generator module is implemented in a latch mode. The latch of the trigger section, denoted as the *main-latch* in the figure, is *set* by the trigger signal itself, and *reset* by a pulse from the output register module of CAMAC system. The latchs of the NaI(Tl) and Ge sections, denoted as the *sub-latch* in the figure, are *set* by themselves and *reset* by the release signals from the trigger section.

The timing information is recorded with *time-to-digital converter* (TDC). TDC measures the time interval between the trigger hit (TDC start) and the detector hit (TDC stop). On the other hand, the energy information is obtained with *amplitude-to-digital converter* (ADC). ADC measures the charge (*charge sensitive type*) or the pulse height (*peak holding type*) of the signal during the gate input.

Details of the data-flows and the modules are described in following sections.

Trigger system

A schematic diagram of electronics for a trigger part is shown in Fig. 3.10. The following explanations enumerated by the indices are corresponding to the label within Fig. 3.10.

(t.0) The trigger PMT is operated at $-1200\ V$ for RUN I, and $-1150\ V$ for RUN II supplied from negative high voltage power supply (HV-TRI : Kaizu N450). Then output from the trigger PMT whose amplitude is about $-200\ mV$ for a mean positron energy of around 100 keV, is divided into three signals by a linear fan-out module (LFF : Lecroy 428F).

(t.1) One signal is directly fed into a fast leading edge discriminator (DISCRI : PHILIPS 708). In order to reduce the time-walk correction due

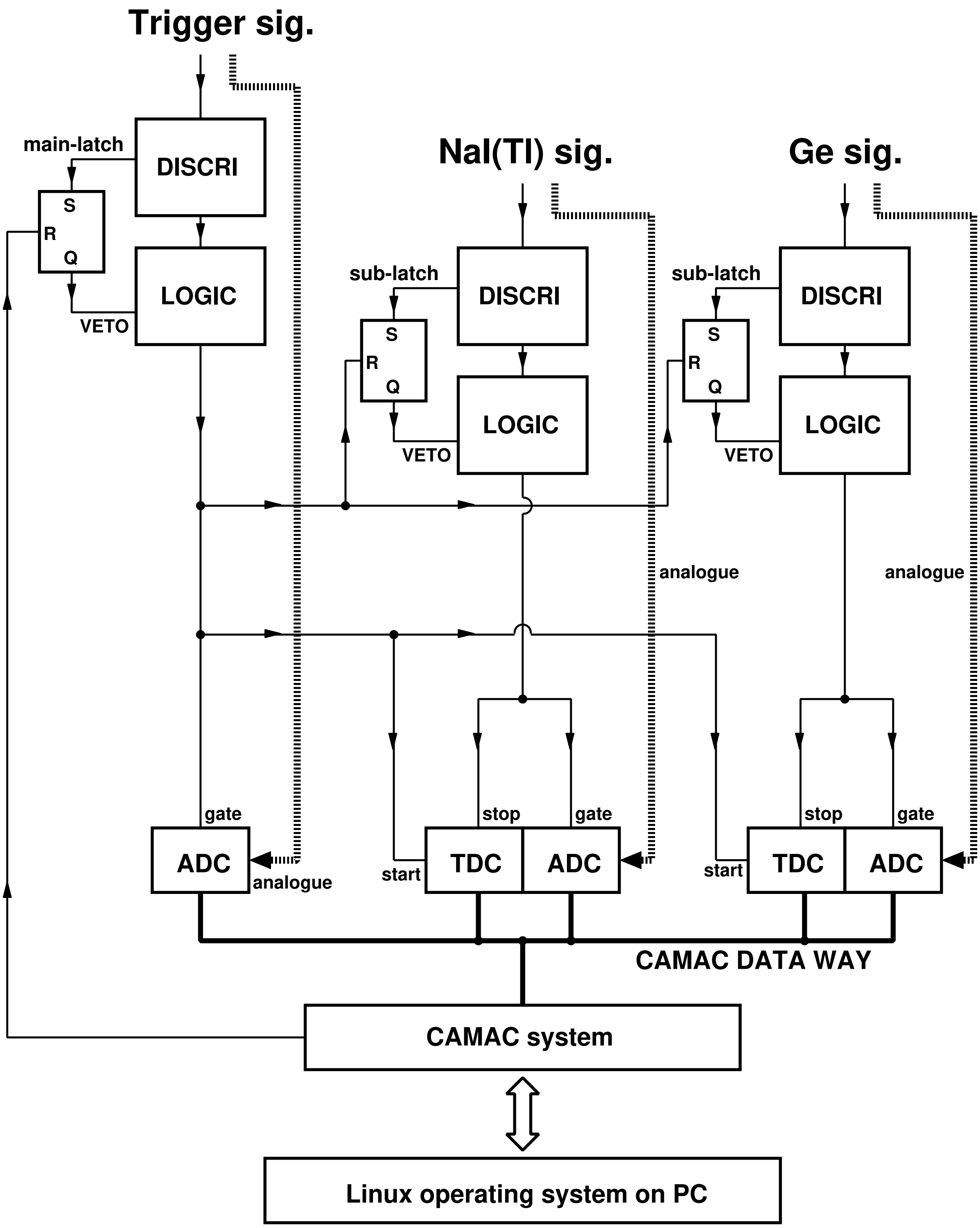

Figure 3.9: Schematic diagram of the process data-flow.

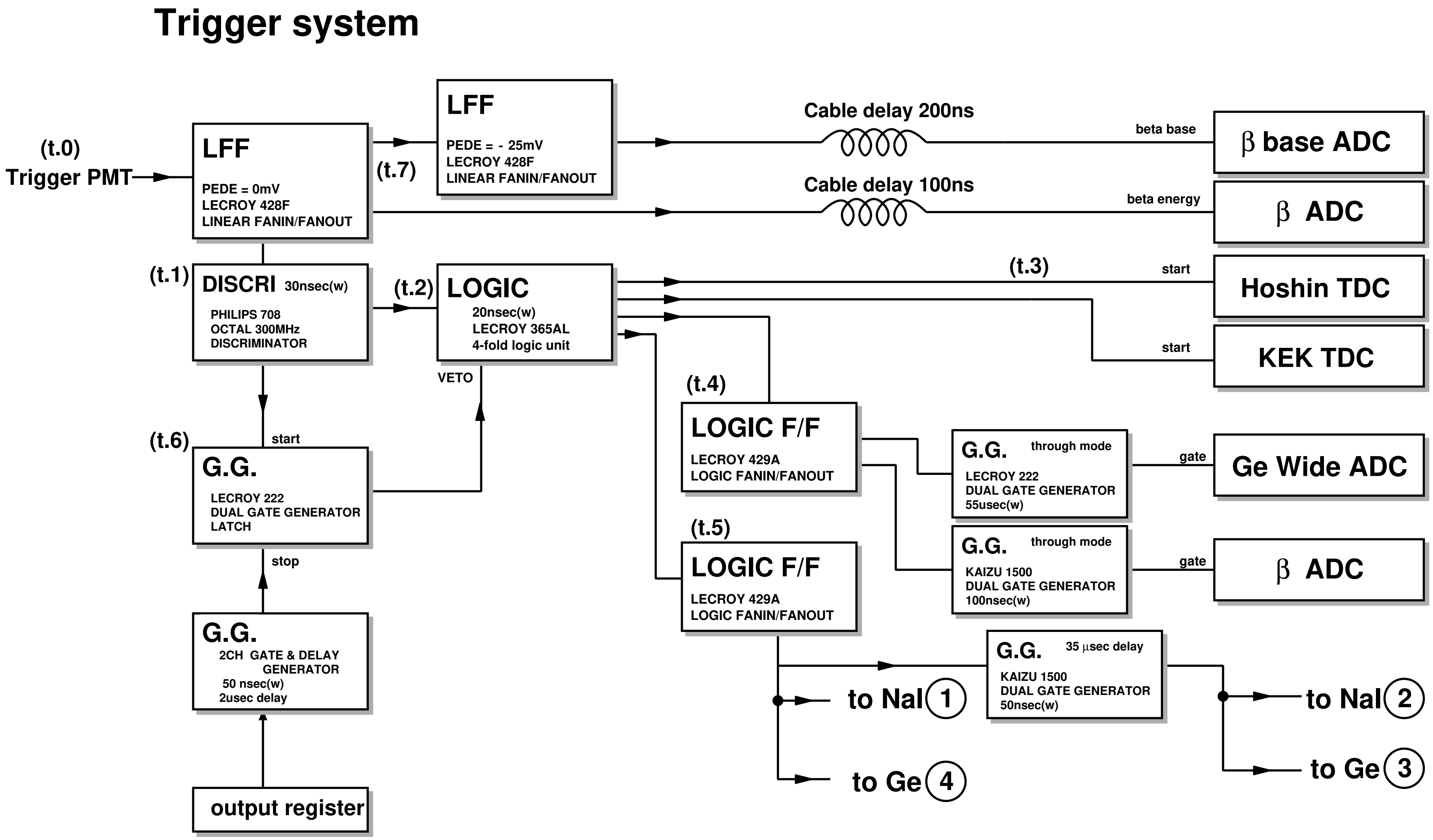

Figure 3.10: Schematic diagram of electronics for trigger system.

to the leading edge method, a threshold level of the discriminator is set as low as possible but which can effectively reject a single photon noise. The threshold value is fixed at $-65\ mV$ for RUN I, and $-62\ mV$ for RUN II; the high-voltage supply and the trigger PMT were so stable that there was no need to tune the threshold value during the RUN's.

(t.2) One of the output of the discriminator is fed into a logic unit (LOGIC : Lecroy 365AL) which produces four logic signals.

(t.3) Two of these outputs provide *common start signals* to two TDCs called KEK TDC and Hoshin TDC, which will be fully described in Sec. 3.2.6.

(t.4) Other output from LOGIC is divided by logic fan-out module (LOGIC FF : Lecroy 429A) and provides the gate-signals to a peak-holding type analogue-to-digital converter GE-WD (PHADC : Hoshin C011) for the precise energy measurement of Ge detectors, and a charge sensitive type ADC (CS ADC : Lecroy 2249A) which measures the energy information of the β^+-itself. These gates are generated by gate-generator (G. G. : Lecroy 222 for PHADC, Kaizu 1500 for CS ADC) with a 55-μs and 100-ns gate width for PHADC and CS ADC respectively.

(t.5) The other rest from LOGIC is also divided by LOGIC F/F and provides a release signals for all the veto systems of both the NaI and the Ge part of the electronics (see, Sec. 3.2.5, 3.2.5). These release signals wake up the timing system of all the γ-detectors which have been inhibited (vetoed) since after obtaining their previous hit.

On the other hand, the same output from LOGIC F/F is delayed by 35 μs (which is a full range of a KEK TDC), and provided to the LOGIC module of both NaI(Tl) and Ge section, as a force veto (these signals are denoted as ② and ③ in Fig. 3.10, and reappear in (n.4), (g.2) at the NaI(Tl), Ge section respectively).

(t.6) The other output from the DISCRI is fed into a gate-generator which is operated in a latch-mode (LATCH : Lecroy 222), then output from the LATCH module goes into a veto input of the LOGIC module. This veto signal inhibits the succeeding trigger signals from going through the LOGIC unit during the data-taking period, and controls the entire timing system by separating the sequence of trigger events one by one.

This *trigger latch* is released by the logic signal from the CAMAC output register module at 2 μs after the CAMAC system having finished their measurements and the data taking system have decided to move onto the next events.

(t.7) The rest channels from the first LFF are used to measure the information of β^+ itself. One of which is fed into a CS ADC after passing through the 100-ns cable delay : with this delay, the gate pulse of CS ADC in (t.4) can wholly cover the period of signal duration. From now on, this ADC output is denoted as B-EN (beta energy) and has a 11-*bit* ADC information.

On the other hand, the rest of the output is again fed into a LFF in order to have a -25-mV pedestal, and then after passing through the 200-ns cable delay the base-line condition of the β^+ is measured by CS ADC : this delay time is adequate for measuring the base-line condition of the signal just prior to the event. This ADC output is denoted as B-BS (beta base) and also has a 11-*bit* word.

Electronics for the NaI(Tl) scintillator

A schematic diagram of electronics for a NaI(Tl) scintillator part is shown in Fig. 3.11. The logic described in the figure is for a just *one* NaI(Tl) system, and essentially the independent four systems are prepared for RUN I. On the other hand, in RUN II, the systems decrease to one in accordance with the number of the NaI(Tl) scintillators used.

As in the description of trigger part, the following indices are corresponding to the labels in Fig. 3.11. Basically the following enumerations explain the data-flow for a one of the four NaI(Tl) systems.

(n.0) The photomultiplier for an each NaI(Tl) scintillator is operated with the appropriate high voltage provided by the positive high voltage supply module (HV-NAI : Repic RPH-021). The anode output of photomultiplier is fed into a photomultiplier Amplifier (PM AMP : Lecroy 612A) whose gain is fixed at 10×. Its high stability of 1mV DC, and high integral linearity of 0.1% enable the ADC to measure the correct energy information from NaI(Tl). The fast rise time of less than 3 ns (from 10% to 90% of the signal) insures the good reproduction of the raw signal. The output from PM AMP is divided into four lines with a linear fan-out module (LFF : Lecroy 428F). In order to suppress the time jitter and obtain the good signal-to-noise ratio, the outputs from the LFF are integrated with 23.5 ns time constant.

(n.2) One of the divided signals is fed into a fast leading edge discriminator (DISCRI : PHILIPS 710). As the maximum pulse-height of the single photon noise of the used NaI(Tl) scintillator is about -7 mV, threshold value of -10 mV is enough to reject them effectively; in fact -10 mV is the minimum threshold value the DISCRI can provide.

In RUN II, another gate-generator (G. G. : Kaizu 1500) is used to inhibit the DISCRI from making outputs other than the first leading edge of the signal. This G. G. is drawn inside the dashed area in Fig 3.11 While the whole NaI(Tl) system is vetoed at (n.3), it is desirable

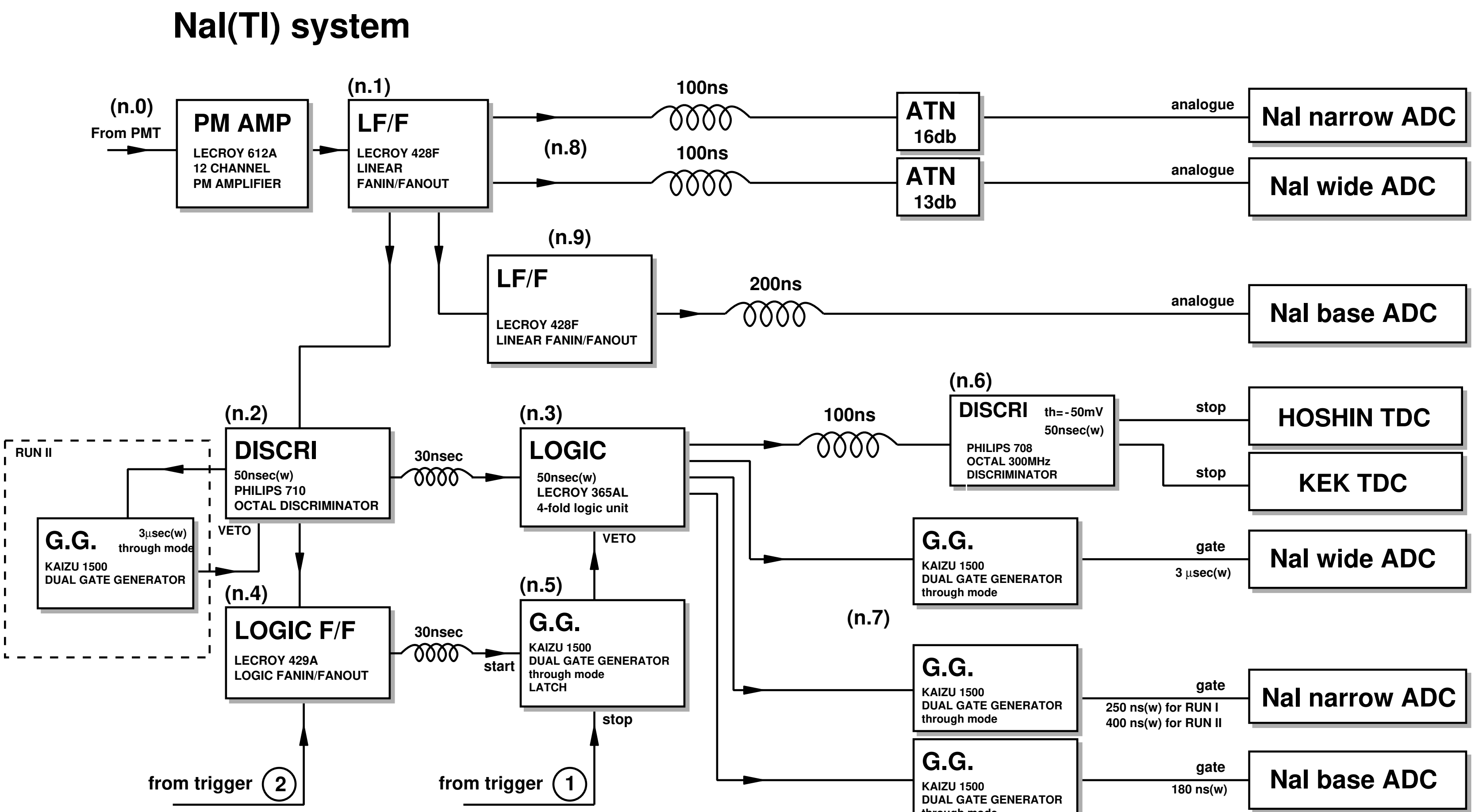

Figure 3.11: Schematic diagram of electronics for NaI(Tl) scintillator system.

to limit the DICRI outputs to one corresponding to the first leading edge; because DISCRI sometimes hits at the tailing edge of the NaI(Tl) signal, such as around $t = 600$ ns, in that range the 3γ-component of o-Ps decay still makes the large contribution to the time spectrum fitting procedure.

(n.3) The output of the DISCRI is fed into a logic unit (LOGIC : Lecroy 365AL) after passing through 30-ns cable delay, and divided into four lines. This 30-ns delay has a role of keeping the NaI(Tl) signal to enter LOGIC, after the veto-reset signal from the trigger part arrives.

(n.4) The other output from the DISCRI is fed into a logic fan-in module (OR : Lecroy 429A). In OR module this signal is *ORed* (logically added) with the *force veto* signal from the trigger part (in Fig. 3.11, this signal is denoted as ②); this force veto inhibits the NaI(Tl) signals from going through the LOGIC after 35-μs having passed from the trigger timing. It prevents the accidental events from passing through the LOGIC at the time interval between the CAMAC hardware clear, and the next trigger. If it were no force veto as described above, such extremely slow accidental events would leave their footprints on only ADCs and not on TDCs, then these ADC values would pretend as if they were measured at the next event.

(n.5) The output of OR module is provided into a gate-generator which is operated in a latch-mode (LATCH : Kaizu 1500). The output from this LATCH vetoed the LOGIC from about 20-ns after the NaI(Tl) signal timing till the next event, that is arriving of the reset signal from trigger part (in Fig. 3.11, this signal is denoted as ①)

(n.6) After the LOGIC module, one of the outputs is divided by fast leading edge discriminator (DISCRI : Philips 708) and used as the stop signals for two types of TDCs. This line is delayed with 100-ns cable line guarantying that the start signal of TDC is always in advance of the stop signal.

(n.7) The rest three outputs from the LOGIC module are fed into the gate-generators (G.G. : Kaizu 1500) providing three different gates to three charge-sensitive ADCs for different purposes. One ADC with 3-μs gate width, called NAI-WD (Wide ADC: Lecroy 2249W), measures the whole charge for the duration of the signal concerning the typical decay time constant of NaI(Tl) of about 230 ns; In order to correct the whole charge including the long decay tail, more than 2 μs is needed for a gate.

While the long gate can cover the whole signal, it suffers from the pile-up effect as well. Therefore we need the other information that is sensitive to the pile-up of the signals. The other ADC called NAI-NW (narrow ADC : see table 3.4 for module type) measures the signal charge with narrower gate-width (250 ns for RUN I, 400 ns for RUN II). As can be seen in Fig. 3.12, comparison of the two value from

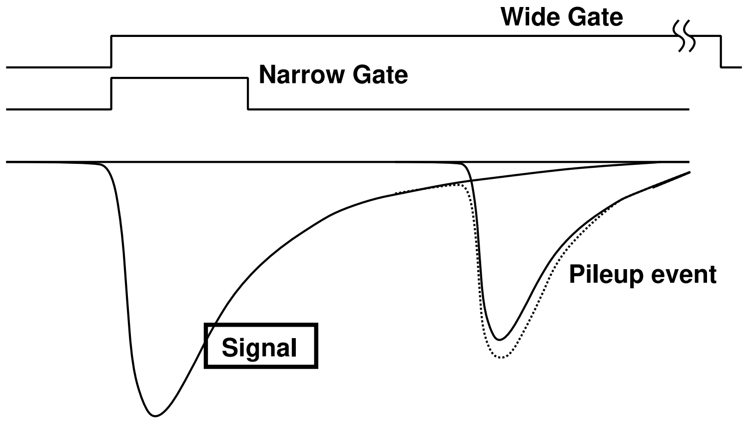

Figure 3.12: The timing chart of the NaI(Tl) signal. The relation between the narrow gate and the wide gate is presented.

different ADC enables us to effectively reject the pile-up events, as they results in larger value on NAI WD than on NAI NW.

The last type of ADC is called NAI-BS (base ADC : see table 3.4 for module type). It measures the base-line condition of the signal just prior to the event. The timing relations between the gates and the

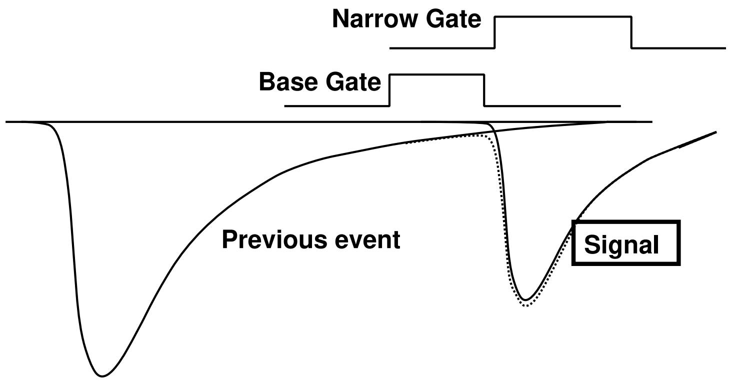

Figure 3.13: The timing chart of the NaI(Tl) signal. The relation between the narrow gate and the base gate is presented.

signals are schematically illustrated in Fig. 3.13. As in the figure, if the NaI(Tl) hits within a tail of the previous events, i.e. the accidental events occur just before the system veto reset, the output of the WD NAI is larger than intrinsic value because of the pile-up effect. This kind of pile-up events can be effectively rejected by monitoring the NAI-BS.

Definite names of the ADCs are listed in Table. 3.4. The fact that the large number of modules are needed to provide each NaI(Tl) with independent gates is compensated by the special ADC which provides 12-channel ADC with separate gates (SG ADC : Lecroy 2249SG).

Conventional name	RUN I		RUN II	
NAI WD	for NaI-0~NaI-3	2249W	for NaI-0	2249W
NAI NW	for NaI-0	2249W		
	for NaI-1~NaI-3	2249SG	for NaI-0	2249W
NAI BS	for NaI-0	2249A		
	for NaI-1~NaI-3	2249SG	for NaI-0	2249A

Company	Model	Supported gate-width	# of bits	Comments
Lecroy	2249A	10-2,000 ns	10	
Lecroy	2249W	30-10,000 ns	11	wide gates
Lecroy	2249SG	10-2,000 ns	10	separate gates

Table 3.4: List of modules used for NaI(Tl) system in two RUNs and list of their features.

(n.8) The two channels from the first LFF are fed into ADCs (NAI-WD, NAI-NW) as an analogue inputs respectively. The lines are retarded with BNC cables in order to tune the timing for the gates, and attenuated with the coaxial attenuator in order to fit the dynamic range of each ADC.

(n.9) The last channels from the first LFF is again fed into a LFF in order to keep a -30-mV pedestal. Then the analogue output of the second LFF is delayed precisely for reaching ADC a little prior to the signal.

Electronics for the germanium detectors

This section explains the electronic scheme for a Ge detector section in accordance with the Fig. 3.14. The logic is described for just a one Ge system same as NaI(Tl) system. The only difference between the two Ge systems is the type of spectroscopy amplifier, which makes no difference within the application for the present measurement.

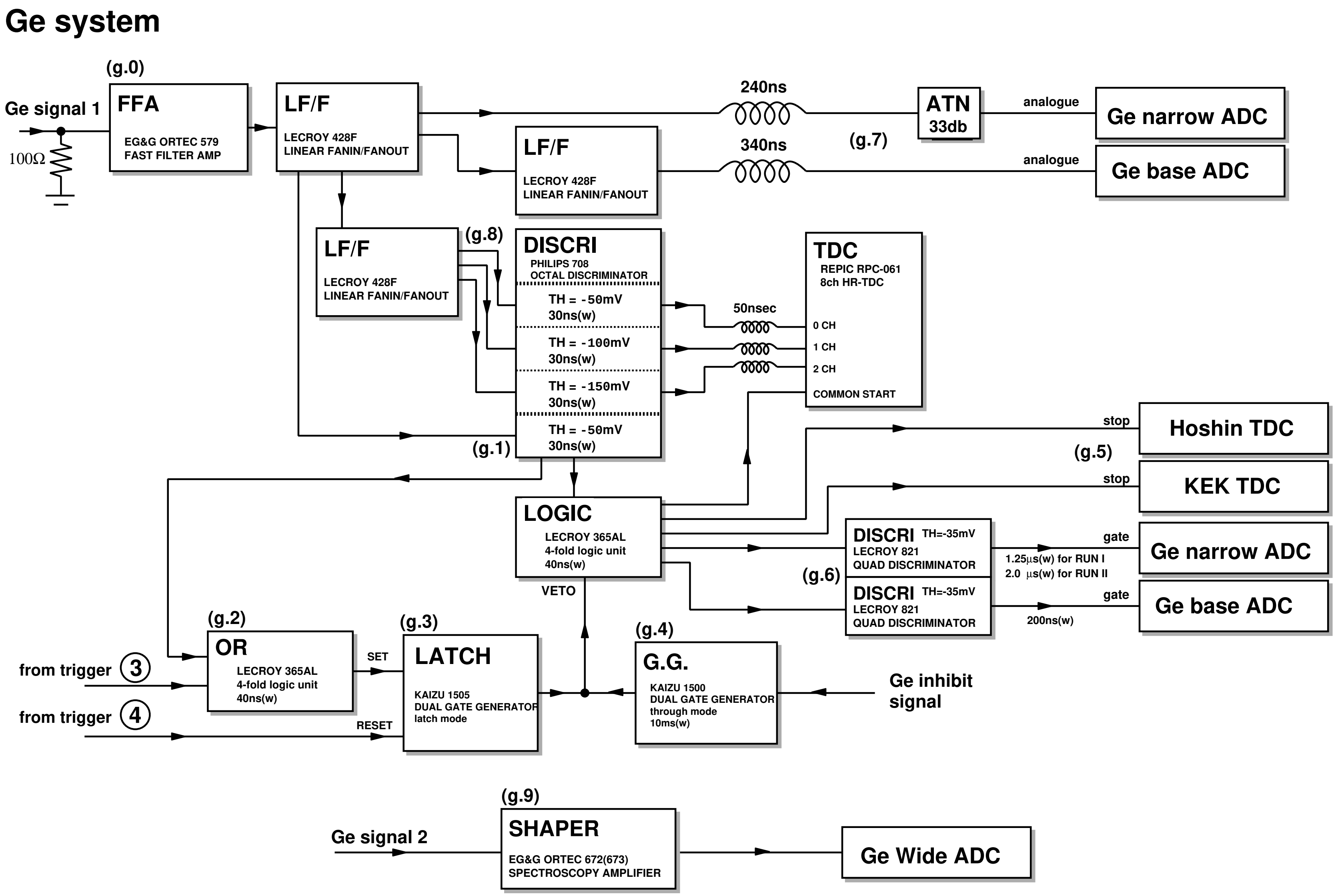

Figure 3.14: Schematic diagram of electronics for Ge detector system.

High voltage power supply The HV values are optimized by manufacturer according to the quality of crystal, i.e. +2600 V for Ge 0, and +2000 V for Ge 1. They are supplied from bias supply module (BIAS : EG&G ORTEC 459) through the HV buffer (BUF : SEIKO EG&G DS-1550) in apprehension for the accidental power cut.

Outputs from pre-amplifier The pre-amplifier (or FET) provides the two identical signal outputs, the inhibit signal, and the shutdown signal. One of the signals is mainly used for the timing measurement, and the other is used for the precise measurement of the energy information. The inhibit signal is synchronized with the transistor reset pulse (TRP) of the pre-amplifier. Frequency of the TRP is depending on the vacuum condition of the cryostat. Typically rate of about 10 Hz is expected, and this signal is used to veto the electronics for Ge system.

(g.0) The first output from the pre-amplifier (Ge signal 1) is fed into a fast-filter amplifier (FFA : EG&G ORTEC 579). The differentiation (200 ns) and integration (50 ns) time constants of the module are optimized in order to obtain a good time resolution. Then the output from the FFA is divided into four by linear fan-out module (LFF : Lecroy 428F).

(g.1) One of the outputs from LF/F is directly fed into a fast leading edge discriminator (DISCRI : PHILIPS 708) to generate the timing information. Logically the adopted scheme in here is similar to the one in the NaI(Tl) system, namely one of the outputs from the DISCRI is fed into a logic unit (LOGIC : Lecroy 365AL), while the other is used as a set signal for the veto latch.

(g.2) The *set* signal for the gate-generator which is operated in a latch mode (LATCH : Kaizu 1505) is an *ORed* (logically added) signal of the DISCRI output, and the *force veto* signal from the trigger part (in Fig. 3.14, it is denoted as ③). Why this force veto is beeing required has been already described in the (n.4) of the NaI(Tl) section.

(g.3) In order to prevent the second hit from accidentally disturbing the data-taking system, the output from the LATCH vetoes the LOGIC during the data taking period. The veto is reset by a reset signal from trigger part (in Fig. 3.14, this signal is denoted as ④).

(g.4) The LOGIC is also vetoed for a short time when the TRP (transistor reset pulse) is generated. Veto duration of 10 $msec$ is required for the FFA to thoroughly recover the saturated base-line.

(g.5) Two outputs of the LOGIC are used as the stop signals for two types of TDCs. Detail description for these TDCs will be seen in Sec. 3.2.6.

(g.6) Other outputs from the LOGIC are used for generating gate-inputs for the ADCs; these gates are generated with a fast leading edge discriminator (DISCRI : Lecroy 821) that has been remodeled to be able to produce a longer gate width.

Just like the case in NaI(Tl), the pile-up problem is resolved by measuring the energy with narrower gate width. The charge-sensitive type ADC called GE-NW (narrow ADC: see table 3.5 for module type) measures the Ge signal with narrower gate-width (1.25 μs for RUN I, 2.0 μs for RUN II).

On the other hand, another charge-sensitive type ADC called GE-BS (base ADC: see table 3.5 for module type) measures the base condition of the Ge base-line just prior to the signal.

Conventional name	RUN I	RUN II
GE WD	C011-2	C011-2
GE NW	2249SG	2249W
GE BS	2249SG	2249W

Company	Model	gate-width	# of bits	Comments
Hoshin	C011-2	$500ns-$	12	Wilkinson peak-holding type

Table 3.5: List of ADC modules used for Ge system during two RUNs and their features. The same type modules already described at NaI(Tl) section are omitted.

(g.7) The two outputs from the first LF/F are fed into two ADCs (GE-NW, GE-BS) as the analogue inputs. One is provided to GE-NW after passing through the 240-ns cable delay and 33-db coaxial attenuator. The rest is again fed into another LF/F in order to gain a pedestal of $-20\ mV$. Then after passing through the 340-ns cable delay, this output is provided for GE-BS.

(g.8) Since *RCPD method* is adopted in this thesis instead of the ARC method (See Sec. 3.2.6 for a detail description), the three thresholds discriminator is prepared. The threshold values are set at $-50mV$, $-100mV$, and $-150mV$, that is, the smallest value ($-50mV$) is identical to the value of the first discriminator (g.1). After discrimination, the signals are fed into a high-resolution time-to-digital converter (TDC : Repic RPC-061) having 12-bit dynamic range and 1-μs full scale.

(g.9) The second output from the pre-amplifier (Ge signal 2) is independently fed into a spectroscopy amplifier (SHAPER :EG&G ORTEC 672 for RUN I, 673 for RUN II). Amplified with 6-μs time constant, the uni-polar output of the SHAPER is provided to a Wilkinson type peak-holding ADC called GE-WD (PHADC : Hoshin C011-2). The ADC gate is provided with 55-μs width from trigger system (See trigger part (t.4)).

3.2.6 Timing system

RCPD method

Since the typical rise-time of the FFA output is order of about 50$nsec$, the careful operation must be performed in extracting the intrinsic signal timing. In addition, an electric field inside an large volume coaxial germanium detector has a local inhomogeneity, and this results in the various rise-time signals. There is a bunch of slow rise-time signals which easily disturb the timing information. Hence the special care must be paid for the timing correction.

For a Ge timing spectroscopy, the well established method, for instance *the amplitude-and-rise-compensated* (ARC) method [64, 65] is generally used. With this method by using the hardware module, for instance the *constant fraction discriminator* (CFD), one can produce the timing signal online. By optimizing some hardware parameters, the good time resolution can be obtained. Furthermore slow rise-time (SRT) signals can be rejected if the SRT reject switch is *turned on*.

The last measurement [7] adopted this method and the good time resolution of 6 ns was obtained. However since the timing information of the Ge system plays a crucial role throughout the measurement, it is strongly desired to record the whole information as to the signal rising, and produce the timing signal in the off-line analysis, rather than operating online by putting everything in a hardware module.

Therefore we adopt here a completely original technique called **rise-time compensation by plural discriminators (RCPD)** method. Conceptually RCPD method is same with ARC method, except that while ARC method performs entire procedures on-line, the RCPD method records the rise-time information data and performs equivalent process at off-line analysis.

Concrete electronics has already shown in Fig. 3.14, where the DISCRI (g.8) with three-level thresholds is located in the center of the figure. With the timing signals from these three-threshold discriminator, the shape of the signal rising is easily inferred as in Fig. 3.15 and the intrinsic signal timing can be reconstructed using simple extrapolation, i.e.,

$$T_{intrinsic} = T_{50mV} - \alpha \times (T_{100mV} - T_{50mV}), \tag{3.11}$$

where $T_{<th>mV}$ represents the discriminator's hit timing and <th> stands for the absolute value (actual value < 0) of its threshold, and α is an empirical value that must be determined by minimizing the time resolution and

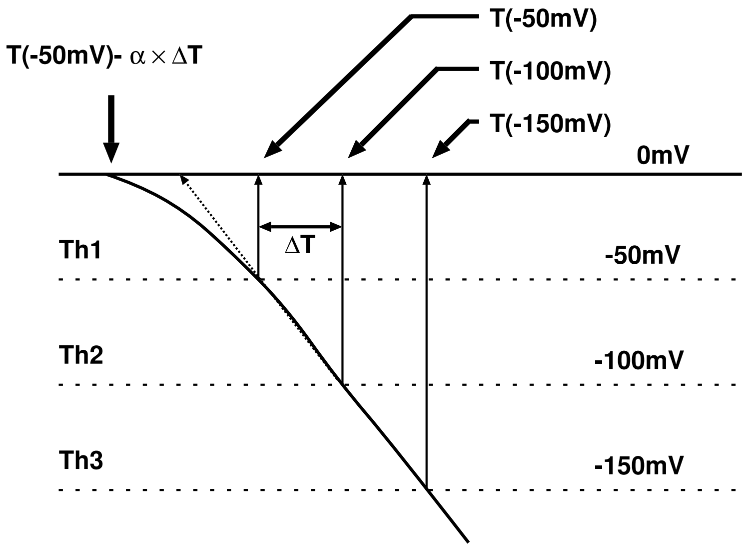

Figure 3.15: Schematic figure explaining the RCPD method. Typically the factor α is determined to be $1.6-1.7$ in extraction of intrinsic signal timing.

by optimizing the time response function; this factor will be discussed in Sec. 4.1.4. A typical value of α is around $1.6-1.7$. Figure 3.16(a) shows the relation between the two time intervals, $T_{100mV}-T_{50mV}$ (X axis) and $T_{150mV}-T_{50mV}$ (Y axis). From this contour plot, one can easily find the peak of the slow component; it is centered around $T_{100mV}-T_{50mV}=50-100$ ns. By cutting the off-diagonal components and the slow rise-time events as indicated in the figure, one can cleanly reject the slow rise-time component, which is shown in Fig. 3.16(b).

Development of the new TDC module

Because present measurement simply *measures the time itself*, the performance, of the TDC, i.e. the linearity strongly affects the final result.

Generally speaking, there are roughly two types of TDCs commercially available, those are *Inner ADC type* and *Direct clock counter type*. Their advantages and disadvantages are as followings,

TDC (Inner ADC type)— This type of TDC has a time-to-amplitude converter (TAC) inside, where TAC converts a time period between two logic pulses into an output pulse whose height is proportional to this duration. The converted amplitude is then digitized using ADC, that the linearity of the TDC directly depends on this built-in ADC.

If *the Wilkinson type ADC* is used, because of a high stability oscillator, the integral-non-linearity (INL) is expected to be quite small;

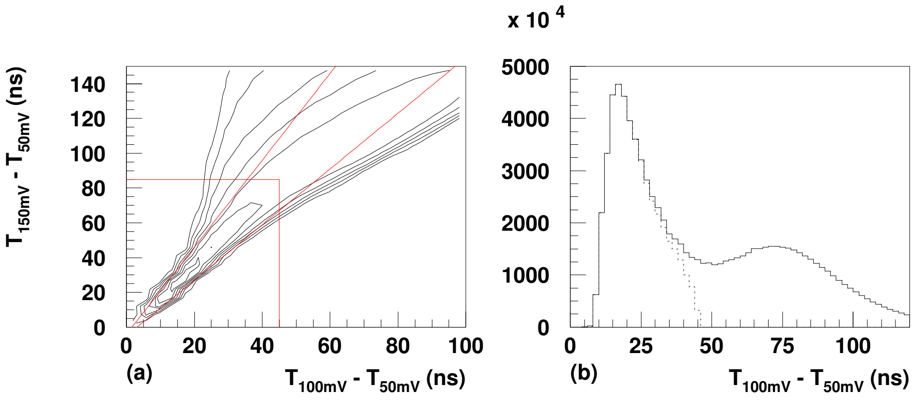

Figure 3.16: (a) The relation of the two time intervals, $T_{100mV} - T_{50mV}$ (X axis) and $T_{150mV} - T_{50mV}$ (Y axis). Two oblique lines and small box indicate the boundaries of the cutting condition. (b) The time distribution of $T_{100mV} - T_{50mV}$. Solid and doted lines represent the distributions of the before and after the SRT rejections.

it is the order of the oscillator's precision, i.e. from 10^{-5} to 10^{-6}. Instead, the differential-non-linearity (DNL) is expected to be large. Because Wilkinson type ADC counts the pulses from oscillator during the gated on (the gate period is proportional to the input amplitude), dependence of gate-period on the scaler's content directly shows up as the DNL. Therefore *if* the gate-off section of the module is *not* completely independent of the scaler's section, the gate-off timing is slightly affected by the fluctuation of ground plane of scaler part due to the bit shift. Actually, the typical size of DNL for Wilkinson type ADC is $2 - 3\%$; in the commercial data book the general values are $< 10\%$.

On the other hand, if *the successive approximation type ADC* is used , the INL is the order of 0.1% due to the intrinsic non-linearity of this ADC type. However the DNL is not small as well, that is the same order of magnitude with the Wilkinson type.

TDC (Direct clock counter type)— The basic principle of this TDC is to use the Start-signal to gate-on a scaler which counts a constant frequency oscillator. At the arrival of a Stop-signal, this scaler is gated-off to yield a digital count proportional to the time interval during the gate-on. Thus with the same reason described at the Wilkinson type ADC, this type of TDC suffers from large DNL.

The commonly available TDCs are listed in table 3.6 with the expected INL and DNL values from their Data-Book. In principle, the non-linearities as

Type of TDC	Company	Model	DNL	INL	comments
Direct clock	Hoshin	C006	$2-3\%$	—	23bit data
	Lecroy	4208	—	$< 0.1ppm^*$	length
ADC successive	Repic	RPC-061	$< 10\%$	$< 0.1\%$	
approximation	Phillips	7186	$\pm 10\%$	$< 0.1\%^*$	4counts 12bit
ADC Wilkinson	Lecroy	2228A	$< 10\%$	$< 0.1\%^*$	2counts 11bit

Table 3.6: List of TDCs available from the commercial base. The DNL and the INL are listed in the columns. The INL values marked with * at the right shoulder indicate the values which are deduced from the counts as in the *comments* column.

described above could be corrected with the data taken at the calibration run. However such calibration data needs to be a high-statistic comparable to that of the decay rate measurements, the calibration run itself is required to be a *long* run. In addition, in order to reproduce the main runs, setup condition, especially the electricity consumption must be equivalent to that of the main runs.

From above sense, it is strongly desired to develop a new TDC that will suit to a purpose of the present experiment. An exhaustive cooperation by the staffs of an Electronics Facility of High Energy Accelerator Research Organization (KEK) in Tsukuba Japan, we can develop an entirely new and completely original TDC. This TDC is referred to as a KEK TDC in this thesis.

As a reference purpose, the other TDC (Hoshin : C006) is used at measurement in parallel with KEK TCD. Principle features of the Hoshin TDC are,

- A direct clock count type TDC containing 200MHz internal quartz oscillator.
- Intrinsic time resolution of 5 ns determined by the clock frequency.
- 12-bit dynamic range and full scale of 20 μs.
- Using common start mode same as KEK TDC.

Picture 3.19 shows the front view of the KEK TDC module. KEK TDC is a direct clock counting type 8ch TDC, packaged in a single width CAMAC module. As can be seen in the picture, the front panel is equipped with 11-LEMO inputs; 8-channel of them are fast negative NIM direct coupled inputs work as stop signals, the others are the COMMON START, the COMMON

STOP, and the fast CLEAR signal. KEK TDC measures the time span between the COMMON START and the each channel. Digitization starts with the COMMON STOP input.

The center of the front panel is a *SMA* connector accepting the external 2 GHz oscillator as a clock source.

The external clock source is a DDS-PLL synthesizer, DPL–2.5G from Digital Signal Technology Inc. DPL–2.5G is wide band clock source utilizing Direct Digital Synthesis (DDS) and Phase Locked Loop (PLL) technique. It provides pure signal output from 700 MHz – 2.5 GHz in 10 Hz steps. Frequency compensated internal 10 MHz clock provide high stability in wide range temparature. The stability of internal clock frequency is guaranteed as, ± 2.5 ppm against the temperature $-10°C$–$+50°C$, ± 3 ppm against one year.

For the present measurement, the clock frequency is adjusted to 2 GHz within a 1-ppm level. Therefore with the 16-bit word length, the time range for each channel is $\underline{32\ \mu s}$, and one obtains the intrinsic time resolution of $\underline{0.5\ ns}$.

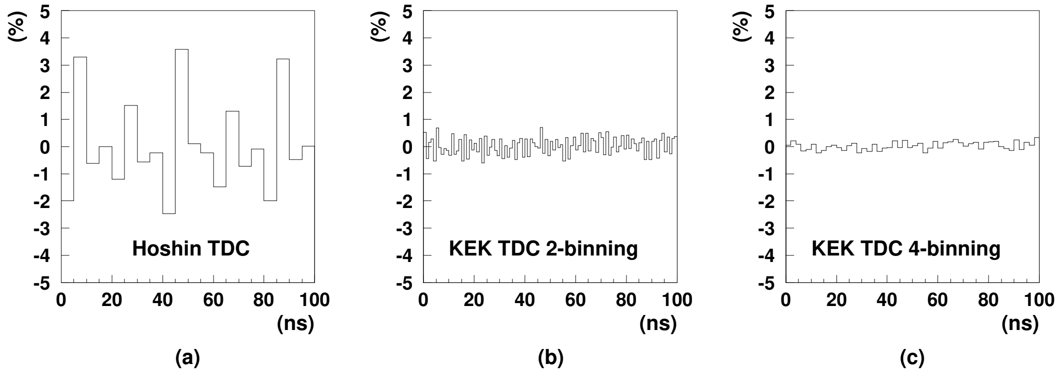

Figure 3.17: DNL distribution of the TDCs. (a) Hoshin TDC with no binning (b) KEK TDC with 2 bin width (c) KEK TDC with 4 bin width. The time resolutions are 5, 1, 2 ns respectively.

Since this TDC is a direct clock counting type, principally miscount never occur and the integral non-linearity is expected to be less than ± 1 count for 16-bit word length; this magnitude corresponding to less than 15-ppm INL. This means the extremely good absolute timing accuracy for the KEK TDC.

By the way, the evaluation of differential non-linearity is more difficult. Differential non-linearity refers to the variation in bin width over the measurement interval. One way to test it is to allow a source of random events, for instance the radioactive source to start the TDC and using a periodic signal as the stop. One can expect the result from this test setup, a flat time spectrum over the period of stop pulses, if there is no DNL.

Figure 3.17 shows the result of the test. From the figure, one can easily see the large improvement of DNL for the KEK TDC. The commercially available module, Hoshin TDC has a intrinsic DNL of $2-3\%$ for 5 ns resolution, while the KEK TDC has $0.4-0.5\%$ DNL for a binning operation of 2 bin width, and $0.1-0.2\%$ DNL for a binning operation of 4 bin width. In this test result, the statistical error can be neglected now, because the simple counting statistics ($\sqrt{N}$) show the (a) 0.06%, (b) 0.11%, and (c) 0.08% contributions for a each histogram. Figure 3.18 accounts for the

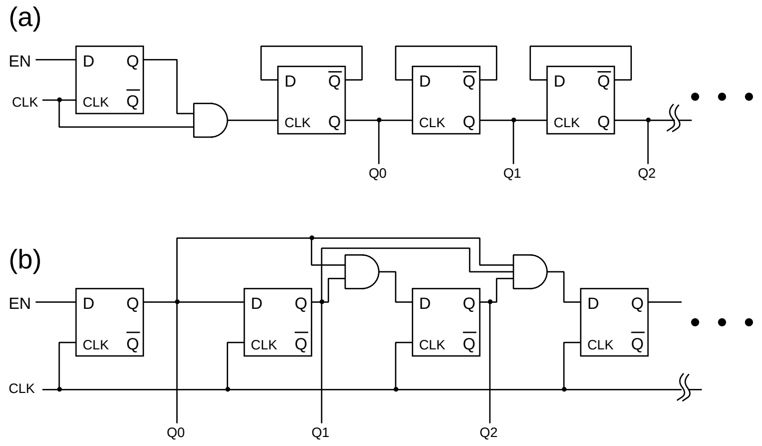

Figure 3.18: A comparison of two counter types. Two figures illustrate 3 least significant bits for (a) a ripple counter scheme (asynchronous mode) and (b) a synchronous counter scheme. The counter outputs are denoted as Q0, Q1, Q2 $\cdots$. The *EN* stands for the enable input, which is a gate signal between the start and stop signal.

reason for this improvement. Since the high clock frequency (2 GHz) is used for the KEK TDC, the asynchronous counting method is adopted as in the Fig. 3.18(a). This method transmits the clocks just like a ripple, and *only* the first flip-flop count the clock during the gate period. The remaining flip-flops merely hand over the received clocks to the next one. Therefore if ground plane of the module is stable against the counter's bit-shifts, one can expect a small DNL.

On the other hand, typical direct counting type TDC, as the Hoshin TDC, adopt the synchronous counting method as in the Fig. 3.18(b). The

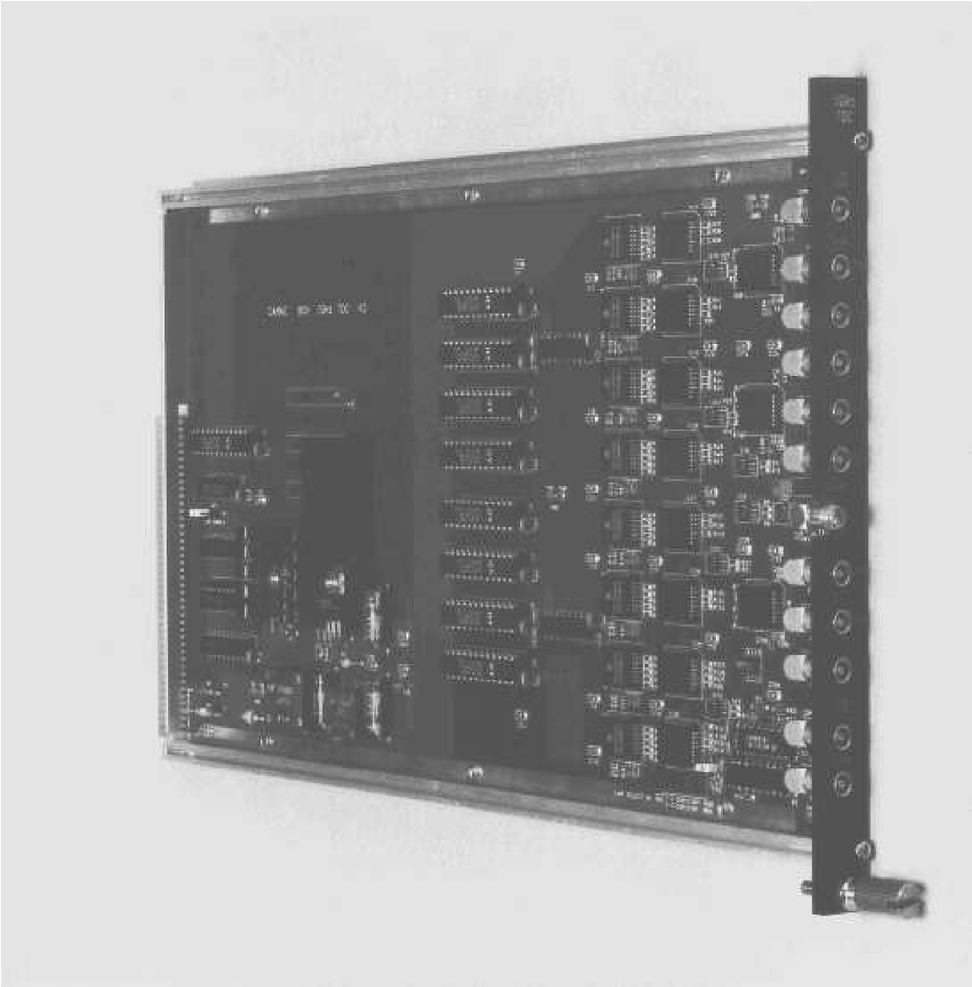

Figure 3.19: The front view of the KEK TDC

transitions of all flip-flops occur synchronously. This affects the ground level of the module so that the bin width varies according to the number of bit-shift. This phenomenon can be seen in Fig. 3.17(a) where the DNL is observed periodically as $2^n (n = 1, 2, 3 \cdots)$.

Although being suppressed enough, the KEK TDC also has the DNL from the same reason. The contribution to the measurements will be discussed in analysis section.

3.2.7 Data acquisition

Data acquisition is performed with the CAMAC system.

The system is composed of the CAMAC standard modules being placed across the two CAMAC Crates (Toyo Corp. PS7500). They are controlled through the CAMAC Crate controllers (Toyo Corp. CC7000) which occupy the last (right) two stations of each Crate. These two crate controllers are connected to a host computer in series, identified by the own crate address.

A host machine (Micron MILLENNIA PRO2) equipped with the CPU (intel pentium pro 200 MHz) is installed with LINUX of the kernel version 2.0.30. It operates the CAMAC functions through the CAMAC driver package (CAMAC Library for Linux OS version 2.0.29c) developed for the particular PC card (Toyo Corp. ISAcc7000, ISAcc7700, or PCIcc7700) by *online-group* at KEK.

The data taking starts at the LAM (*Look-At-Me*) signal from the trigger part. The B-EN and B-BS are measured at first, then the overflow bit of the KEK TDC is checked. If the overflow bits of all detectors are 1 (here 1 means the detector has no hit), one can simply discard this trigger cycle. In this case, the output register (OUTREG : Kaizu KC3471) of the CAMAC module distributes clear pulses to the clear-input of every CAMAC modules. Then system is preparing for the next trigger event.

If instead there is any hit, the data need to be obtained for only those hit detectors. Therefore the data length for each event varies according to the number of detector hits.

Since the data from each CAMAC module is orra length word, for instance 11-bit word, they are packed by specifying a range of values. This data compression saves considerably large disk space. The event header containing the trigger data is 32-bit length. For a one NaI(Tl) the 64-bit data length is prepared containing several ADC and TDC values. For a one Ge, the data length gets longer to be of 96-bit, resulted from the 3-threshold discriminator data. Therefore data size for a one-event varies from *3-long word* to *15(9)-long word* for RUN I (RUN II).

In order to resolve the variable data length for a one trigger event, the delimeter and the detector hit information bits are put inside the header part, which also serves as a verification of a bit missing or a bit flipping.

After the compression, data are saved on a hard disk. Frequently, these data are transferred to the DAT tape storages for a off-line analysis on the other machines.

The data-taking ends with the distribution of hardware clear pulses to each module in the same manner as no detector hit. Then as in Fig. 3.9 clear pulse also reset the veto of the trigger system 2-μs later from the hardware clears, assuring each CAMAC module being reset for the next event.

3.3 Monte Carlo simulation

A Monte Carlo simulation plays a crucial role in this measurement. It's chief purposes are,

– The accurate energy distribution of Ge detector at the present experimental setups is generated. The distribution is used for estimating the pick-off contribution of the 3γ decay of o-Ps.

– Some of the systematic errors are estimated with the Monte Calro simulations. The energy dependent relative efficiencies of the detectors are also studied with this simulation.

The simulation only deals with energy information of the γ-ray, and no timing information is concerned. The basic interactions of γ-ray with the materials, that is photoelectric, Compton (incoherent), and Rayleigh (coherent) scatterings are taken into account. Since the energy range concerned here is restricted to under 511 keV, the pair production is neglected. The geometries of the experimental setup and various materials are reproduced in detail.

The flow chart Fig. 3.20 outlines the logic of the simulation code for o-Ps 3γ decay. The simulation simply trace the step the o-Ps would actually do in reality. At first, the o-Ps is produced at the center of the assembly then transported according to the positron slowing-down processes [66] in the SiO_2 powder.

The o-Ps decays into 3γ-rays; the energy distribution of each photon is determined according to the $O(\alpha)$-corrected energy spectrum [67] which is offered as a table of the relative deviations from the tree-level energy spectrum. The directions of the photons are determined from the energy distribution.

Then a subroutine named *matter* is called. It returns the material type (Ge, NaI, Al, $\cdots$) at the position of the photon now we're following. Since the absorption coefficients for the basic materials are well known and currently available with a wide variety of means [68], the coefficients are calculated in subroutine called *absorption* utilizing the coefficient table prepared for each material.

The interaction type is then determined with the random number generated, only when the photoelectric or Compton scattering occurred that the photon energy is deposited to the materials. In the case of photoelectric, all the energy is deposited at the current material at one time, then the simulation proceeds to a next photon process. At the Compton scattering, the photon deposit part of its energy and change its direction according to the Klein-Nishina differential cross-section formula [69], until it loses all of its energy (or the energy reduced to be below some energy threshold).

The simulation repeats these processes for the 3γ while the energies deposited are successively added to the detectors. The energy deposited on detectors is smeared by the experimentally measured resolutions and the response functions. After finishing the 3γ processes, it independently starts the next o-Ps events from the beginning.

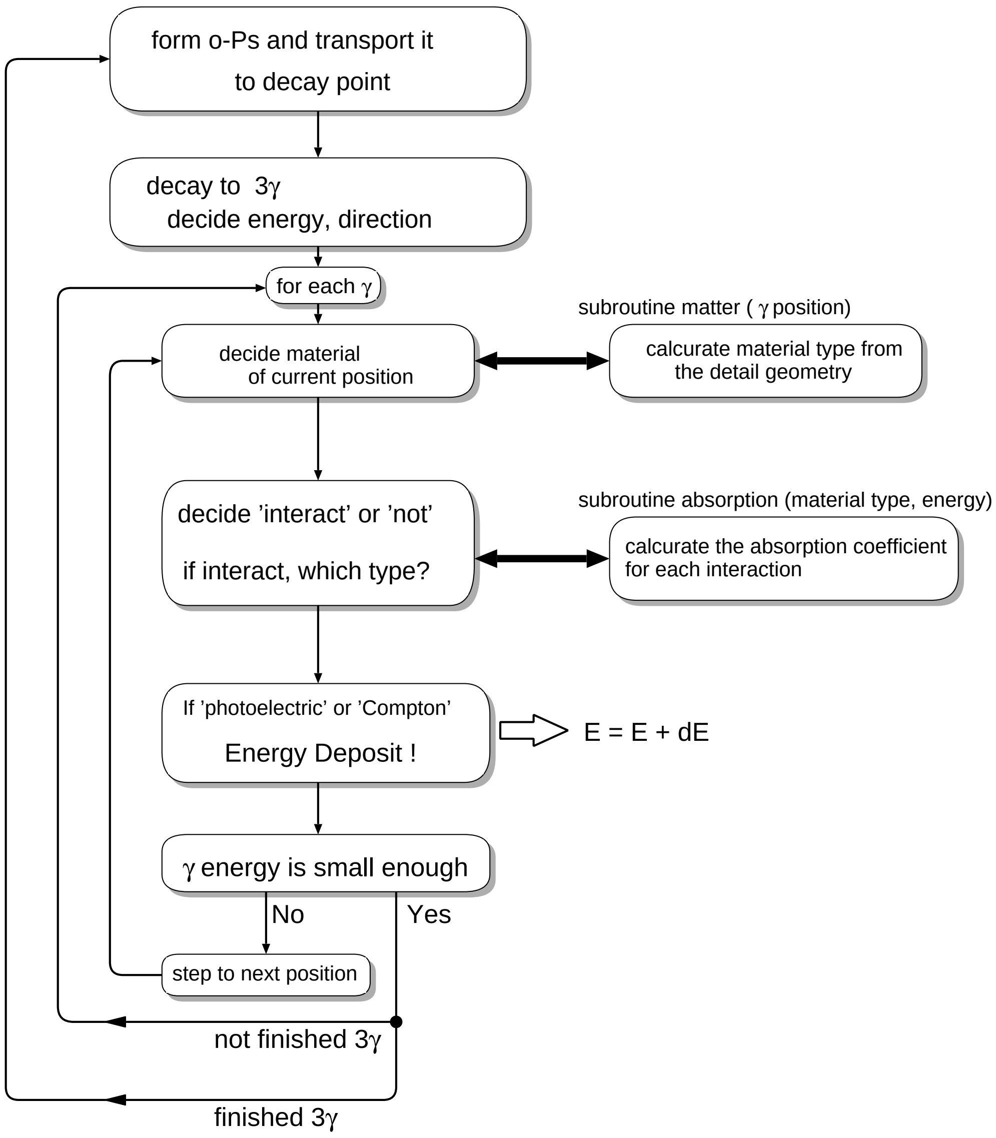

Figure 3.20: Flow chart of the logic for the Monte Carlo simulation.

Chapter 4

Analysis and Discussion

In this chapter, the observed time spectrum is fitted with the direct 2γ correction method. The calibrations, several cuts, and the correction mechanism are described in detail. The last section contains a detailed discussion of the systematic errors accompanying this measurement.

The explanations of various procedures are described for RUN I, whereas most of the parts are common to both RUNs. Several points where the two RUNs make differences will be stated on its point.

4.1 Calibration and Correction

4.1.1 Data sets

During the RUNs, data are taken with the CAMAC-Linux system (see, Sec. 3.2.7) through CAMAC data taking cycles. Only the valid events , i.e. valid β^+-signal with at least one valid data from the γ-detectors, are recorded. About 78% and 64% of the β^+ hit events are valid for RUN I and II, and stored in the disk storage after data suppression, which will be described in the following paragraphs. Totally about 2.7×10^9 β^+ and 2.0×10^9 β^+ events were recorded for RUN I and II respectively. The net data taking periods are about 6.1 month and 6.0 month for RUN I and RUN II. Typical β^+ rate for two RUNs are (regardless of their validity) *630Hz, 575Hz* for RUN I, and RUN II respectively.

The most of the valid events consist of the fast component called the prompt events which appears as a sharp peak at $t = 0$ in the time-spectrum. This peak consists of the 1274.6 keV nuclei-γ and the 511 keV $\gamma's$ emitted from a positron annihilation or p-Ps decay. For the decay rate measurement of o-Ps, this prompt events are indispensable since these events can be used for the time-zero calibration. Nevertheless the large fraction of them are useless. Therefore only the fraction 1/20 of prompt events of NaI(Tl) and Ge detectors, are stored in a disk storage; this operation is denoted as the prompt suppression in this thesis.

Typical count rate of the valid events before and after the prompt suppression are summarized in table 4.1 in regard to 10^5 counts of β^+ events. Data are storaged into multiple files for every 8.5×10^6 events. All the

	RUN I	RUN II
blind β^+ events	100 000	100 000
valid events	78 000	64 000
after suppression	27 000	22 000

Table 4.1: The data taking rate for RUN I, and RUN II.

manipulation of the data analysis, especially the calibration is carried out by utilizing these files as data units. Because it needs about half a day to take data for a one file unit, it is guaranteed that the data calibration is performed twice a day.

4.1.2 Recovery of Data

Off-line analysis starts from recovery of the data on the other machine. The data which have been compressed at the data dumping are recovered according to exactly the reverse way. The prompt events having been defined as those events that lie within certain TDC region is enhanced at the data recovery by a factor of 20. Note that the actual statistics of the prompt region is 1/20, the care needs to be taken when handling the ADC spectrum from the prompt region.

4.1.3 Calibration of Data set

The temperature of the experimental area was controlled to be stable within $\pm 0.5\ ^{\circ}C$ throughout the measurement. Consequently the electronics system works in stable. However the each measured spectrum of the ADCs and the TDCs can subtly shift in a long-range measurement due to the humidity variation or small change of the temperature.

In order to suppress the smearings due to the fluctuation of the measured quantity, the dairy calibration (twice a day) has been performed by using an each file unit. To reflect these multiple number of calibrations to the analysis part or a fitting procedure, the variable number of calibration values are written in the *parameter files*, being preserved on the same format during the RUNs.

There are three kinds of data for a dairy calibration.

for ADC spectrum of NaI(Tl) scintillators, and Ge detectors
It must be noted that the merit of using ^{22}Na as a positron source is a accompanying 1274.6 keV nuclei-γ. With the 511 keV positron

annihilation line, these two peaks can be the best pointer at an energy scale calibration for ADC both for NaI(Tl) and Ge. Each peaks are fitted with normal Gaussian function and the fitted values are recorded in the corresponding parameter file. Fitting is performed with the ADC spectrum from NaI 0 $\sim$ 3, and Ge 0, 1, for both wide, and narrow gate one, i.e. NAI-WD, NAI-NW, GE-WD and GE-NW (see Sec. 3.2.5, 3.2.5 for definition).

for TDC spectrum of NaI(Tl) scintillators Owing to its fast rise-time of the signal, TDC values of the NaI(Tl) can be directly used for T_0 determination. Nevertheless small energy dependence on timing splits the prompt peak into two peaks, i.e. 1274.6 keV from nuclei-γ's and 511 keV from an annihilations and p-Ps components. This time-walk correction is performed in Sec. 4.1.5 at the time spectrum filling. Since the time-walk is defined as a deviation of the discrimination timing from the 511 keV signal, T_0 needs to be determined from the 511 keV prompt peak. The time spectrum whose energies lie within $\pm$ 50 keV from 511 keV is used for the prompt peak fitting.

for TDC specturm of Ge detectors

For the Ge detectors, the things are getting rather complicated. In this case the TDC value itself cannot be directly used for T_0 fitting due to the slow rise-time feature of the Ge signal.

As already discussed in Sec. 3.2.6, the hit timing of the Ge detectors are obtained with RCPD method . The slow rise-time events are rejected according to a certain criterion, and the time spectrum is obtained using Eq. (3.11) where a factor α has been set at an optimal value (detail parameter value, etc. will be described in Sec. 4.1.4).

Same as in the NaI(Tl) case, the time-walk correction is performed by using 511 keV timing as a reference, thus the derivation of T_0 is carried out by fitting a time spectrum whose energy is around 511 keV.

for base ADC of NaI(Tl) scintillators, and Ge detectors

Generally the values of the base ADCs are centering at the base-line value, and present a normal Gaussian type structure around the center value; this uncertainty is mainly originated from the base-line fluctuation. Contrast to the ADC spectrum case, the absolute calibration is meaningless for the base ADC, because the degree of the fluctuation depends only on the devices and not on the physics. In addition, there is no useful marker as the two peaks in the ADC spectrum.

Therefore the mean value and standard deviation of fitted Gaussian are recorded. At the data cutting step, these values will be used for calculating the degree of deviation from the center value of base-line.

for ADC spectrum of β^+ energy and base line condition
The lower and the upper limit value of the selected region is fixed during the runs. The values are confirmed for each file unit with the distributions.

The contents of the parameter files are summarized in table 4.2. All param-

detector type	data type	values	
NaI $0 \sim 3(0)$ for RUN I (II)	for Wide ADC	511.0 keV	1274.6 keV
	for Narrow ADC	511.0 keV	1274.6 keV
	for Base ADC	peak	standard deviation
	KEK TDC	T_0	
Ge $0 \sim 1$	for Wide ADC	511.0 keV	1274.6 keV
	for Narrow ADC	511.0 keV	1274.6 keV
	for Base ADC	peak	standard deviation
	KEK TDC	T_0	
β^+	β^+ energy	Lower	Upper
	β^+ base	Lower	Upper

Table 4.2: The contents of the each parameter file.

eter files are written in this format.

4.1.4 SRT Cut and Determination of RCPD factor

As described in Sec. 3.2.6, slow rise-time components of the Ge signal can be rejected with RCPD method. If one defines the time intervals between the plural discriminator level as, $\delta T_1 = T_{100mV} - T_{50mV}$ and $\delta T_2 = T_{150mV} - T_{50mV}$, then the actual cutting conditions can be expressed as follows,
for Ge 0,

$$\begin{aligned} \delta T_2 &> 1.6 \times \delta T_1 + 3.0 \ , \\ \delta T_2 &< 2.5 \times \delta T_1 + 8.0 \ , \\ \delta T_1 &< 40.0, \ \ \delta T_2 < 85.0 \ , \end{aligned} \tag{4.1}$$

for Ge 1,

$$\begin{aligned} \delta T_2 &> 1.6 \times \delta T_1 - 5.0 \ , \\ \delta T_2 &< 2.5 \times \delta T_1 - 4.0 \ , \\ \delta T_1 &< 45.0, \ \ \delta T_2 < 85.0 \ . \end{aligned} \tag{4.2}$$

These cuts can be verified in Fig. 4.1. As can be expected from the fact that the three discriminator levels are equally separated, slope of the distribution is 2.0 which can be confirmed in the figure, although each figure has the

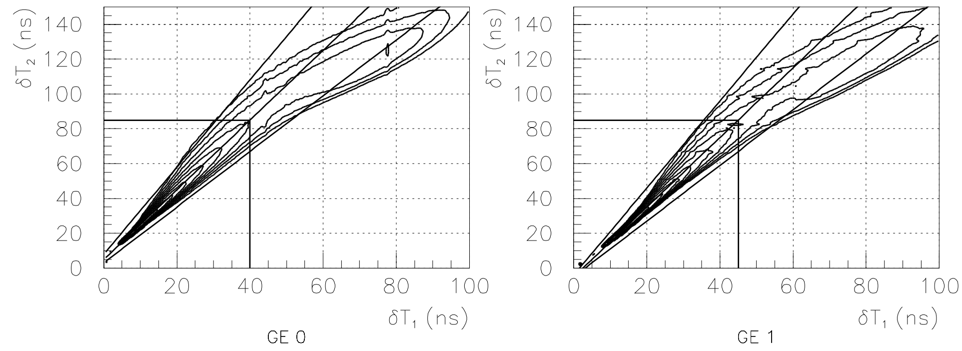

Figure 4.1: Contour plot of the two time intervals δT_2 and δT_1 for RUN I. The diagonal line indicates the exact slope of 2.0 penetrating the ridge of distribution. Two lines on sides are pointing out the fan-shape cut boundary which is mentioned in context as Eq. 4.1 and 4.2. The vertical and horizontal lines shows the cut boundary for the SRT events.

different pedestals which has been stemmed from the different off-set on each TDC channel.

The actual distributions are spreading in a fan-shape as a result of the signal-rise fluctuation. Thus as a cut condition, one should employ a fan-shape cut though it requires rather complicated correction functions consist of δT_2 and δT_1 values. The equation (3.11) is modified as,

$$T_{intrinsic} = T_{50mV} - \alpha \times \delta T, \quad \delta T = \frac{1}{2}\left(\delta T_1 + \frac{1}{2}\left(\delta T_2 - a\right)\right), \tag{4.3}$$

where a is a off-set value of δT_2 in Fig. 4.1. The time intervals δT_2, δT_1 are averaged and replaced with the simple δT_1 value in Eq. (3.11). Since the signal-rise time property is not charged at all from RUN I to RUN II, the same cutting condition can be applied for the RUN II case as well. From Fig. 4.2 this can be clearly confirmed.

The RCPD factor in Eq. (4.3) is determined by minimizing the timing resolution while retaining the shape of time-response function e.g. symmetry. The time responses of the germanium detectors are checked by using the prompt peak (see Sec. 4.1.1 for definition of prompt peak). Since the prompt peak events are occurring at a time zero, they are supposed to make a symmetric Gaussian distribution as to the time. The prompt peak is fitted by an asymmetric Gaussian function which is defined as,

$$F_{agauss}(t) \quad = \quad \frac{A}{\sqrt{2\pi}(\sigma_+ + \sigma_-)} \exp\left(-\frac{1}{2}\left((x-\mu)/\sigma_+\right)^2\right) \quad (\text{for } x \ \geq \ \mu)$$

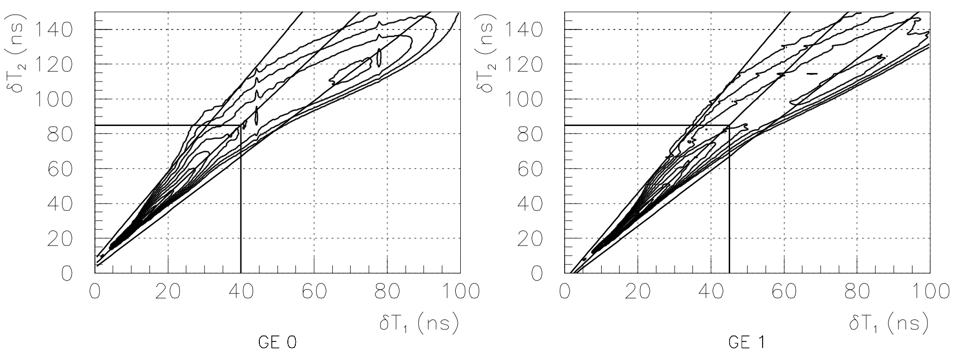

Figure 4.2: Contour plot of the two time intervals δT_2 and δT_1 for RUN II. The same cutting conditions as in RUN I are applied. Description of the figure is found in the caption of Fig. 4.1.

$$= \frac{A}{\sqrt{2\pi}(\sigma_+ + \sigma_-)} \exp\left(-\frac{1}{2}\left((x-\mu)/\sigma_-\right)^2\right) \quad (\text{for } x < \mu), \tag{4.4}$$

where σ_+ and σ_- are the standard deviation of the right and the left side of the peak respectively. The best value of the RCPD factor, α is searched for by scanning the value from 1.0 to 2.2. The value called *Asymmetry* and *mean sigma* are defined as,

$$\begin{aligned} \text{Asymmetry} &= \sigma_+ - \sigma_-, \\ \text{mean sigma} &= \sqrt{(\sigma_+^2 + \sigma_-^2)/2}. \end{aligned} \tag{4.5}$$

Figure 4.3 shows these values as a function of factor α. For Ge 0, the minimum point of the mean sigma is around $\alpha = 1.6 - 2.0$, whereas the asymmetry rapidly collapses over 1.8. Therefore one can determine the optimized α value to be 1.7. In the same way, the optimized value for Ge 1 is settled to be 1.5.

4.1.5 Time walk Correction

Because the detection timings of the signals are depending on their energies, which are termed as the time walk, this lag of time must be corrected in order to obtain the intrinsic decay timing.

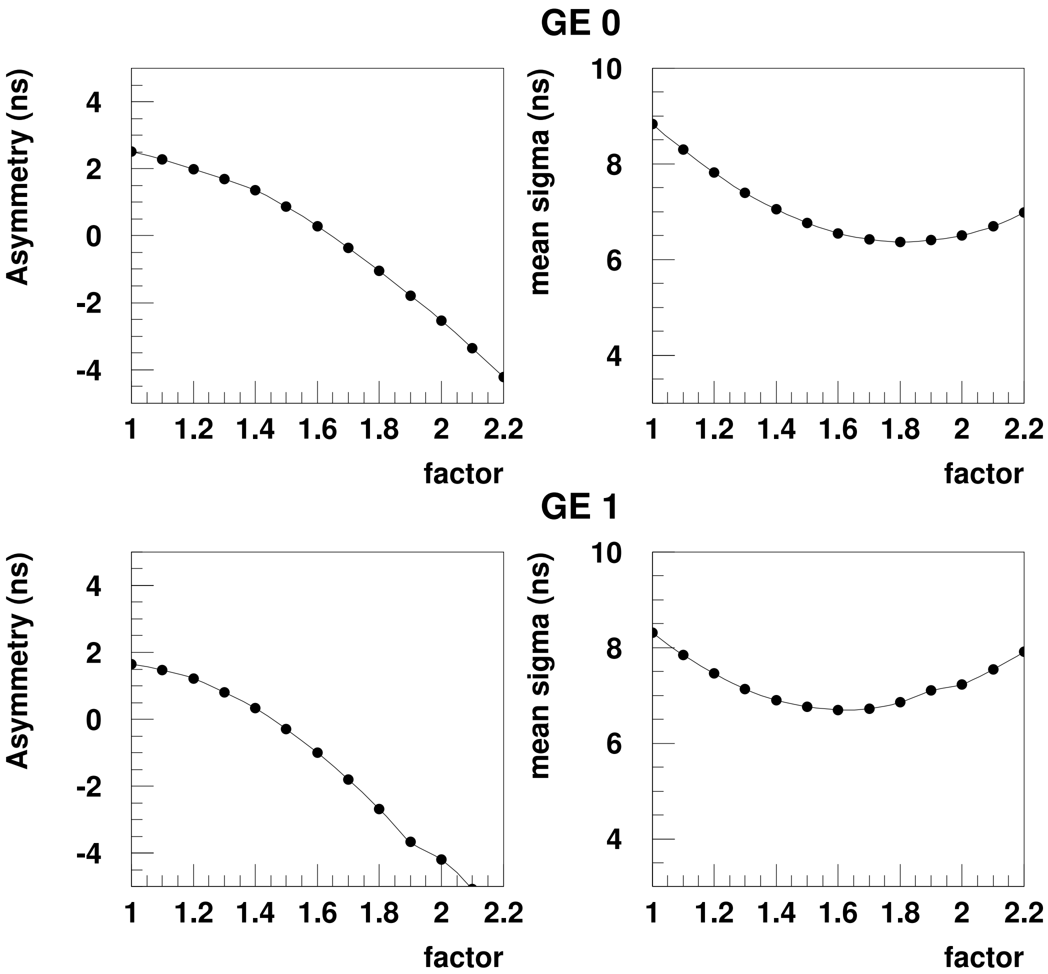

Figure 4.3: The asymmetry and the mean sigma of the Ge timing response functions. The definition of these quantities are found in the context. The asymmetry and the mean sigma of the prompt peak for each Ge detector are plotted as a function of the RCPD factor α.

Time walk correction for NaI(Tl) scintillators

To know the relation between the time walk and the energy, the prompt peak can be again made use of from the fact that its absolute time must equal to zero. The pulse height of the low energy γ signal is relatively small and resulting to a later detection timing as a consequence of the leading edge discrimination. Figure 4.4(a) shows this relation for the NaI 0; it can be expressed with a simple polynomial function of the energy.

The prompt peak is divided into 14 energy windows by 100 keV step each, and filled into 14 histograms. Each histogram is fitted by normal Gaussian in order to obtain the peak time. Typical energy for each energy window is determined by a mean value weighted with event numbers. Since the calibration of T_0 is performed for the 511 keV annihilation line (see Sec. 4.1.3), the time walk is defined as a time deviation from the reference energy 511 keV. 14 data set (mean time, mean energy) weighted with the event number inside the window, are fitted with a five-degree polynomial of $\log E$ (E: energy of γ). This fitted function $f(E)$ is used at the time spectrum filling, i.e. f(NaI(Tl) energy in keV) $-$ f(511.0 keV). After correction, one can obtain the energy independent timing as in Fig. 4.4(b). Inasmuch as the time spectrum of the NaI(Tl) is formed with the energy selected events of 370–440 keV, the time walk affects little on the final result of the decay rate.

Time walk correction for Ge detectors

Although the RCPD method compensates the time differences between the various pulse heights, there still remains the timing dependencies on the energy of the incident γ-ray. This time walk can be corrected with the same manner as in the NaI(Tl) case. That is, the 14-points of time deviations from the reference energy, 511 keV are fitted with a five-degree polynominal of $\log E$. The relative deviation from 511.0 keV, i.e. f(Ge energy in keV) $-$ f(511.0 keV) is subtracted from TDC value at time spectrum filling. After the correction, time walk effects of the Ge detectors as in Fig. 4.5(a), (c) are modified to be (b), (d) for Ge0 and Ge1 case respectively,

Time walk correction for the trigger PMT

Due to its fast rise time property of the signal, the time walk of the trigger side (plastic scintillator) is small. In order to extract the time walk effect from the trigger, one needs a fixed TDC stop signal, e.g. the energy limited NaI(Tl) scintillator signals for the prompt peak events. In Fig. 4.6(a) selected NaI(Tl) events whose energies being within 1274.6 ± 50.0 keV are plotted against the β^+ energy which is expressed in ADC channel. As contrasted with the γ-ray detectors, the lower the energy becomes the faster

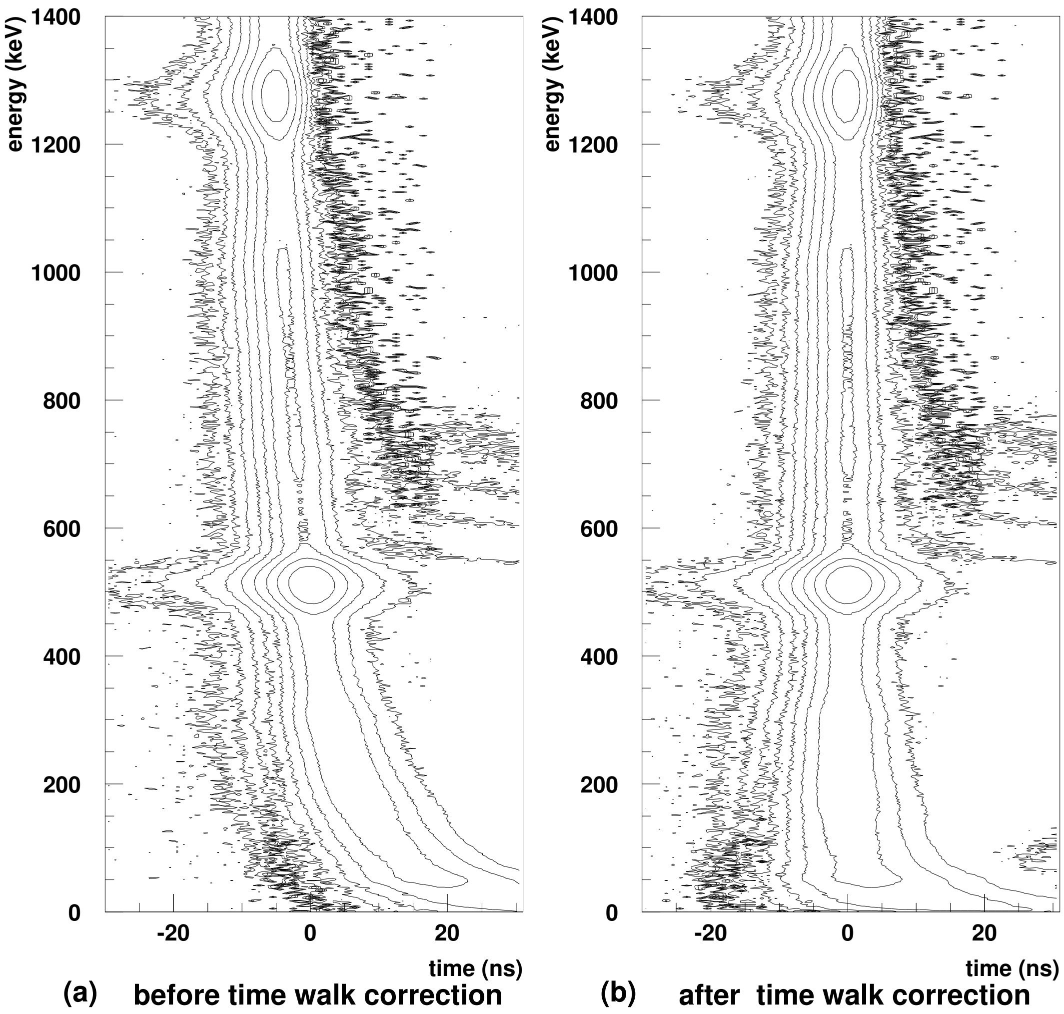

Figure 4.4: Contour plot of the prompt timing of NaI(Tl) scintillator versus its energy, before (a) and after (b) the time walk correction. The altitude are expressed in logarithm form.

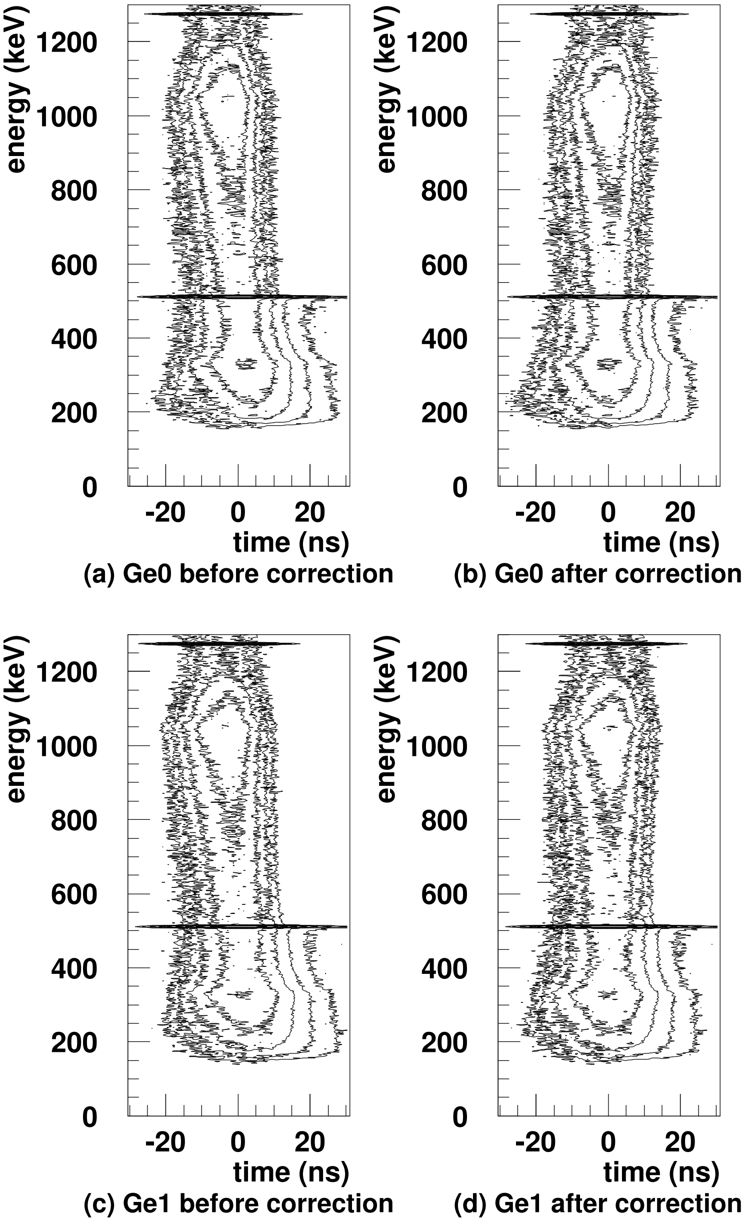

Figure 4.5: Contour plot of the prompt timing of Ge detectors versus its energy, before (a)(c) and after (b)(d) the time walk correction, for Ge0, and Ge1 respectively. The altitude are expressed in logarithm form, and the asymmetry of the distribution beneath the energy of 511 keV shows the contribution from the o-Ps 3γ decay.

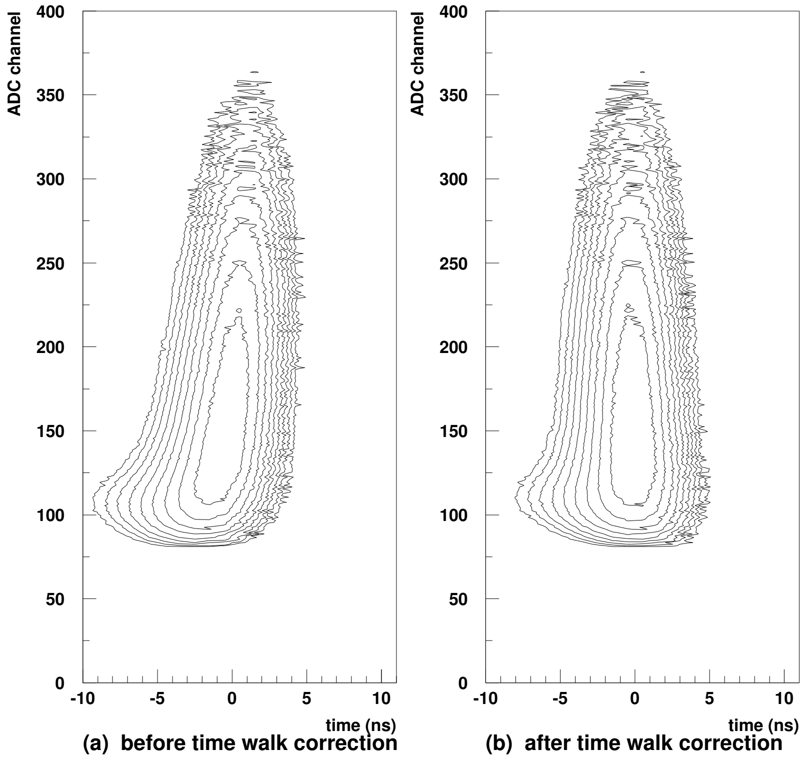

Figure 4.6: Contour plot of the time walk of trigger PMT versus the ADC channel for β^+ energy, before (a) and after (b) the time walk correction. The altitude are expressed in logarithm form. Notice the time walk effect is observed in the opposite direction compared with NaI(Tl) scintillators or Ge detectors, due to the fact the trigger PMT starts the TDC instead of stopping.

the timing of prompt becomes, due to the fact that the trigger PMT plays a role of starting the TDC instead of stopping.

As in the same manner with the NaI(Tl) and Ge cases, the selected prompt events are divided into 7 energy windows. The relation of fitted peak times of each energy window, and the typical ADC channels calculated from the weighted mean values are then determined by two dimensional fitting with a function of,

$$\mathrm{ADC(ch)} = P_0 + P_1 \cdot \log(\mathrm{time} - P_3) + P_2 \cdot (\log(\mathrm{time} - P_3))^2, \tag{4.6}$$

where $P_0 \sim P_3$ are fitting parameters. Because the absolute energy scale of β^+ is not clear, the reference β^+ energy value for absolute time zero, is determined to be the weighted mean of the ADC channel. Figure 4.6(b) represents the relation between the prompt timing of the energy selected events and the β^+ energy after the time walk correction.

4.2 Determination of the ratio $\lambda_{pick}(t)/\lambda_{3\gamma}$

In this section, the ratio $\lambda_{pick}(t)/\lambda_{3\gamma}$ is determined as a function of time using the energy spectrum precisely measured by the Ge detectors. Firstly, the typical time window ($t = 150\ ns - 700\ ns$) is used for the explanation of the procedure. Later the procedure will be applied for multiple time windows, yielding the time dependencies of the ratio $\lambda_{pick}(t)/\lambda_{3\gamma}$.

4.2.1 Energy spectrum of Ge detectors

The energy information of Ge detectors (GE WD) are measured with the ADC whose dynamic range is 12-*bit* (4096 *ch*). If one uses the ADC with its full range and covers the 1274.6 keV-γ at around 4000 *ch*, the intrinsic energy information par 1 ch (1 bin) of the ADC is about 0.3 keV. In order to maintain this ADC resolution, the bin width of histogram for the energy spectrum is determined to be 0.33 keV (1/3 keV).

As a event selection, the germanium data whose base conditions lie within the range, $-4 < \mathrm{BASE}(\sigma) < +4$, and their (wide-narrow) values lie within ± 40 keV are selected.

The energy spectrum is obtained by the re-binning operation; by assuming the good linearity of the ADC system, the ADC values are transferred into new histogram using following equation,

$$\text{Energy of Ge} = (1274.6 - 511.0) \cdot \frac{[\mathrm{GE\ WD}] + Random - C_{511}}{C_{1275} - C_{511}} + 511.0, \tag{4.7}$$

where *Random* is a uniform random number generated ranging from 0 to 1, C_{511} and C_{1275} are the calibration constant representing the ADC channel for 511 keV and 1274.6keV respectively which have been obtained at Sec. 4.1.3.

In the energy range of 511 keV±15 keV, *Random* number is weighted with the Gaussian distribution because the variation of the spectrum within the one bin-width cannot be no longer negligible around 511 keV. Figure 4.7 shows the energy spectrum of a prompt peak at the energy of 511 keV and 1274.6 keV, which enter the time range of $t = -10\ ns \sim 10\ ns$. The shown figures are for RUN I. These two peaks can be used to check the energy calibration and the re-binning operation as well. It is well known as in the references [70, 71] that these single peaks observed by Ge detectors obey the analytical function which consists of Gaussian function, a lower exponential function, a higher exponential function, and a step function. In practice, the peaks are fitted with following rather simplified function,

$$f(E) = a_2 \left(\frac{1}{\sqrt{2\pi} a_3} \exp(-y^2/2a_3^2) + \frac{a_4 \exp(a_5\ y)}{(1+\exp(a_6\ y))^4} \right), \tag{4.8}$$

where y is defined as $y = (E - a_1)$. The function is expressed with six parameters, the peak centroid a_1, peak strength a_2, the Gaussian width a_3, and the tail property $a_4 \sim a_6$.

The Gaussian part can be simply attributed to the white noise of the detector. However the momentum distribution of the 511 keV annihilation line is broader than the intrinsic Ge detector's resolution, because the Doppler broadening due to the electron motion inside the target atoms is wide. This Doppler broadening is known to approximately obey the Gaussian distribution in SiO_2 powder.

On the other hand, the exponential tail component in the function is attributed to the incomplete collection of ionized charge and to the electron escapes from the active region of the detectors.

From Fig. 4.7, it is obvious that the assumption of the fitting function above works well, and that the energy calibration and the re-binning operation are correctly performed. The value of the centroid and the Gaussian width are summarized in Table. 4.3.

detector	energy	centroid a_1 (keV)	Gaussian width a_3 (keV)
Ge0	511.0 keV	510.999 ± 0.004	1.01771 ± 0.0003
Ge0	1274.6 keV	1274.47 ± 0.0007	0.7753 ± 0.0008
Ge1	511.0 keV	511.002 ± 0.005	1.07278 ± 0.0004
Ge1	1274.6 keV	1274.49 ± 0.007	0.7920 ± 0.0003

Table 4.3: The basic profile of the Ge detector's energy spectrum.

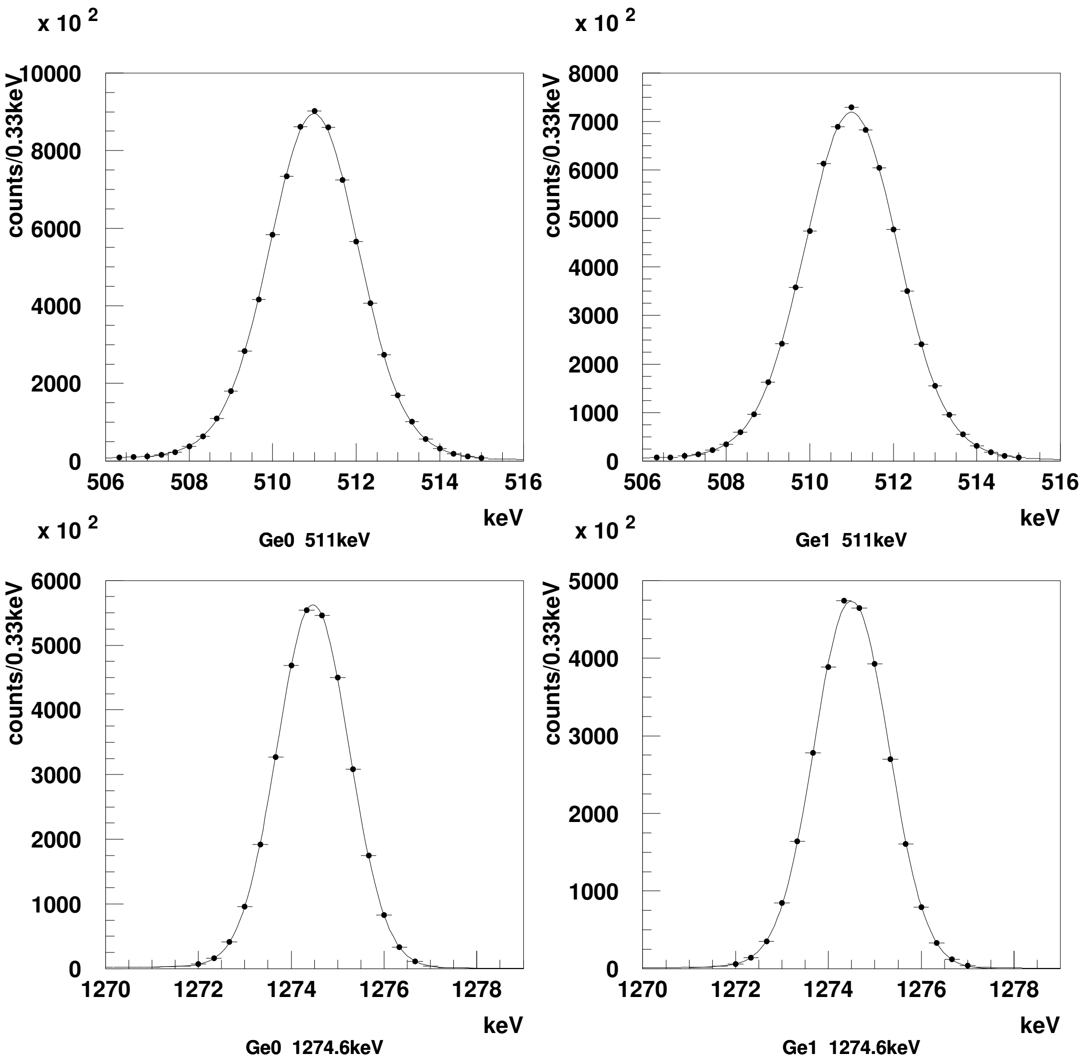

Figure 4.7: The energy spectrum of the prompt peaks measured by Ge detectors. The events from $-10ns$ to $10ns$ time range are sliced out. Note that in spite of the prompt time region, the multiplication of data suppression factor 20 to the event number is not performed in order to ensure the statistical consistency for the error bars (See Sec. 4.1.2).

4.2.2 Time spectrum of Ge detectors

The γ-rays are classified into following event groups according to their signal timing. The typical time windows used firstly in this analysis is defined as well.

Prompt peak - As already defined, a sharp peak at $t = 0$ as is shown in Fig. 4.8 is referred to as *the prompt peak*. The peak is consists of the 1274.6 keV nuclei-γ and the 511.0 keV γ's emitted from a positron annihilation (a positron does not form the Ps and annihilate with an electron), and the p-Ps decay (whose life time is about 125 *ps*, being regarded here as a time zero). A good time resolution of $\sigma =$ 4.2(4.8) ns for Ge 0(1) at 1274.6 keV nuclei-γ prompt peak, and $\sigma =$ 5.2(5.9) ns for Ge 0(1) at 511 keV prompt peak.

o-Ps decay events - Following the prompt peak, an exponential decay curve due to the o-Ps decay can be found in Fig. 4.8. These decay events consist of photons whose energies are under 511 keV because the energy distribution of the o-Ps 3-body γ decay is continuum.

The time window defined as "Delayed" ranges from 150 ns to 700 ns as in Fig. 4.8. The events within this window are used for a typical window in explaining of the procedure.

Accidental events - The accidental hits whose β^+-start does not corresponding to the γ-stop signal forms a flat spectrum after the o-Ps decay curve. In order to estimate a contribution from the accidental hit, the time window of $t = 2000\ ns - 3600\ ns$ is sliced out, and referred to as "Accidental" from now on.

4.2.3 Extraction of o-Ps Energy Spectrum

In this section, the typical windows defined above are used to extract the o-Ps energy spectrum for the first step.

Figure 4.9 shows the energy spectrum of the Delayed and Accidental windows. Spectrum of the Accidental window is normalized in order to compensate the difference of window width, i.e. multiplied by 550/1600. No correction on R_{stop} factor (see Eq. (3.9)) has been done for the Ge time spectrum, as the average stop rate for Ge detectors are about 200Hz, which can contribute to the final result by less than 2 *ppm*.

The Accidental events mainly consist of the same contents as in the prompt events, thus the source of contents within the energy region (300–520 keV) now being of interest are the 511 keV annihilation line, and the Compton scattered events from the 511 keV or the 1274.6 keV-γ's.

Energy spectrum of o-Ps decay is obtained by subtracting the Accidental energy spectrum from the Delayed energy spectrum. From now on, this

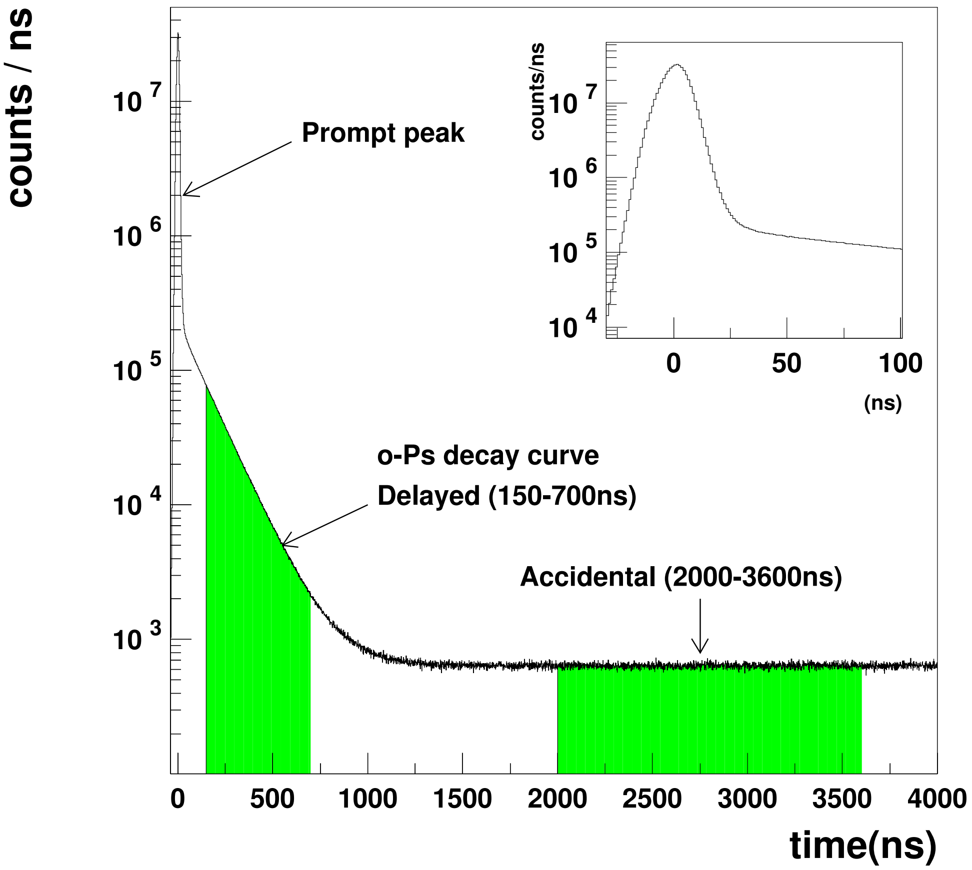

Figure 4.8: The time spectrum distribution of Ge0+Ge1 for RUN I. Events inside the energy window of 300–520 keV are extracted. A sub-figure in the upper right corner shows the enlarged view of the prompt peak. It takes about 40 *ns* to completely eliminate the effect from the prompt peak.

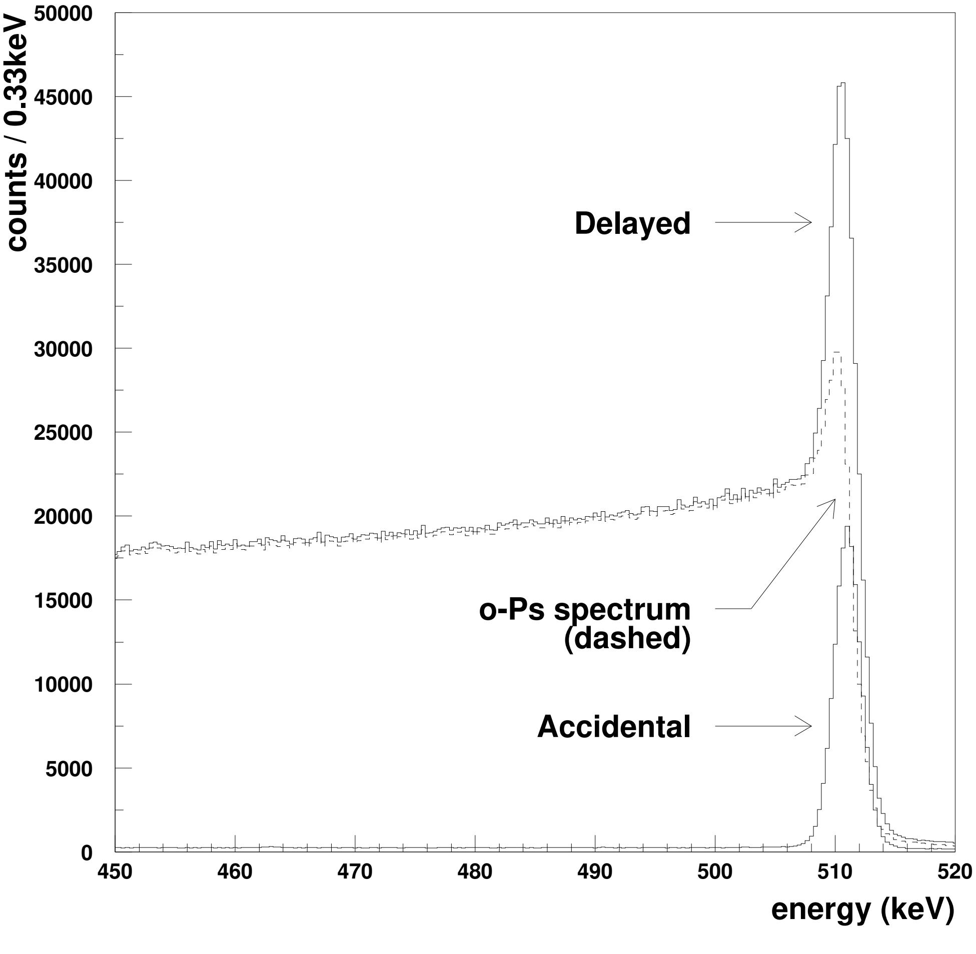

Figure 4.9: The energy spectrum of Delayed and Accidental time windows for RUN I. Accidental events are normalized as to compensate the different time window widths. Dashed line represents the o-Ps spectrum; the residual of a subtraction between two spectra.

energy spectrum is denoted as "o-Ps spectrum", and is plotted in Fig. 4.9 with a dashed line. The pick-off annihilation peak at 511 keV is clearly evident at the edge of the 3γ-decay continuous spectrum.

On the other hand, the energy spectrum containing 3γ-decay continuum alone is calculated by the Monte Carlo simulation. For the purpose of reproducing the real data whose spectrum being deformed by the SRT (slow rise-time) cut, the Monte Carlo spectrum is modified by multiplying the energy dependent efficiency curve obtained at Sec. 4.2.4. Obtained energy spectrum of 3γ-decay, being referred to as "3γ-spectrum" from now on, is normalized with the observed o-Ps spectrum at the region 480-505 keV.

This narrow region just below the tail of 511 keV-peak is used to normalize the Monte Carlo distribution with the data spectrum according to the following reasons.

- Compton scattered events originated from the pick-off events can be reduced. Only 2.3% of the Compton scatted 511 keV events can enter this region.

- The detection efficiency which has been already implemented in the Monte Carlo (see Sec. 3.2.4), and the efficiency of slow rise-time cutting have some dependence on the energy of the incident γ -ray. This dependences can be reduced by adopting the narrow region aside from the 511 keV peak.

- Relative change of the 3γ spectrum caused by the $O(\alpha)$-correction does not exceed 0.3% as indicated in Fig. 2.1.

4.2.4 Assessment of the SRT cut Efficiency

Although our RCPD method described in Sec. 3.2.6 can accept any energy γ-ray signal and there would seem to exist no cutting efficiency depending on the energy, it actually depends on the energy of the Ge detectors due to the SRT cut. To estimate the cutting efficiency, the four types of energy spectra are prepared,

1. The energy spectrum observed in time region (500 - 1000 ns) with the SRT cut condition.

2. The energy spectrum observed in time region (500 - 1000 ns) without the SRT cut condition.

3. The energy spectrum of the accidental time (2000 - 3600 ns) with the SRT cut condition.

4. The energy spectrum of the accidental time (2000 - 3600 ns) without the SRT cut condition.

The normalized accidental spectra are subtracted from the corresponding o-Ps decay spectra. This yields the energy spectra of the pure o-Ps decay with and without the SRT cut respectively. The efficiency curves are obtained simply by dividing the one spectrum (SRT on) with the other (SRT off).

It should be noted that the Compton scattered γ events are tend to be highly rejected rather than the photoelectric events. Because they apt to extend over the Ge detectors and result into the SRT events; heterogeneous high-voltage region generates the SRT pulses. Therefore the Compton scattered events, especially originated from the prompt peaks, easily spoil the precisely determined efficiency curve. In order to avoid this, the spectra are sliced out from the selected time range.

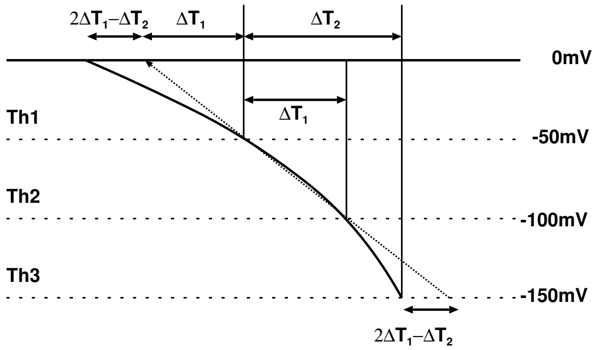

Figure 4.10: Schematic figure illustrating how to extract the intrinsic signal timing for the SRT events. The procedure for the normal events is already illustrated in Fig. 3.15

Unfortunately the other problem arises from the fact that the RCPD method described in Sec. 3.2.6 is no longer valid for the SRT events. As seen in Fig. 4.1, the relation between δT_1 and δT_2 is no longer subjected to a constant slope rule. Instead, the intrinsic decay time must be hastened as illustrated in Fig. 4.10, where δT in Eq. (4.3) is replaced by,

$$\delta T = 3 \times \delta T_1 - \delta T_2, \tag{4.9}$$

applied for the events that satisfy the condition $\delta T_1 > 50(55)\ ns$ for Ge 0(1). Figure 4.11 shows the effectiveness of the new approach. If one applies the normal-RCPD method to all signal including the SRT events, then one obtains the avalanche of the Prompt peak around $t = 100\ ns$ as the solid-line in the figure. This indicates that the normal-RCPD method tends to underestimate the δT for the SRT events. On the other hand, the new approach well suppresses the avalanche as can be seen in the figure with the dashed-line. The improvement can be confirmed by comparing with the dotted-line which stands for the time spectrum with the SRT cut. However

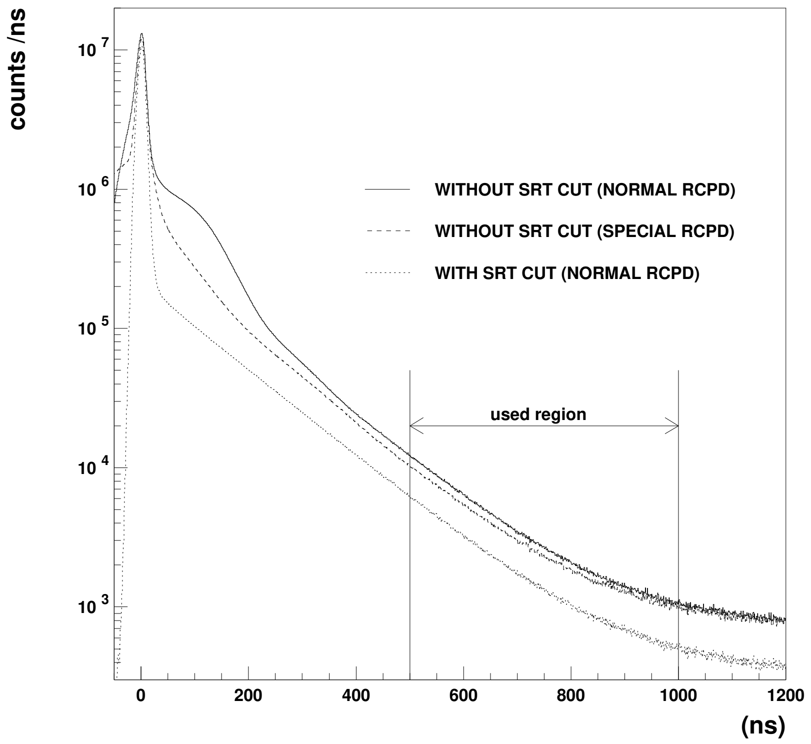

Figure 4.11: Result of the SRT cut. (solid) The line shows the time spectrum without the SRT cut. The normal-RCPD method is applied to all the signal including the SRT events. (dashed) The line shows the time spectrum without the SRT cut; this time the different way of correction is performed for SRT events as in Fig. 4.10. (dotted) The line shows the time spectrum with the SRT cut; intrinsic timing is extracted with the normal RCPD-method.

since the exclusion of the prompt events cannot be perfectly performed, the later timing events such as $500 - 1000$ ns are used in practice.

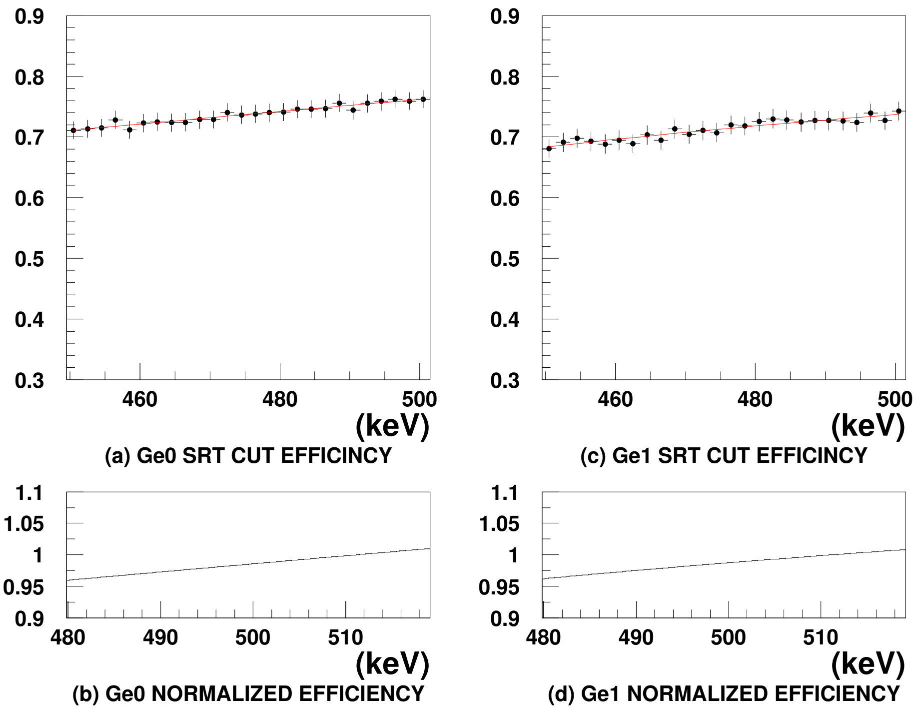

Figure 4.12: The cut efficiency for the SRT.
(a) (c) Data points are obtained for Ge0 and Ge1 with the procedures described in context. Solid line shows the result of fit; fit is carried out within the range $450 - 500$ keV.
(b) (d) Fitted curve is normalized by a factor such that the value at 511 keV equals to 1.

Figure 4.12 (a) and (c) show the obtained efficiency curves for the Ge 0 and Ge 1 respectively, where the fitting is performed in order to obtain the efficiency curves as a function form; the fit is performed using the range 450–500 keV which is now in interest. The region over 500 keV is excluded to avoid the irregular behavior around the pick-off spectrum. The normalized curves with respect to the values at the 511 keV points are drawn in

Fig. 4.12 (b) and (d). The spectrum from the Monte Carlo simulation is multiplied with these efficiencies; this yields the 3γ-spectrum which reproduce the actual measurement.

4.2.5 Extraction of the Pick-Off Spectrum

As shown in Fig. 4.13 and in Fig. 4.14, the 3γ-spectrum from Monte Carlo calculation and the observed o-Ps spectrum indicate good agreement below 508 keV. The shape of the 3γ-spectrum is nearly independent of Monte Carlo simulation details in that the sharp drop-off at 511 keV is solely due to the phase-space cutoff. It is almost entirely determined by the energy response function of the Ge detectors.

It should also be noted that the lead sheets with 2.0-mm thick being placed in front of the Ge detectors well suppress the contribution from events where two low-energy γ's emmitted from a 3γ-decay simultaneously hit the one Ge detector.

Figure 4.15 and 4.16 show an enlarged view of the observed o-Ps spectrum after subtracting the 3γ-spectrum for RUN I and II respectively. The histograms from two Ge detectors are summed up. The resultant peak spectrum can be fitted with the function Eq. 4.8, since the shape of the peak must be same with that of the prompt peak if it really originates from the pick-off annihilation. The result of the fit parameters are summarized in table 4.4 for two RUNs. From the size of 1 σ width and position of the cen-

RUN #	centroid a_1 (keV)	Gaussian width a_3 (keV)	χ^2/d.o.f.
RUN I	$510.997^{+0.030}_{-0.024}$	1.142 ± 0.011	$50.5/(25-3)$
RUN II	$510.995^{+0.079}_{-0.059}$	1.024 ± 0.0065	$52.2/(19-3)$

Table 4.4: The profile of the resultant peak spectrum for two runs.

troid, one can undoubtedly conclude that this peak is purely originated from the pick-off events. Therefore this peak will be referred to as the **pick-off spectrum** from now on.

In order to estimate the validity of the present subtraction, i.e. the assessment of the systematic errors arising from this operation and SRT cut efficiency will be discussed in Sec. 4.4.

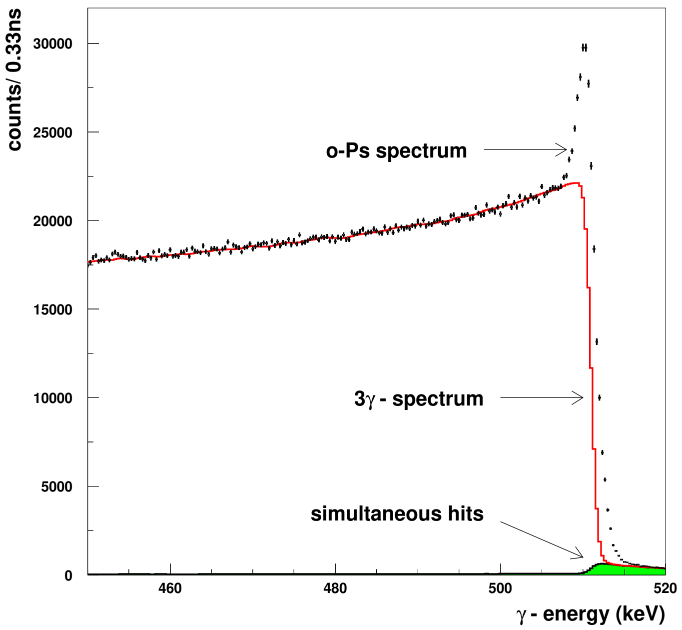

Figure 4.13: The energy spectrum of γ-ray from the measurement for RUN I (o-Ps spectrum: plotted points with error bars) and from the Monte Carlo simulation (3γ-spectrum: drawn with histogram). The spectrum of Monte Carlo simulation is normalized to the data by a number of events within the energy region of $480-505$ keV. Contribution from the simultaneous hits where two low-energy γ's hit the one Ge detector, are plotted as a shade area in the lower right corner.

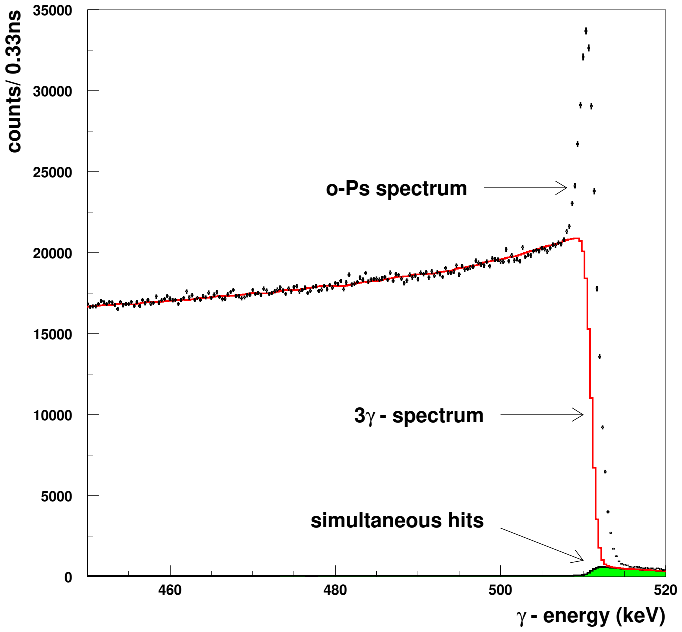

Figure 4.14: The energy spectrum of γ-ray from the measurement for RUN II.

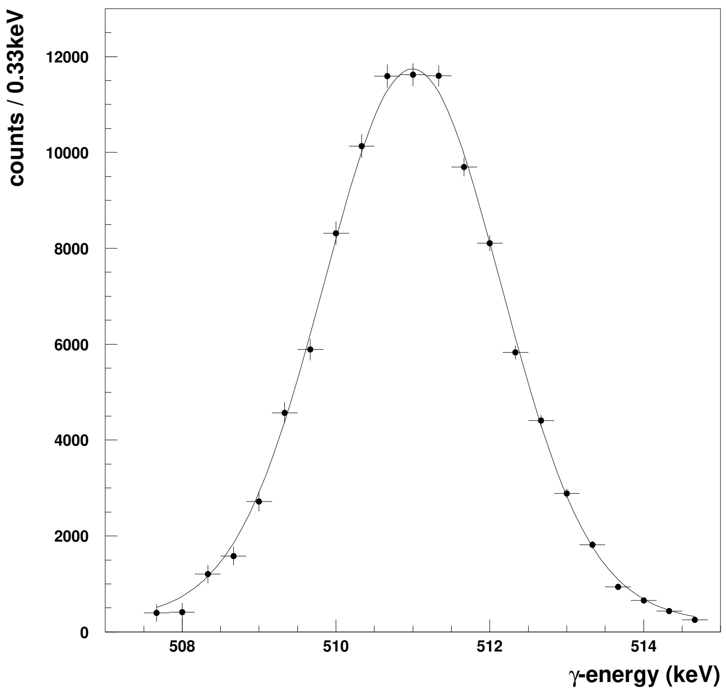

Figure 4.15: The pick-off spectrum at time range 150–700 ns for RUN I.

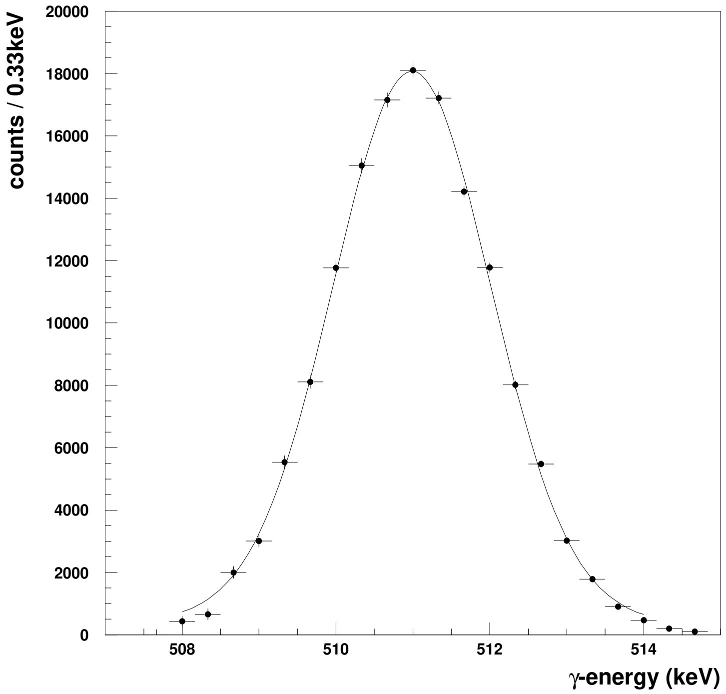

Figure 4.16: The pick-off spectrum at time range 150–700 ns for RUN II.

4.2.6 Introduction of the Counting Method

The ratio $\lambda_{pick}/\lambda_{3\gamma}$ can be calculated simply by counting the event number of the o-Ps spectrum and the pick-off spectrum. The reliable spectrum range of the o-Ps spectrum is restricted over the 450 keV from the following reasons.

- the SRT cutting efficiency is estimated within the range of $450-500$ keV. The range below the 450 keV is not reliable.
- Number of Compton scattering events increase relatively in the low energy range.

Therefore the part of the spectrum (480-505 keV) is used for the estimation. This **counting method** is performed with following procedures,

At first, let us describe the equation that relates the number of events with the ratio $\lambda_{pick}/\lambda_{3\gamma}$, that is,

$$\frac{\lambda_{pick}}{\lambda_{3\gamma}} = \frac{n_{pick}}{n_{3\gamma}} \cdot \mathcal{F}, \tag{4.10}$$

where conversion factor $\mathcal{F}$ is defined as,

$$\mathcal{F} = \frac{\sum_{i=1,2,3} \int_{480\text{ keV}}^{505\text{ keV}} P(E_i)\cdot\varepsilon(E_i)\; dE_i}{2\cdot\varepsilon\,(511\text{ keV})}. \tag{4.11}$$

One can interpret that the intrinsic decay constants λ_{pick}, $\lambda_{3\gamma}$ can be transfered into observed counts with this efficiency factor. In Eq. (4.11), $P(E_i)\; dE_i$ is the probability that i-th γ-ray from a 3γ-decay has energy of $E_i \sim E_i+dE_i$. This probability is known as a spectrum form up to the $O(\alpha)$-correction as in Fig. 2.2. Thus the probability $P(E_i)$ has dependencies neither on the measurement nor the Monte Carlo simulation. On the other hand, a ratio of the relative efficiencies of the Ge detector, $\varepsilon(E_i)/\varepsilon(511\text{ keV})$ can be calculated with the Monte Carlo simulation; the agreement between the observed data and the Monte Carlo can be confirmed as in Fig. 3.6. The specific value for $\mathcal{F}$ factor is 1.464×10^{-1} for both RUNs.

As the conversion factor $\mathcal{F}$ is defined as above, the observed count n_{pick}, $n_{3\gamma}$ is calculated as follows,

- n_{pick} is a sum of the events within the energy range $507-515$ keV of the pick-off spectrum.
- $n_{3\gamma}$ is a sum of the events within the energy range $480-505$ keV of the o-Ps spectrum.

Since the relative efficiencies, i.e. ε's, stand for the efficiency of the photopeak effect, the following background events must be subtracted from $n_{3\gamma}$ to obtain the pure $n_{3\gamma}$.

- Compton scattered event of the pick-off annihilation γ deposits energy on $480 - 505$ keV range.
- Compton scattered event of the 3γ-decay deposits energy on $480 - 505$ keV range.
- Two low-energy γ's from the 3γ-decay simultaneously hit the same Ge detector.

Then the pure $n_{3\gamma}$ can be expressed as,

$$n_{3\gamma}(\text{pure}) = n_{3\gamma} - f_a \times n_{pick} - f_b \times n_{3\gamma} - f_c \times n_{3\gamma}, \tag{4.12}$$

where $n_{3\gamma}$'s in the right hand of equation stand for the observed $n_{3\gamma}$.

These background factors are estimated with the Monte Carlo simulation. As to the events above the Compton edge, the uncertainty of the Monte Carlo is estimated and known to be within $\pm$ 5% level as in Appendix B.1.1. These correction factors are summarized in Table 4.5.

Type of Background	coefficient	for RUN I	for RUN II
Pick-off Compton	f_a	0.024(1)	0.020(1)
3γ decay Compton	f_b	0.0173(5)	0.0174(5)
Simultaneous Hit	f_c	0.0034(2)	0.0027(2)

Table 4.5: Background contamination within observed $n_{3\gamma}$

Notice that normalization between the observed o-Ps spectrum and the 3γ-spectrum from Monte Carlo simulation has been performed using the uncorrected $n_{3\gamma}$. While the observed spectrum contains the three types of backgrounds listed above, the 3γ-spectrum from the Monte Carlo spectrum can reproduce only two of them, that is the contribution from the 3γ-decay. Figure 4.17 schematically explains this relation; To make it clear, the figure is drawn with exaggeration.

In order to perform the normalization correctly, one should use the counts $n_{3\gamma} - f_a \times n_{pick}$, instead of using simply $n_{3\gamma}$. This correction affects $n_{3\gamma}$ value by 0.1 % level, thus it would be a good approximation if one performs renormalize operation for even a one time.

Table 4.6 summarizes the obtained value at the typical time window for both RUN I and RUN II. The large difference between $\lambda_{pick}/\lambda_{3\gamma}$ values of two runs stems from the different characteristics (mean grain distance) of the two powders. This will be clearly seen in Sec. 4.2.7.

4.2.7 Determination of $\lambda_{pick}(t)/\lambda_{3\gamma}$ as a function of time

In this section, time dependence of the ratio $\lambda_{pick}(t)/\lambda_{3\gamma}$ will be studied. The counting method which has been described in previous section, is now

	RUN I	RUN II
n_{pick}	106100(859)	151077(828)
$n_{3\gamma}$	1514540(1241)	1429240(1203)
$n_{3\gamma}$(pure)	1480643(1260)	1397490(1221)
$\lambda_{pick}/\lambda_{3\gamma}$	0.01049(8)	0.01582(9)
weighted mean time (ns)	287.5	284.3

Table 4.6: Summary of $\lambda_{pick}/\lambda_{3\gamma}$ estimation for the typical time window ($150 - 700$ ns). The numbers inside parenthesis are statistical errors which include the propagated errors from the accidental and Monte Carlo spectrum. The counting method is applied for the events winthin the time range of $150 - 700$ ns

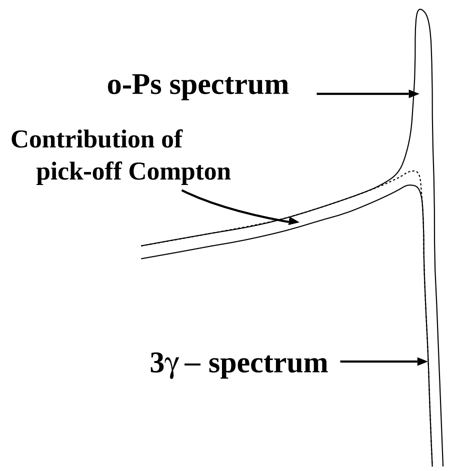

Figure 4.17: Schematic drawing explaining the contribution from the Compton scattered pick-off events to the normalization factor between the observed spectrum and result of the Monte Carlo simulation.

applied for the various time windows. Since the statistics of the o-Ps decay events are less in the later time, definition of the window width varies according to the time.

The time windows are defined as Table 4.7. The results of the counting method applied for each time-window are plotted in Fig. 4.18 and 4.19 for RUN I and RUN II respectively. Following the discussions in Sec. 3.1.3, data points in the figure can be fit with the differential equation (3.5). The fit is performed using the famous function minimization package *MINUIT* [72]. It it easily prospected by glancing the Eq. (3.5) that the fitting parameter C, θ_∞ and a_j are strongly correlating to each other, then the error matrix

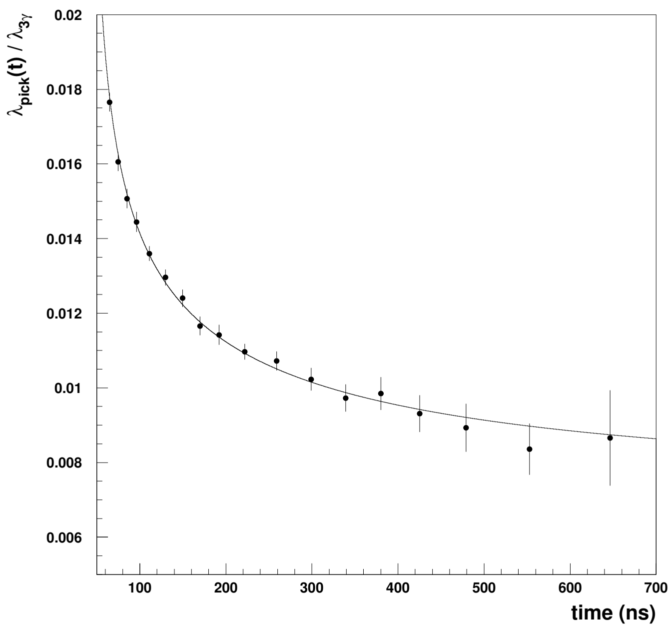

Figure 4.18: The ratio $\lambda_{pick}(t)/\lambda_{3\gamma}$ of RUN I plotted as a funtion of time. The solid line shows the fitting results; the procedure of fit is explained in the context. Note that the vertical scale is different from that of Fig. 4.19

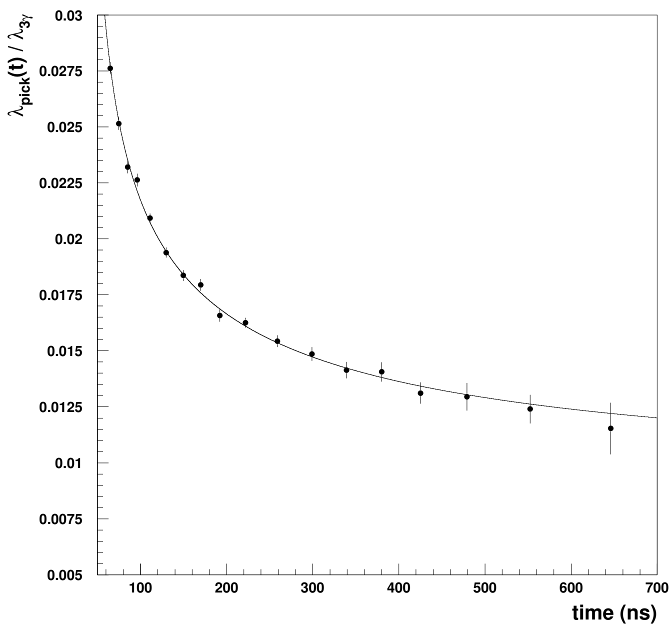

.

Figure 4.19: The ratio $\lambda_{pick}(t)/\lambda_{3\gamma}$ of RUN II plotted as a funtion of time.

time range	window width	# of window
40-50 ns	5 ns	2
50-100 ns	10 ns	5
100-200 ns	20 ns	5
200-400 ns	40 ns	5
400-500 ns	50 ns	2
500-800 ns	100 ns	3

Table 4.7: Definition of the time windows

or the covariance matrix [††] won't be properly diagonalized and resulting to a poor error estimation. From these technical reasons and for the sake of simplicity, the polynomial term in Eq. (3.5) should be represented by a power law, i.e.

$$\frac{d}{dt}\theta(t) = -C\left(\theta(t)^2 - \theta_\infty^2\right)\theta(t)^{2\beta}, \tag{4.13}$$

where numerous parameters are substituted with one new fitting parameter β. This notation is identical to the one which can be found in reference [57] where parameter β is optimized to be 2.2 ($2 \sim 2.5$) for the o-Ps in silica aerogel within 0.92 amagat of He gas (1 amagat$\equiv 2.69 \times 10^{25}$ atom m^{-3}, the number density of an ideal gas at 0 $°C$ and 1 atm).

The measured $\lambda_{pick}(t)/\lambda_{3\gamma}$'s are fitted with Eq. (4.13). Since the Eq. (4.13) is not those differential equations that can be solved analytically, the equation is solved numerically using the Runge-Kutta method. Specifically, subroutine code DDEQMR in CERN LIB [73] is made use of for solving the first-order differential equation. To solve the differential equation, one fixed data-point is needed as a calculation start point; $\lambda_{pick}(t)/\lambda_{3\gamma}$ value within the $45-50$ ns is used for it. Since the ratio $\lambda_{pick}(t)/\lambda_{3\gamma}$ suffers a influence from prompt peak, the fast time region is not reliable, thus the data-points after 45 ns is used for fit. From sub-figure of Fig. 4.8, one can confirm that it takes about 40 ns to completely eliminate the influence of prompt peak.

Following four fitting parameters are used,

1. Constant factor C, which determines the rate of variation in $\theta(t)$ curve.
2. Asymptotic value θ_∞.
3. A power low constant, β, the effect of energy dependence on thermalization process. This variable determines the degrees of twisting in $\theta(t)$ curve.
4. The deviation of one fixed point from the data-point within $45-50$ ns. In order to estimate the dependencies of the fitting result on the fixed

[††] It is defined as a inverse of the second derivative matrix of the function with respect to the parameters.

point, the deviation from the data point is considered as a fit parameter.

To fit the discrete data points with the continuous fitting funtion, the binning effect must be taken into account. Typical $\theta(t)$ value in i-th time window, $\overline{\theta_i}$, is determined to be a mean value weighted with the o-Ps populations $N(t)$,

$$\overline{\theta_i} = \frac{\displaystyle\int_{t\in i-th\ window} \theta(t)N(t)}{\displaystyle\int_{t\in i-th\ window} N(t)} \tag{4.14}$$

The result of the best fit is drawn upon the Fig. 4.18 and Fig. 4.19 for RUN I and RUN II respectively.

Table 4.8 shows the result of the fit parameters. The errors of parameters are estimated by calling MINOS error analysis routines in the MINUIT package [72]. The minimization is done for the chisquare of the parameterized function. MINOS is reliable since it takes account of non-linearities in the parameter space of chisquare. MINOS can calculate the error of the first three parameters thus they have the asymmetric errors as in Table 4.8, whereas MINOS cannot estimate the error for the fourth parameter that the parabolic error is attained with somewhat downgrade error analysis package called HESSE [72]. For the purpose of investigating the uncertainties of fit, following operations are carried out. At first, one out of four parameters is fixed at the value which deviates from the best fit value by 1 σ while the rest parameters are left free; the error values in Table 4.8 are used as 1 σ. The second fit with three free parameters is carried out for each parameter, yielding the fit uncertainty due to the fixed parameter. Figure 4.20 and 4.21 show the deviation of the second fit from the best fit for RUN I and II respectively. Each line shows the respective deviation from the best fit. The results of these error estimations will be used in later at the time spectrum fitting.

parameters	for RUN I	for RUN II
C	$0.166 \times 10^{-2}\ {}^{+0.43\times10^{-3}}_{-0.45\times10^{-3}}$	$0.522 \times 10^{-3}\ {}^{+0.16\times10^{-3}}_{-0.14\times10^{-3}}$
θ_∞	$0.761 \times 10^{-2}\ {}^{+0.90\times10^{-3}}_{-0.17\times10^{-2}}$	$0.999 \times 10^{-2}\ {}^{+0.12\times10^{-2}}_{-0.22\times10^{-2}}$
2β	$2.64\ {}^{+0.35}_{-0.30}$	$2.12\ {}^{+0.25}_{-0.22}$
deviation	$-0.27 \times 10^{-4} \pm 0.27 \times^{-4}$	$-0.32 \times 10^{-4} \pm 0.32 \times^{-3}$
χ^2/d.o.f	9.53/(23-4)	12.27/(23-4)

Table 4.8: Summary of $\lambda_{pick}(t)/\lambda_{3\gamma}$ fitting result

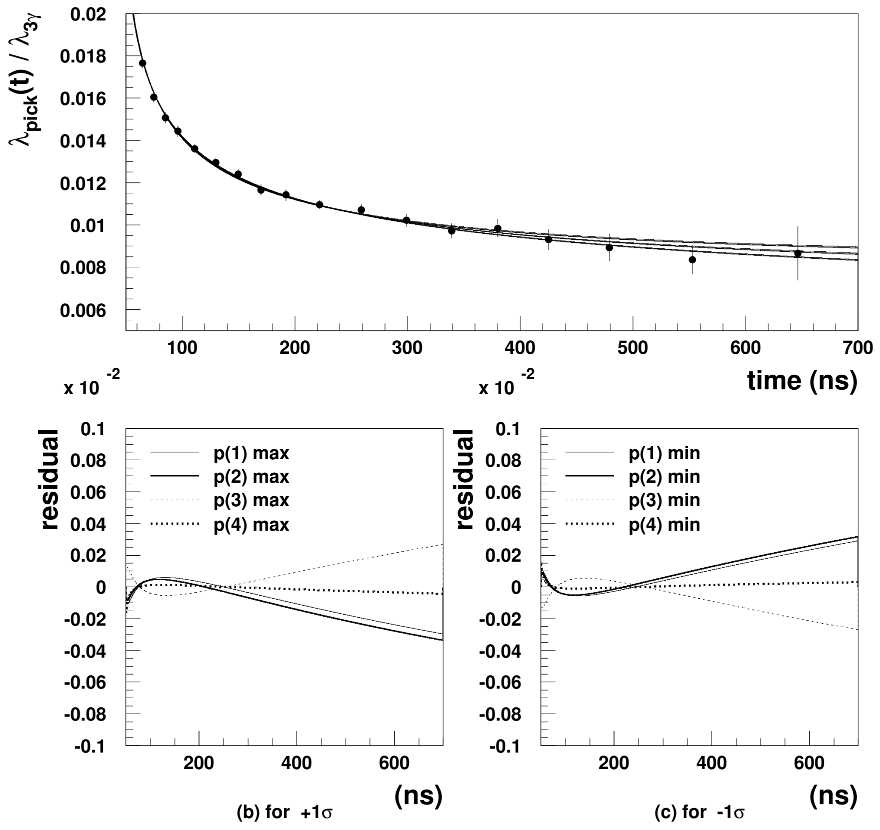

Figure 4.20: Uncertainties of the fit are plotted as a function of time for RUN I. In order to study the parameter dependencies of fit, one of the parameters has been fixed at the value which is 1σ large (positive error) or small (negative error) from the best fitting value, and similar fitting operation is performed again with three free parameters. Upper figure shows the similar plot as in Fig. 4.18, superimposed lines are representing fit uncertainties attributed to each parameter. Lower figures (b),(c) shows the residuals of three parameter fitting result from the best fit; they are plotted as a function of time, and $P(1) \sim P(4)$ stand for the parameters defined in the context.

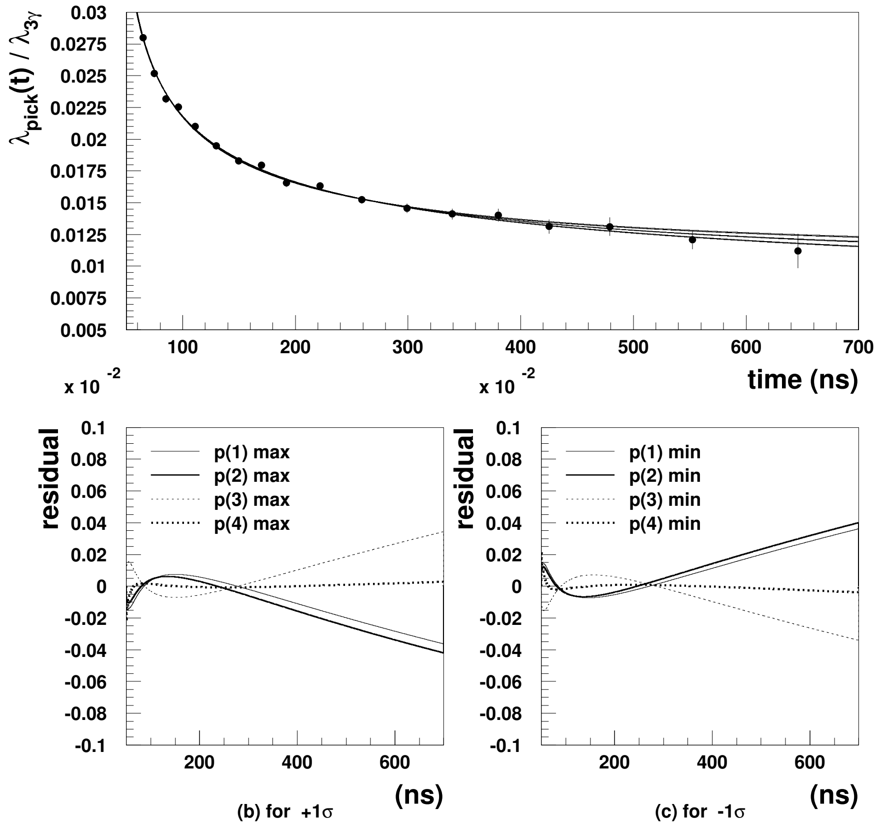

Figure 4.21: Uncertainties of the fit are plotted as a function of time for RUN II. The procedures are same as Fig. 4.20.

From the figures, one can easily see that the o-Ps thermalization in SiO_2 powder is a slow process, and it takes more than 600 ns to be completely thermalized.

4.3 Decay Rate Fitting

In this section, the time spectra obtianed with NaI(Tl) scintillators are fitted to yield the intrinsic decay rate of o-Ps. As already described in Sec. 3.1.3, the direct 2γ correction methodis used for the fit; it takes into account the thermalization process which has just been derived in the previous section.

4.3.1 Energy selection

Figure 4.22 and 4.23 represent the energy spectrum of the NaI(Tl) scintillator for RUN I and RUN II respectively; the events in the time range of $-5 \sim +5$ ns (prompt events) are sliced out to examine its energy response.

The fit function Eq. (3.9) contains the factor $\varepsilon_{pick}/\varepsilon_{3\gamma}$, which must be determined with the Monte Carlo simulation alone. Fortunately the uncertainty of this factor is suppressed both by the small pick-off ratio, $\lambda_{pick}(t)/\lambda_{3\gamma} \sim 0.01$ and by the small value of itself, $\varepsilon_{pick}/\varepsilon_{3\gamma} \sim 0.1$. However from Fig. 4.18 and 4.19, it is obvious that $\lambda_{pick}(t)/\lambda_{3\gamma}$ value grows suddenly before 100 ns. Thus the effect from relative efficiency ratio is no longer negligible, and it is desired to use a small $\varepsilon_{pick}/\varepsilon_{3\gamma}$ region as far as possible. Therefore the Compton free region of $370 - 440$ keV is adopted for fit; this range is shown as a shaded area of sub-figures in Fig. 4.22 and Fig. 4.23. The dependence of the energy selection will be discussed in Sec. 4.4

4.3.2 Base-Line Condition of NaI(Tl) signal

As illustrated in Fig. 3.13, the base-line condition of NaI(Tl) scintillator is measured for each events. Since this information observes the subtle movement of ground-line condition, it can be used as an sensitive indicator for the good events.

Base-Line condition of NaI(Tl) for RUN I

It can be conjectured that time-dependent fluctuation of the base-line condition easily deforms the time-spectrum shape. Thus one can evaluate the validity of the time-spectrum by examining the base-line condition along the time direction.

Unfortunately, the measured base-line conditions of NaI(Tl)s in RUN I have some time-dependent fluctuation. Figure 4.24(a)$\sim$(d) clearly shows these behaviors. Center of the base value gradually waves along the time base. It is anticipated that these fluctuations comes from the cross-talk

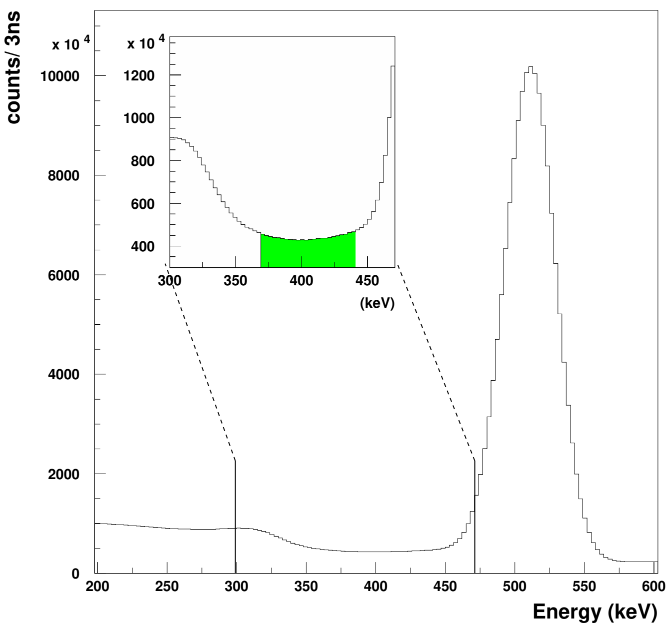

Figure 4.22: The energy spectrum of the NaI(Tl) scintillator #0 for RUN I. The prompt events (from -5 ns to $+5$ ns) are extracted.

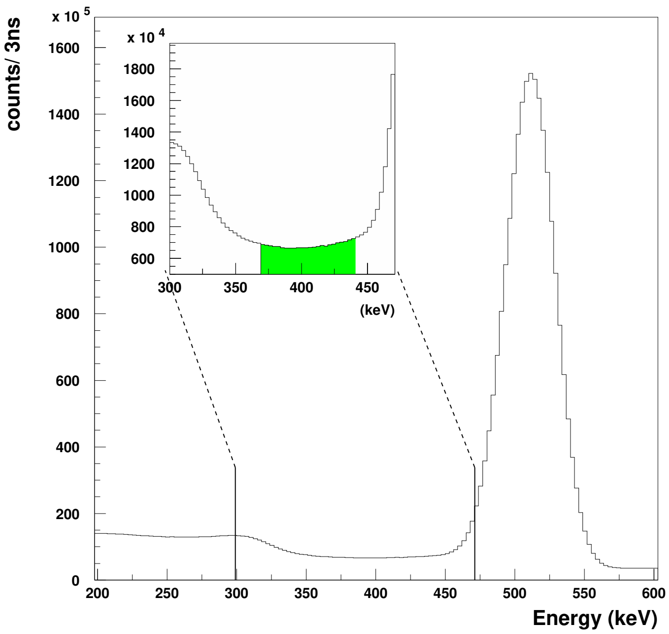

Figure 4.23: The energy spectrum of the NaI(Tl) scintillator #0 for RUN II. The prompt events (from -5 ns to $+5$ ns) are extracted.

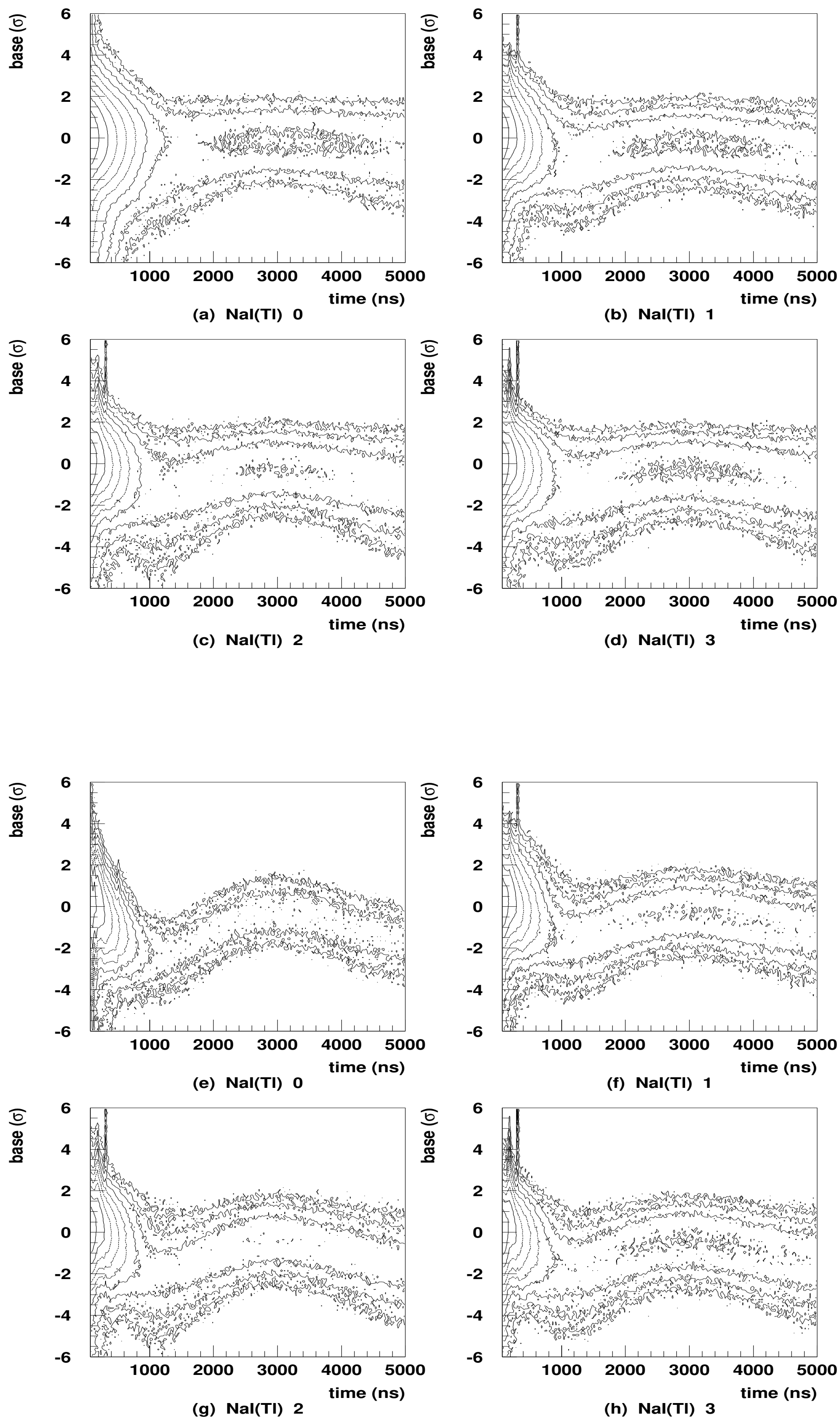

Figure 4.24: Contour plot of the base-line condition of NaI(Tl) scintillators versus detection timing without cut for RUN I. The base values are expressed in σ unit (see table 4.2). Figure (a)$\sim$(d) show the distribution without selection. In figure (e)$\sim$(h), only the events which have more than two NaI(Tl) hits are plotted.

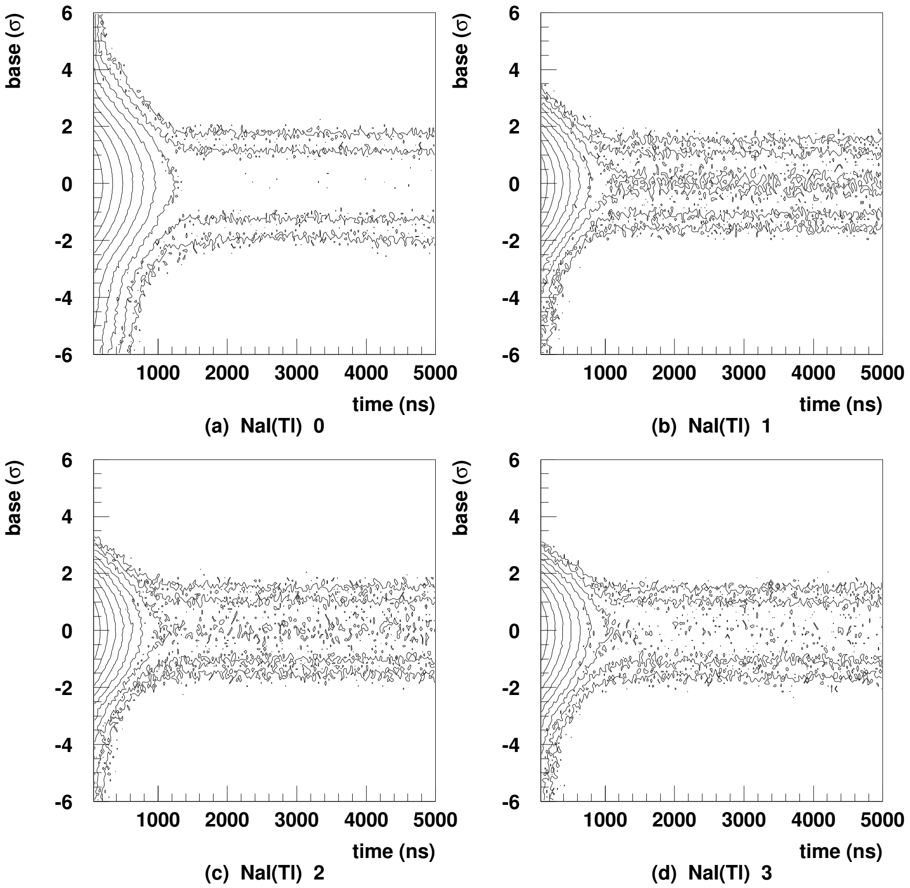

Figure 4.25: Contour plot of the base-line condition of NaI(Tl) scintillators versus detection timing for RUN I. The base values are expressed in σ unit (see table 4.2). Selected events requiring single NaI(Tl) hit are plotted.

effect between the detectors, because,

- The signal from each four NaI(Tl) goes through the identical electric module.
- The time dependencies are observed, which indicates the origins of this fluctuation are synchronizing to the decay timing. A large signal of 1274.6 keV hits the detector at time zero, and it can contribute to a large fraction of event hit.

Thus it can be suspected that the detection of 1274.6 keV-γ on the other detectors swings the base-line electrically. Then it is worth trying to cut events that have more than two NaI(Tl) hits. Figure 4.24 (e)$\sim$(h) shows the same kind of plots as Fig. 4.24 (a)$\sim$(d) but only events which have more than two NaI(Tl) hits are plotted. This time, the behavior is much more obvious and one can see that each signal has a similar wave property.

On the other hand, single NaI(Tl) hit events are plotted in Fig. 4.25; the base-line conditzion are clearly flat over the wide time range. Therefore the clean time-spectrum can be obtained by requiring single hit condition for RUN I.

Base-Line condition of NaI(Tl) for RUN II

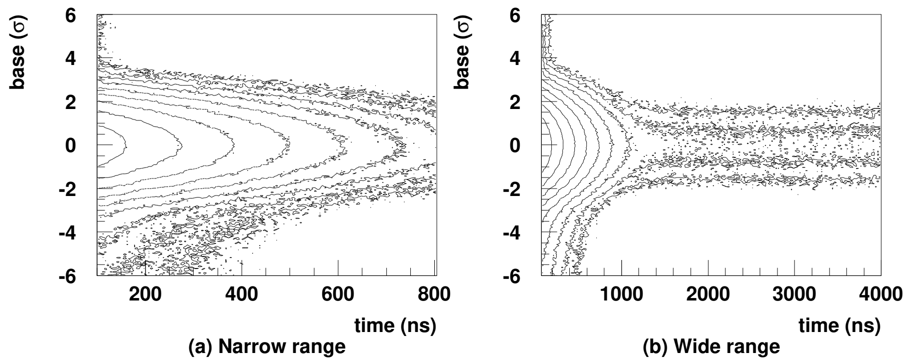

Figure 4.26: Contour plot of the base-line condition of NaI(Tl) scintillators versus detection timing for RUN I. The base values are expressed in σ unit (see table 4.2). Selected events requiring single NaI(Tl) hit are plotted.

Contrary to RUN I, only one NaI(Tl) scintillator is used in RUN II.

Thus the behaviour discussed in previous section never occur this time. As in Fig. 4.26, quite clean base-line condition is obtained without any selection.

Base-Line cut

As a cut condition, the events with base values within the range, $-4 <$ BASE $(\sigma) < +4$, are selected for both RUNs. Figure 4.27 shows the distribution of base-line condition of NaI(Tl) and its cut condition for RUN I, and Fig. 4.28 display the same plot for RUN II.

The dependence of the base-line selection will be discussed in Sec. 4.4.

4.3.3 Selection for the Non Pile-Up Events

As described at (n.7) in Sec. 3.2.5, pile-up events can spoil the energy information and result in the wrong correction for the time-walk. These events can be excluded by requiring the WD-NW condition, i.e. by examining relative difference of the wide-gate ADC value and the narrow-gate ADC value. As a cut condition, the events whose (wide–narrow) values lie within the range -30 keV $<$ (wide $-$ narrow) $<$ 30 keV, are selected for both RUNs. Figure 4.29 shows distribution of this (wide–narrow) values in keV unit and its cut condition as a vertical lines. The width of peak structure represents the fluctuation of signal shape during the narrow ADC gate, since the narrow ADC gathers a part of the total signal charge. Different peak width found in Fig. 4.29 reflects this effect. Since the RUN II adopts the narrow gate width longer than that of the RUN I, sharp (wide–narrow) peak is obtained in RUN II.

Figure 4.30 shows the (wide–narrow) distribution for RUN II in a reduced scale. It can be clearly verified that the pile-up events stretching over to a positive side of the peak are well rejected by the above cut condition. The tail events stretching to negative side of the peak are attributed to the under-shoot of the signal; since the under-shoot events result in a mal energy information, it is appropriate to reject these events.

The dependence of the (wide–narrow) value selection will be discussed in Sec. 4.4.

4.3.4 Time Spectrum of NaI(Tl) Scintillator

Two time spectrum from the energy window of $370 - 440$ keV are presented in Fig. 4.31 and in Fig. 4.32 for RUN I and RUN II respectively. These spectrum have the same structure as those of Ge detectors. A sharp peak of the prompt peak is followed by the exponential decay curve of o-Ps, and finally the constant accidental spectrum appears. From the figures, it can be seen that the o-Ps curve is observed over the wide range of about 1.2 μs corresponding to about eight times the o-Ps lifetime. This is in part due to the weak positron source of 0.03 μCi is in use; as the number of o-Ps

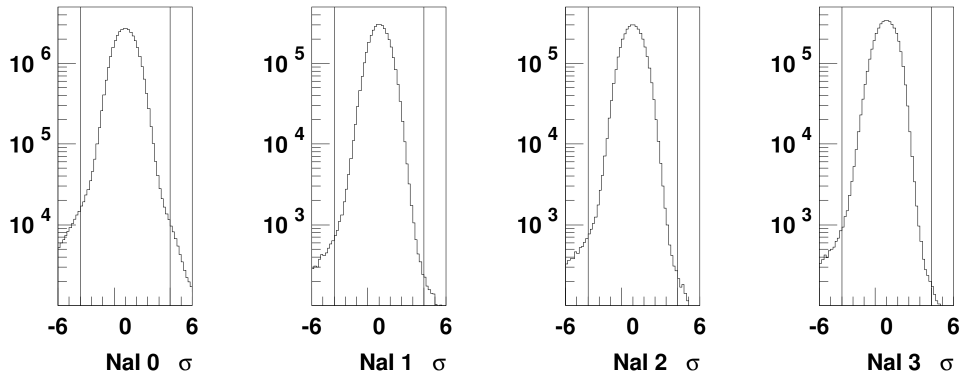

Figure 4.27: Base-line distribution of 4 NaI(Tl) for RUN I. Vertical lines indicate the cut condition borders of $\pm 4\sigma$. The events after 50 ns are selected, i.e. the prompt peaks are not included in the figures.

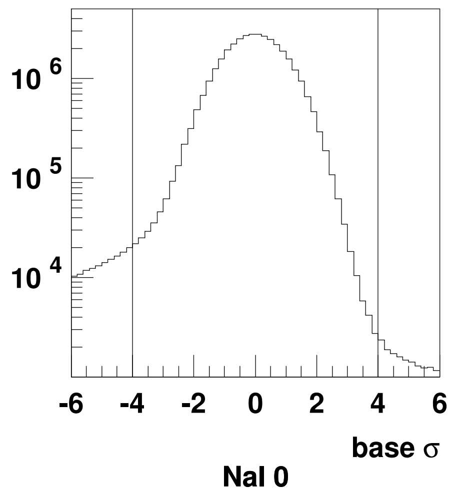

Figure 4.28: Base-line distribution of NaI(Tl) for RUN II. Same as above figures, the events after 50 ns are selected. Vertical lines indicate the cut condition borders.

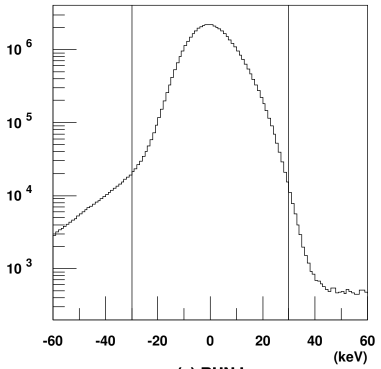

(a) RUN I

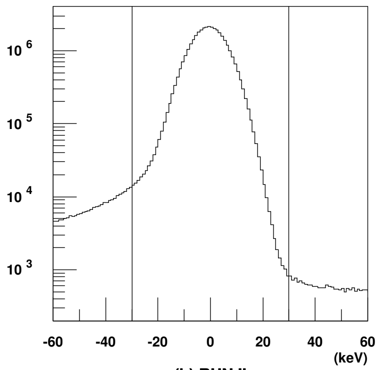

(b) RUN II

Figure 4.29: The difference between the wide and narrow gate ADC value. Figure (a) represents the total NaI(Tl) (0$\sim$3) events for RUN I while Fig. (b) represents the NaI(Tl) 0 events for RUN II. The vertical lines indicates the cut condition boarders of wide $-$ narrow $= \pm 30$ keV. The events lying within the energy window of $370 - 440$ keV are selected.

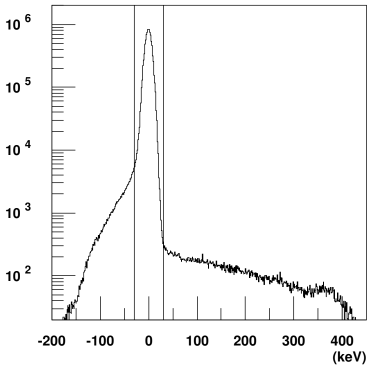

Figure 4.30: The distribution of the (wide–narrow) values for RUN II in a reduced scale. The events lying within the energy window of $370-440$ keV are selected.

events is proportional to the strength of source, i.e. $N_{o-Ps} \propto \mathcal{S}$, while the accidental event rate is proportional to the square of source strength $N_{acci} \propto \mathcal{S}^2$, where $\mathcal{S}$ stands for the source strength. For another reason, the accidental contributions are well suppressed by selecting the γ-energy.

The sub-figures in Fig. 4.31, 4.32 show the enlarged view of the prompt peaks, good time resolutions of $\sigma = 2.21$ ns and $\sigma = 2.01$ ns are obtained for the combined (0$\sim$3) NaI(Tl) of RUN I and NaI(Tl)-0 of RUN II respectively.

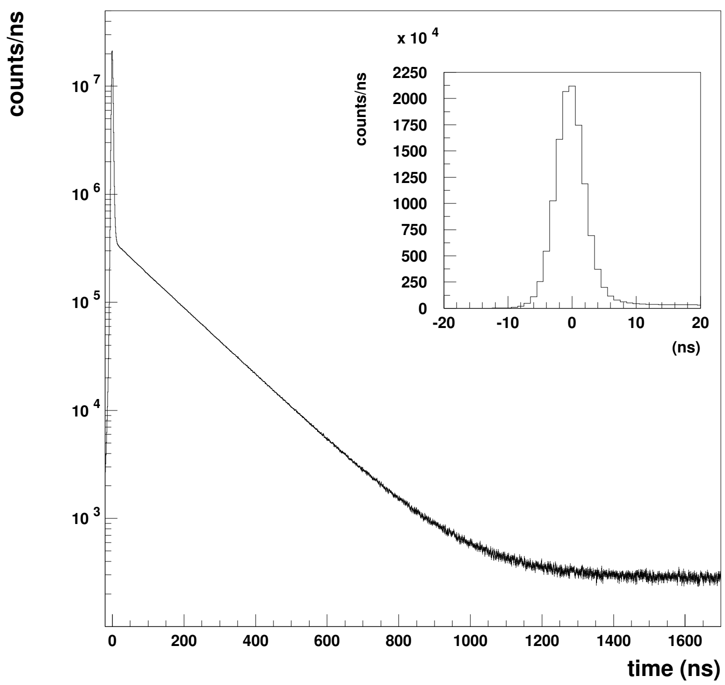

Figure 4.31: Time spectrum of NaI(Tl) scintillators for RUN I at the energy window of 370–440 keV. Events from four NaI(Tl) (0$\sim$3) are summed up. Base-line conditions are restricted to be within $\pm 4\sigma$, and (wide–narrow) values within $\pm$30 keV are selected. Sub figure shows the enlarged view of the prompt peak.

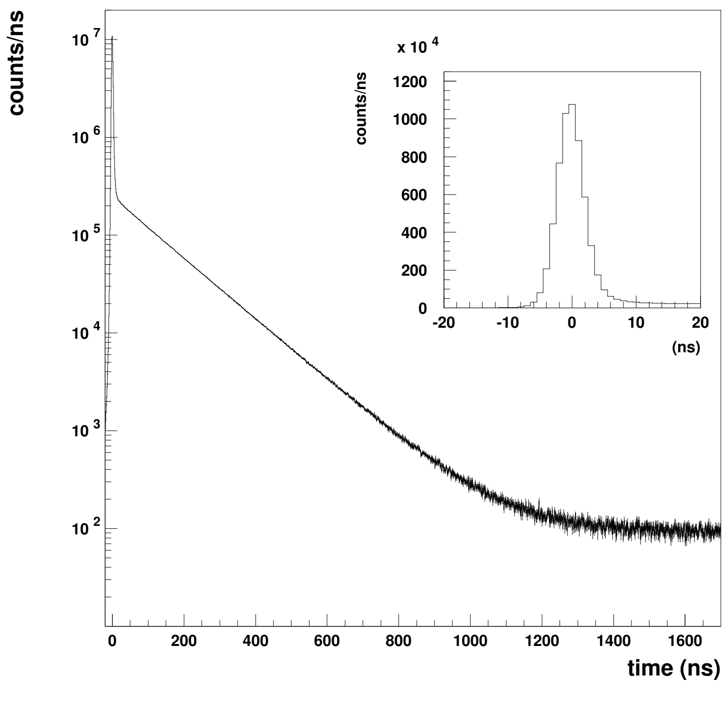

Figure 4.32: Time spectrum of NaI(Tl) scintillator for RUN II at the energy window of 370–440 keV. Events are selected with same condition as in RUN I. Sub figure shows the enlarged view of the prompt peak.

4.3.5 Time Spectrum Fitting

The expected time spectrum without the presence of prompt peak is derived in Sec. 3.1.3. The final equation form is given by,

$$N_{obs}(t) = e^{-R_{stop}t}\left[\left(1+\frac{\varepsilon_{pick}}{\varepsilon_{3\gamma}}\frac{\lambda_{pick}(t)}{\lambda_{3\gamma}}\right)N_0 \exp\left(-\lambda_{3\gamma}\int_0^t\left(1+\frac{\lambda_{pick}(t')}{\lambda_{3\gamma}}\right)dt'\right)+C\right]. \tag{4.15}$$

the ratio $\varepsilon_{pick}/\varepsilon_{3\gamma}$

In equation 4.15, ε_{pick} and $\varepsilon_{3\gamma}$ are the detection probability that γ's emitted from a pickoff annihilation and a o-Ps 3γ-decay deposit the selected energy (370–440 keV as a standard value) on the NaI(Tl) scintillator.

The ratio $\varepsilon_{pick}/\varepsilon_{3\gamma}$ is estimated by Monte Carlo simulation. The values for the scintillators are summarized in Table 4.9, 4.10. Because RUN I adopts the cut condition that the only single hit event among the NaI(Tl)'s has been accepted, the values must reflect that configuration in Monte Carlo simulation. As can be seen in Eq. (4.15), the ratio $\varepsilon_{pick}/\varepsilon_{3\gamma}$ is used in such

Scintillator	370–440 keV	380–430 keV	360–450 keV
NaI-0	0.0651(7)	0.0637(8)	0.0700(6)
NaI-1	0.433(3)	0.438(4)	0.435(3)
NaI-2	0.413(3)	0.404(4)	0.415(3)
NaI-3	0.151(2)	0.140(3)	0.170(2)

Table 4.9: The ratio $\varepsilon_{pick}/\varepsilon_{3\gamma}$ for RUN I. The values are estimated for several different energy selections.

Scintillator	370–440 keV	380–430 keV	360–450 keV
NaI-0	0.0607(6)	0.0579(7)	0.0645(5)

Table 4.10: The ratio $\varepsilon_{pick}/\varepsilon_{3\gamma}$ for RUN II.

a form that is multiplied by $\lambda_{pick}(t)/\lambda_{3\gamma}(\approx 0.01)$, thus the final result does not strongly depend on the detail of Monte Carlo simulation.

R_{stop} rate

The stop rate for each NaI(Tl) scintillator is measured several times between the run intervals. Typical values are shown in Table. 4.11. Each value is integrated into the time spectrum at histogram filling as a weight factor, $\exp(+R_{stop}t)$. Thus the factor $\exp(-R_{stop}t)$ is already compensated (or canceled) at time spectrum fit.

Scintillator	NaI-0	NaI-1	NaI-2	NaI-3
RUN I	1460 Hz	740 Hz	710 Hz	740Hz
RUN II	1220 Hz	—	—	—

Table 4.11: Typical stop rate of NaI(Tl) scintillators.

dependence on fitting start time

As a subsequent result from the above discussions, the remaining free parameters in Eq. (4.15) are just three, i.e. N_0, C, and $\lambda_{3\gamma}$. Note that the part of Eq. (4.15) containing time integration can be rewritten as,

$$\begin{aligned} & N_0 \exp\left(-\lambda_{3\gamma}\int_0^t \left(1+\frac{\lambda_{pick}(t')}{\lambda_{3\gamma}}\right)dt'\right) \\ &= N_0 \exp\left(-\lambda_{3\gamma}\int_0^{t_{start}} \left(1+\frac{\lambda_{pick}(t')}{\lambda_{3\gamma}}\right)dt' - \lambda_{3\gamma}\int_{t_{start}}^t \left(1+\frac{\lambda_{pick}(t')}{\lambda_{3\gamma}}\right)dt'\right) \\ &= \overline{N_0} \exp\left(-\lambda_{3\gamma}\int_{t_{start}}^t \left(1+\frac{\lambda_{pick}(t')}{\lambda_{3\gamma}}\right)dt'\right) \end{aligned} \tag{4.16}$$

All the uncertainties before fitting start time, t_{start} are absorbed into the re-defined free parameter, $\overline{N_0}$. Therefore the integration before t_{start} does not have any influence to the fitting.

time spectrum fitting for RUN I

Fitting the time spectrum of RUN I has one problem. As presented in Table 4.9, different size of ε rate will increase the degree-of-freedom in the fitting procedure, if one simply employs Eq. (4.15). On the other hand performing the fitting procedures to the four different time spectrum from the four NaI(Tl) independently makes no sense.

Consequently the following procedures are performed on the time spectrum of RUN I,

1. Firstly constant term C can be fitted (obtained) with using only the accidental flat part of time spectrum for each NaI(Tl).

2. Now that if one subtracts the flat spectrum from the time spectra, Eq. (4.15) shrinks into the product of following two part,

   (a) The NaI(Tl) dependent term,

$$\left(1+\frac{\varepsilon_{pick}}{\varepsilon_{3\gamma}}\frac{\lambda_{pick}(t)}{\lambda_{3\gamma}}\right) \tag{4.17}$$

(b) The NaI(Tl) independent term,

$$N_0 \exp\left(-\lambda_{3\gamma}\int_0^t \left(1+\frac{\lambda_{pick}(t')}{\lambda_{3\gamma}}\right)dt'\right) \tag{4.18}$$

3. Above NaI(Tl) dependent term can be excluded from the each time spectrum by dividing them with the term (4.17).

4. Adding (recovering) the constant term C which has been subtracted at point 1, to a respective time spectrum.

5. Finally time spectrum of each NaI(Tl) has been transformed into the shape that can be fitted with the rather simple function,

$$N(t)_{transformed} = \overline{N_0}\exp\left(-\lambda_{3\gamma}\int_{t_{start}}^t \left(1+\frac{\lambda_{pick}(t')}{\lambda_{3\gamma}}\right)dt'\right) + C. \tag{4.19}$$

At this stage, the four time spectra can be summed up into one spectrum, and one can perform the time spectrum fitting with Eq. (4.19).

The time spectrum is fitted using the minimization package [72] by a least-square-fit method. Now that the free parameters remained are following three, $\overline{N_0}$, $\lambda_{3\gamma}$, C.

The data used in the fit corresponded to times in the time spectrum between 60 ns and 5000 ns. After the first fit, the fit is repeated moving the fitting start time out by 10 ns. The fitting start time is stepped out in this way between 60 ns and 500 ns.

The obtained decay rates in μs^{-1} are plotted as a function of fitting start time in Fig. 4.34. Note that the each fitted value of $\lambda_{3\gamma}$ in the figure is not independent of the others. If the two fitting start time, t_1, t_2 are close together, the corresponding decay rate λ_1 and λ_2 are highly correlated, that is the standard deviation of the difference is smaller than their individual errors.

In figure 4.34 the horizontal small-lines on the error bar indicate statistical errors solely due to NaI(Tl) time spectrum fitting. On the other hand, the propagated errors due to the $\lambda_{pick}(t)/\lambda_{3\gamma}$ fitting uncertainties are estimated with the deviated $\lambda_{pick}(t)/\lambda_{3\gamma}$ curves; these are obtained for each fitting parameter as in Fig. 4.20. The total errors including the propagated errors are estimated as,

$$\sigma_{total} = \sqrt{\sigma_{NaI}^2 + \sum_{i=1}^{4}\left(\sigma_i^2\,(\max) + \sigma_i^2\,(\min)\right)} \tag{4.20}$$

where $\sigma_i^2(\max)$ and $\sigma_i^2(\min)$ are the deviated values obtained with the deviated $\lambda_{pick}(t)/\lambda_{3\gamma}$ curves for each parameter fixed at $\pm 1\sigma$ from the best fit. Figure 4.34 shows these total errors with the extending vertical bars.

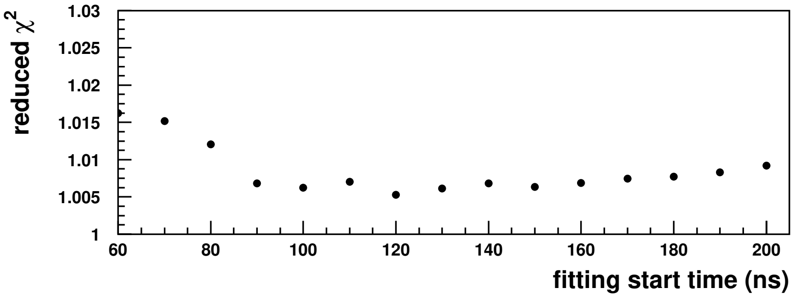

Figure 4.33: The reduced χ^2's plotted as a function of fitting start time for RUN I.

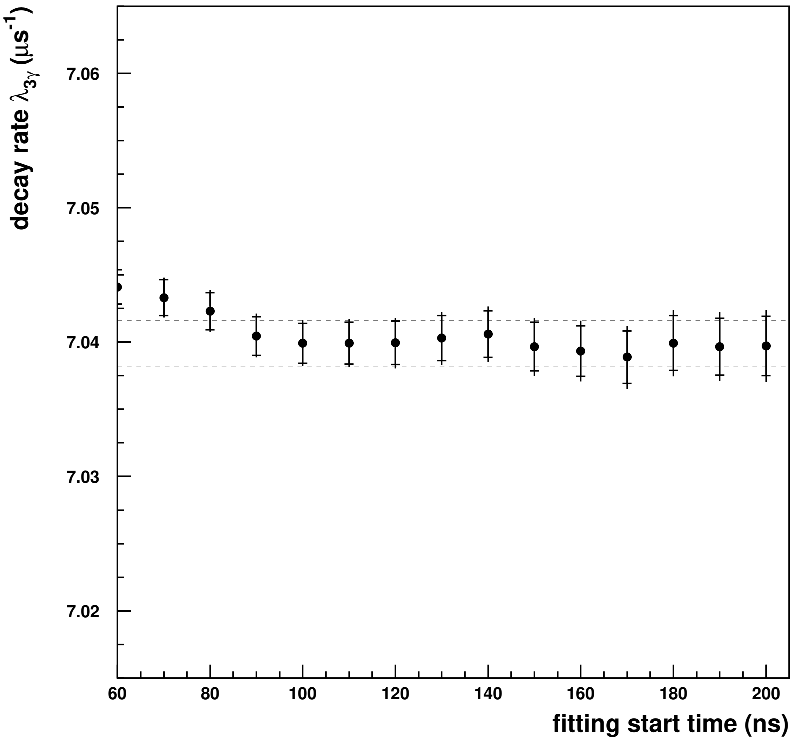

Figure 4.34: The fitted decay rates for RUN I are plotted as a function of fitting start time. The horizontal small-lines on the error bar indicate statistical errors solely due to fitting the NaI(Tl) time spectrum, while vertically extending bars include propagated errors from the $\lambda_{pick}(t)/\lambda_{3\gamma}$ fitting. The horizontal dotted lines show the one standard deviation region obtained at fitting start time = 100 ns.

As can be seen in Fig. 4.33, fitting χ^2 is rapidly increasing before 90 ns; thus the decay rate at 100 ns fitting start time is adopted as a resultant value. The dotted horizontal lines represent the one standard deviation err obtained at $t = 100$ ns fitting start. From the figure 4.34, one can confirm that the fluctuation of the decay rates are smaller than the statistic error after 100 ns.

Therefore the decay rate obtained with the RUN I data is determined to be,

$$\lambda_{3\gamma} = 7.03991 \pm 0.0017(stat.)\ \mu s^{-1}, \tag{4.21}$$

where only the statistic error is showed; this already includes the propagated error from $\lambda_{pick}(t)/\lambda_{3\gamma}$ fitting.

time spectrum fitting for RUN II

Unlike the complicated procedure applied for RUN I, the fitting process for RUN II is getting somewhat simpler because the ε ratio used in Eq. (4.15) is only one value as in Table 4.10.

Then the time spectrum is fitted with Eq. (4.15) by a least square method as in RUN I. The obtained decay rates for RUN II are plotted as a function of fitting start time in Fig. 4.36. As in RUN I, upper limit of the fitting range is fixed at 5000 ns, and the fitting start time is stepped out from 60 ns to 500 ns.

As in the RUN I, rapid increase of χ^2 is observed before 80 ns, yet another increase can be seen at $t = 150$ ns due to the bump-like structure as seen in the figure below. Thus the decay rate value obtained at the fitting start time $t = 100$ ns is used as a final value in common with RUN I.

Then the decay rate for RUN II is determined to be,

$$\lambda_{3\gamma} = 7.03935 \pm 0.0017(stat.)\ \mu s^{-1}. \tag{4.22}$$

This shows only the statistic error, including the propagated error from $\lambda_{pick}(t)/\lambda_{3\gamma}$ fitting.

Thermalization effect

In order to see the thermalization effect on the decay rate, and to see the advantage of the direct 2γ correction method, the time-spectra for each RUN are fitted with following normal exponential function,

$$N_{\rm norm}(t) = e^{-R_{stop}t}\Big(N_0 \exp\left(-\lambda'_{norm}t\right) + C\Big), \tag{4.23}$$

where λ'_{norm} is corrected by a factor of $(1 + \lambda_{pick}(t = 600\ ns)/\lambda_{3\gamma})$ to compensate the pick-off events and obtain the intrinsic value, λ_{norm}. It is assumed that the o-Ps is well thermalized in both SiO_2 powders till 600 ns after its formation, which can be confirmed from Fig. 4.18 and 4.19.

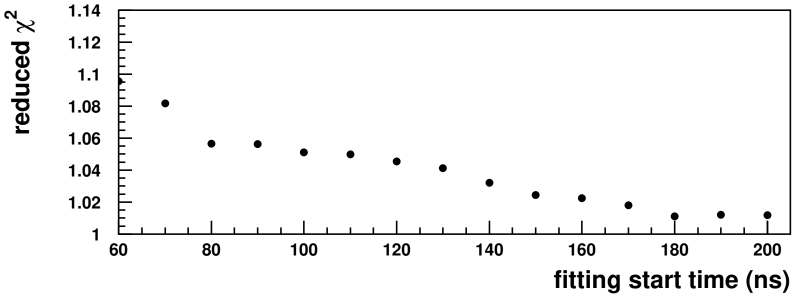

Figure 4.35: The reduced χ^2 's plotted as a function of fitting start time for RUN II.

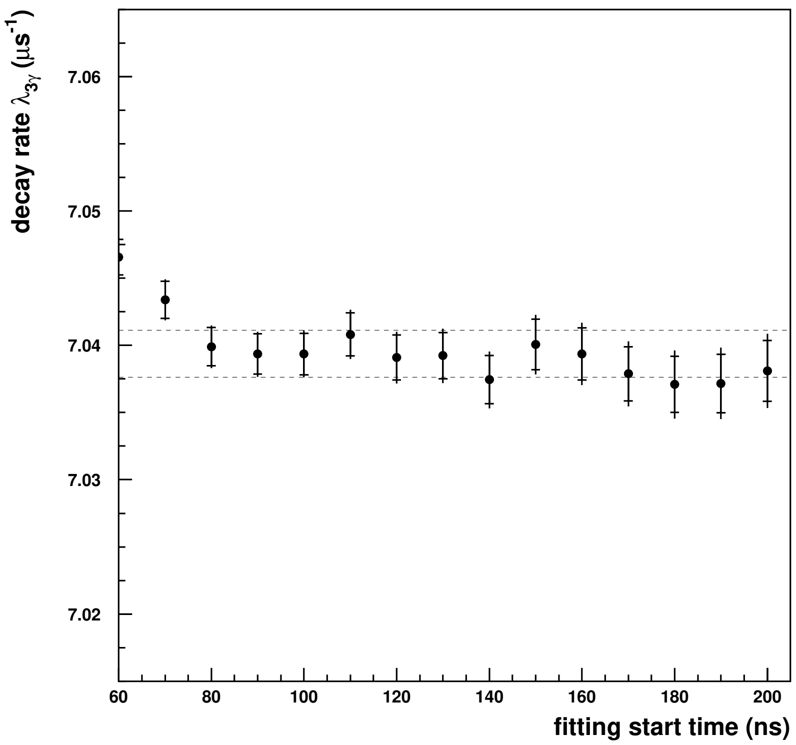

Figure 4.36: The fitted decay rates for RUN II are plotted against the fitting start time. The description of error bars are found in the caption of Fig. 4.34. The horizontal dotted lines show the one standard deviation region obtained at fitting start time = 100 ns.

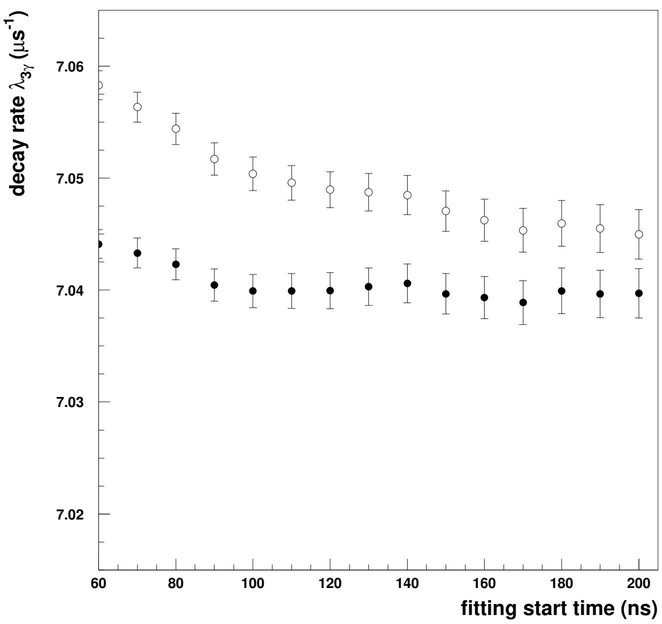

Figure 4.37: A comparison of the direct 2γ correction methodand the normal exponential fitting for RUN I. The open circles show the decay rates obtained with the normal exponential fitting. As in the context, the fitted values are corrected by a factor to compensate the pick-off effect. The closed circles represents the result from the direct 2γ correction method.

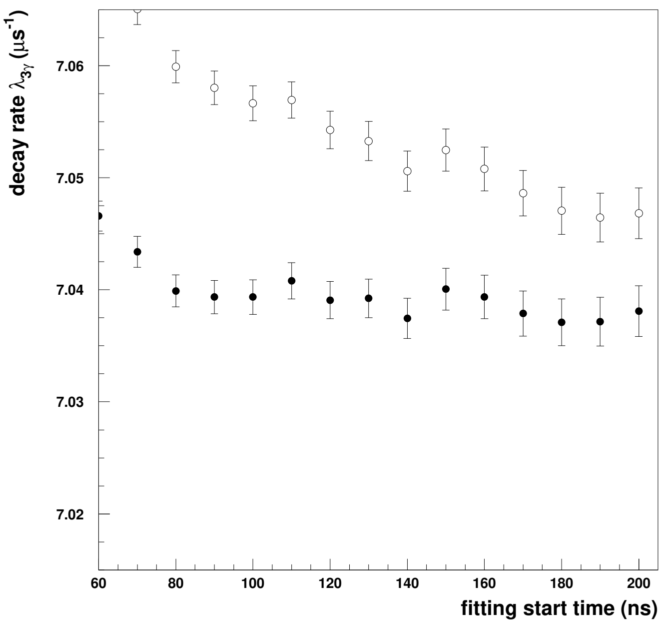

Figure 4.38: A comparison of the direct 2γ correction methodand the normal exponential fitting for RUN II.

In figure 4.37 and 4.38, the corrected λ_{norm} values are plotted as a function of the fitting start time with open circles. For a comparison, the values obtained with the direct 2γ correction methodare plotted with closed circles.

From the figure, it is obvious that the thermalization of o-Ps easily affects the final result, especially in the fast fitting start-time region. The fitted decay rate with Eq. (4.23) fall slowly to an asymptotic value around 600 ns. Note that in Cavity [6] and Gas [5] measurements they used the normal exponential function in the fitting procedure, and in addition they typically adopted $t = 170$ ns [6] and $t = 180$ ns [5] as the fitting start time. The figure shows that λ_{norm}, for instance at $t = 180$ ns is about 7.047, and it is likely that their higher decay rates were suffered from this thermalization effect.

The improvement of the method

As was already described in Sec. 3.1.4, the decay rates obtained in 1995 were systematically increasing before 200 ns fitting start time. In the current measurement no increase is observed till 90(80) ns for RUN I(II). Then let us consider possible explanation for this difference.

In 1995, the time spectrum was obtained with CsI(Tl) scintillators instead of NaI(Tl) scintillators and the fixed wide gate of 12 μs was provided to the ADC which is for CsI(Tl) energy. In addition, the gate opening timing was determined by the trigger PMT, instead of self-gate timing in the current measurement.

As a consequence, a lot of pile-up events were expected. Since the time-walk correction was determined from the energy information, the pile-up events could result in the tail effect in the time spectrum. Then let's assess a size of this tail with the specific values. In 1995, the signal from CsI(Tl) was integrated in a pre-amplifier with 70 ns time-constant. The longest time-walk can be estimated as, 70 $ns \times - \ln 0.1 \simeq 160$ ns if one assumes the lowest energy signal and 90% of the signal is below the threshold level of discriminator, since the time-walk rapidly increases in the lower energy region. These time-walk was corrected as in the current measurement, and needless to say these small signals were not used because they adopted the energy region of 300−410 keV. However if another signal, say accidental event, entered just after such small signal and totally deposited $300 - 410$ keV fake energy on ADC, these events could survive the energy cut condition and must have provided a wrong timing information because events in the energy range of $300 - 410$ keV needed little time-walk correction as in Fig. 4.4. Therefore the long tail spectrum from the huge number of the prompt events could easily disturb the o-Ps time spectrum; this tail effect had been observed as the rapid increase of the decay rate before 200 ns in 1995.

In the current measurement, these tail effect is suppressed because,

- The pile-up events are effectively rejected with the three types of ADC information.

- The outputs of the photomultiplier for NaI(Tl) are integrated with 23.5 ns time constant instead of 70 ns. Thus if the pile-up *could* occur, the tail effect can maximumly reach around 23.5 $ns \times -\ln 0.1 \simeq 54$ ns from the prompt peak.

The stable decay rates are observed after 90(80) ns fitting start time for RUN I(II) as a result of these improvements.

Consequently, the more precise result can be obtained in the current measurement due to the high statistics in the faster region of the o-Ps time-spectrum.

4.4 Systematic errors

Following systematic errors which might, or are known to affect the result are discussed. They are put into several categories, the TDC module related effects, the cut condition dependence, the MC dependence, and the other effects.

4.4.1 TDC module related systematic effect

As described in Sec. 3.2.6, used TDC (called KEK TDC) is a direct clock counting type TDC module that utilizes the external synthesizer as a clock source. The counter itself suffers no systematic effect, all the systematic errors can be attributed to the external clock source, if they exist.

– Calibration
  The calibration of the systhesizer is carried out before the runs to a frequency of 2 GHz within a 1-*ppm* level.

– Stability
  The frequency of the clock is guaranteed to be stable within 3-*ppm* against one year, and within 2.5-*ppm* against the temperature $-10°C\sim 50°C$owing to the high stability internal clock which compensates the temperature fluctuation.

– Integral Non Linearity
  Less than ± 1 miss count per 16-bit word length can occur, thus maximally the 15-*ppm* INL can happen.

– Differential Non Linearity
  Since the final time spectrum fitting is carried out with the histogram whose bin width is defined as 1 *ns* (twice the intrinsic TDC module resolution). Thus fundamentally $0.4 - 0.5\%$ DNL can be observed for each bins. But in the process of transformation from the measured TDC histograms into the time spectrum histogram, there are several factors which smear the DNL, such that, the time-walk correction and the fluctuation of T_0 timing, during the runs over the long time scale. Therefore the systematic effect due to the DNL is considered to be negligibly small.

These TDC related systematic errors are common to the two runs.

4.4.2 Cut condition dependence

The time spectrum of the NaI(Tl) scintillator which is used for the decay rate fitting is obtained through several data cutting. The dependence on the following cut conditions are estimated.

– Energy Selection

As described in Sec. 4.3.1, the optimized energy window used for the fitting is decided to be 370 – 440 keV. By spreading or reducing the selected window size, one can examine the energy window dependence.

The following deviations from the best fitted value are observed.

for RUN I

Lower Edge dependence	360–440 keV +105 ppm	365–440 keV +63 ppm	375–440 keV −18 ppm
Upper Edge dependence	370–435 keV +8 ppm	370–445 keV +54 ppm	370–450 keV +26 ppm

for RUN II

Lower Edge dependence	360–440 keV −99 ppm	365–440 keV −20 ppm	375–440 keV +114 ppm
Upper Edge dependence	370–435 keV +82 ppm	370–445 keV −61 ppm	370–450 keV −79 ppm

The fitting procedure suffers the uncertainties due to the rapid increase of $\varepsilon_{pick}/\varepsilon_{3\gamma}$ at the tail edge of the 2γ photo electric peak and near the Compton edge as inferred from Fig. 4.22, 4.23. Thus somewhat large deviations can be prospected at those ranges.

Since the 3γ-spectrum in this region is flat, the change of energy window definition means a drastic change of the event contents. Nevertheless above deviations are less than the halves of statistical one standard deviation; they are statistically consistent with the best fitting. Additionally, the above table shows no systematic orientation. Therefore one can conclude these deviations belong to statistical errors, and no systematic errors are assigned as to the energy selection.

– Base line Selection

The base line selection is applied as a cutting condition that the events within the range $-4.0\ \sigma \leq$ base line $\leq +4.0\ \sigma$ are selected as in section 4.3.2. The systematic error due to this condition is estimated by changing the domain of the base-line and surveying the deviation from the final result.

for RUN I

Lower Edge dependence	$-3.0 \sim +4.0$ +89 ppm	$-3.5 \sim +4.0$ +17 ppm	$-4.5 \sim +4.0$ −8 ppm	$-5.0 \sim +4.0$ −17 ppm
Upper Edge dependence	$-4.0 \sim +3.0$ −12 ppm	$-4.0 \sim +3.5$ +4 ppm	$-4.0 \sim +4.5$ +11 ppm	$-4.0 \sim +5.0$ +22 ppm

for RUN II

Lower Edge dependence	$-3.0 \sim +4.0$ −8 ppm	$-3.5 \sim +4.0$ −4 ppm	$-4.5 \sim +4.0$ +2 ppm	$-5.0 \sim +4.0$ +6 ppm
Upper Edge dependence	$-4.0 \sim +3.0$ −11 ppm	$-4.0 \sim +3.5$ −3 ppm	$-4.0 \sim +4.5$ +12 ppm	$-4.0 \sim +5.0$ +23 ppm

This condition is different from the energy selection in that the deviation of the ranges cause slight difference on the event statistics; that is the contents of the above selections are highly conrrelated. Thus small deviation from the best fit is expected; this can be confirmed in above tables. For RUN I, from -17 *ppm* to $+89$ *ppm* is assigned, and for RUN II from -11 *ppm* to $+23$ *ppm* is assigned for systematic error.

– WD-NW condition
In Sec. 4.3.3, the events whose WD-NW value lie within −30 keV∼30 keV are selected in order to reject the pile-up events. To investigate the influence of this cut condition, the cut domain is changed.

for RUN I

Range	−25 keV∼+25 keV +45 ppm	−35 keV∼+35 keV −6 ppm	−40 keV∼+40 keV +6 ppm

for RUN II

Range	−25 keV∼+25 keV −20 ppm	−35 keV∼+35 keV −6 ppm	−40 keV∼+40 keV −6 ppm

As in base-line selection, this condition is also a edge cut, thus one can expect the small deviation from the best value. The assigned systematic errors are -6 *ppm* $\sim +45$ *ppm* for RUN I, and -20 *ppm* for RUN II.

– Dependence on the Trigger PMT Threshold
In Sec. 4.1.5, the time walk correction is performed for trigger PMT. Figure 4.6 shows that the correction has been successfully carried out. However some fraction of events still remain uncorrected well due to the broad time response nature of the events near threshold. Therefore in order to check the threshold dependence, the same fitting procedure is performed on the different time spectra obtained with different threshold. Figure 4.39 shows the energy spectrum of trigger scintillator. From the figure it is obvious that the threshold changes of +10 channel, +20 channel is enough to investigate the dependence.

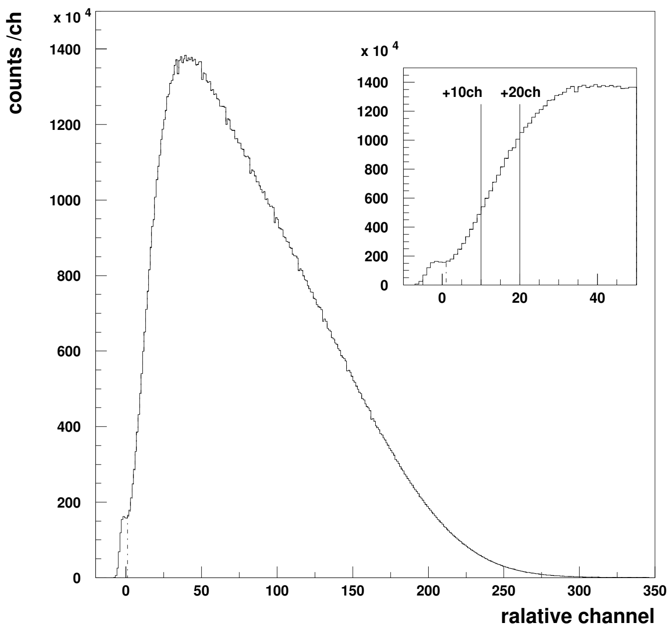

Figure 4.39: Energy spectrum of trigger scintillator (β^{+} from ^{22}Na. The horizontal axis represents a relative ADC channel in terms of the trigger threshold. The subfigure at upper right corner is a enlarged view of the spectrum near threshold.

for RUN I

Threshold Level	+10 channel	+20 channel
	+22 ppm	-10 ppm

for RUN II

Threshold Level	+10 channel	+20 channel
	+14 ppm	+15 ppm

These deviations can be attributed to the statistical fluctuations. Then one can neglect this effect.

4.4.3 Monte Carlo simulation dependence

– Normalization

In the analysis, the $\lambda_{pick}(t)/\lambda_{3\gamma}$ ratio is calculated with the counting method. The number of pick-off events are extracted by subtracting the 3γ-spectrum from the o-Ps spectrum as in Fig. 4.13. In this process, the 3γ-spectrum which is calculated with the Monte Carlo simulation is normalized with the measured data at the narrow range of 480 keV–505 keV.

Uncertainty of this normalization and the mal shape of 3γ-spectrum could change the $\lambda_{pick}(t)/\lambda_{3\gamma}$ value and provide a biassed result. Systematic errors according to this uncertainty is estimated by checking the symmetry of the residual pick-off peak. Because the sharp fall-off of the 3γ-spectrum at 511 keV is expected due to the phase space cutoff, and this fall-off is only smeared by the Ge energy resolution (σ ~0.5 keV), while the pick-off has twice the width (σ ~1.05 keV), the subtraction mainly affects the lower side of pick-off spectrum. This can be seen in Fig. 4.40 and 4.41 where the only left side of the pick-off spectrum is distorted by changing the subtraction normalization factor by +1.0%, −1.0%.

From the figures, one can easily find that the position of peak centroid is not sensitive to this distortion at all. Instead we define a new parameter ξ_{asym} which is defined as,

$$\xi_{asym} = \left(\sum_{\mathrm{E=507.0\ keV}}^{\mathrm{E<511.0\ keV}} N(E) \right) / \left(\sum_{\mathrm{E>511.0\ keV}}^{\mathrm{E=515.0\ keV}} N(E) \right), \tag{4.24}$$

where $N(E)$ is observed number at E keV in the pick-off spectrum. The ξ_{asym} parameter is sensitive to the asymmetry level of the peak spectrum and also to the position of centroid. Table 4.12 summarizes the obtained ξ_{asym}-parameters for three normalization factors together with the ξ_{asym}-parameters for the prompt events. Figure 4.42, 4.43

Normalization	−1.0% MC	±0.0% MC	+1.0% MC	Prompt
RUN I	1.069	1.018	0.966	1.024
	±0.018	±0.018	±0.018	
RUN II	1.039	1.010	0.98	1.014
	±0.012	±0.012	±0.012	

Table 4.12: Summary of the ξ-parameters

show these relations. Since the dominant component of the prompt events is annihilation, ξ-parameter value for the prompt peak is a good indicator when the validity of subtraction is estimated. From the figures, it is obvious that the ξ-parameters of prompt peaks are consistent with ξ-parameter value at ±0.0% MC for both RUNs; this indicates the subtraction is properly performed. From 1σ error at the normalization ±0.0% being shown as a horizontal band in the figures,

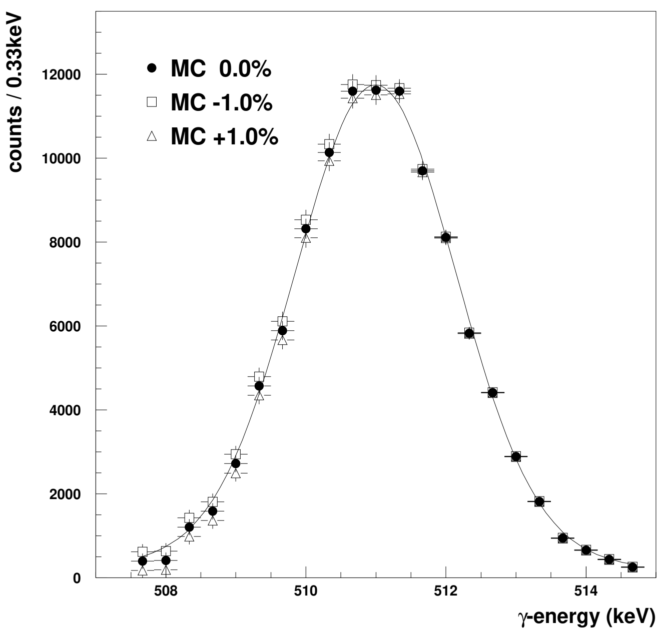

Figure 4.40: The pick-off spectrum of RUN I. Closed circles represent the pick-off spectrum extracted from the normal normalization factor (0.0%). Open squares and open triangles are extracted by changing the normalization factor by -1.0%, $+1.0\%$ respectively.

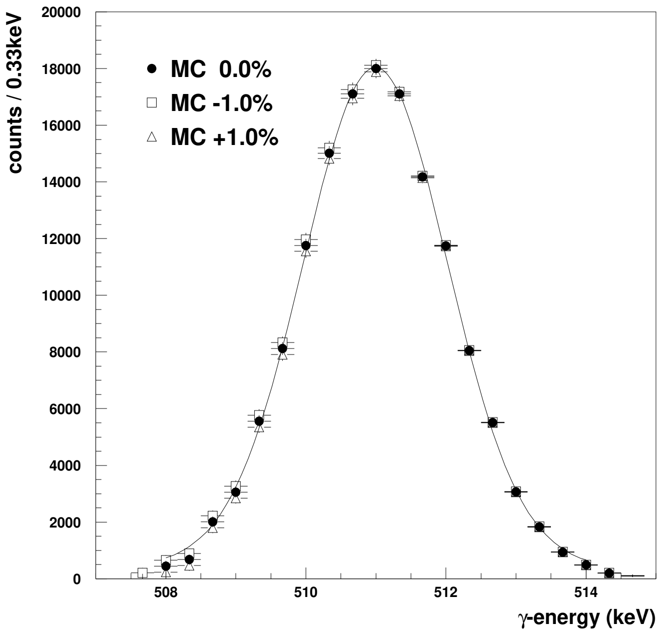

Figure 4.41: The pick-off spectra of RUN II which are extracted with different normalization factors. The meaning of markers are same as in Fig. 4.40.

this assessment is guaranteed within the level of $\pm 0.35\%$ for RUN I and $\pm 0.40\%$ for RUN II. For RUN II the slope is more gentle rather than RUN I, because the pick-off ratio for RUN II is larger compared with that of RUN I and ξ-parameters are less sensitive to the variation of normalization factor.

These variations ($\pm 0.35\%$ for RUN I, $\pm 0.40\%$ for RUN II) can affect the final result by -99 *ppm* $\sim +99$ *ppm* for RUN I and by -113 *ppm* $\sim$ 113 *ppm* for RUN II. These values are assigned as a systematic error for Monte Carlo simulation dependence.

– Relative efficiency of the NaI(Tl) scintillators

The relative efficiency $\varepsilon_{pick}/\varepsilon_{3\gamma}$ of the NaI(Tl) scintillator in Eq. (4.15) is estimated with the Monte Carlo simulation. It can reproduce the spectrum with an uncertainty of 2% as in Appendix B.1.2. However it underestimates the Compton free region, that is $370-440$ keV, by 5%. Then the systematic error is estimated with +5% deviated $\varepsilon_{pick}/\varepsilon_{3\gamma}$. +7 *ppm* deviations are observed for both RUN I and RUN II.

– Inhomogeneity of the SiO_2 powder

The SiO_2 powder is expected to be uniformed within a few %-level. Conservatively, the density of the SiO_2 powder is changed by $\pm 10\%$ in Monte Carlo simulation, which results in a $\pm$ 0.4% change in $\mathcal{F}$ factor. The shifts from these deviations are maximumly ± 55 *ppm* for RUN I and ± 88 *ppm* for RUN II.

4.4.4 Other sources of systematic errors

The Zeeman effect

In the presence of a uniform magnetic field, B ($Gauss$), one of the o-Ps states is perturbed. The decay rate of a perturbed o-Ps state is estimated as [33],

$$\lambda'_{\text{o-Ps}} = \lambda_{\text{o-Ps}} \left(1 + \frac{\eta^2}{4} \frac{\lambda_{\text{p-Ps}}}{\lambda_{\text{o-Ps}}} \right), \tag{4.25}$$

where $\eta = 2\mu_B g B/\hbar\omega = B/36.287$ ($kGauss$) and above expression is valid in the condition, $\eta \ll 1$. As in Sec. 3.2.3 the absolute magnetic field is measured around the positronium formation assembly. With $B = 0.5$, the measured decay rate can be larger than true value by 5 *ppm*. Therefore -5 *ppm* is assigned for this effect.

Three-photon annihilation of an electron-positron pair

The three-photon pick-off process can occur with a certain relative ratio to the two-photon process. With a simple calculation, their relative frequency

$\sigma_{3\gamma}/\sigma_{2\gamma}$ can be estimated from the $(2\gamma/3\gamma)$ decay rate ratio,

$$\sigma_{3\gamma}/\sigma_{2\gamma} = \frac{7.03996 \times 3}{7990.6 \times 1} \sim 1/378. \tag{4.26}$$

The factor 3 in numerator reflects the fact that the probabilities of making parallel or anti-parallel spin combinations are equal in this case. Above value can become further small, because the relative strength of the pick-off frequency of the o-Ps can be smaller than that of the p-Ps. Experimentally the ratio is measured as [74], $\sigma_{3\gamma}/\sigma_{2\gamma} = 1/(3.3 \pm 0.7 \times 10^2)$, which is consistent with the above calculation.

The measured $\lambda_{3\gamma}$ could be maximumly 26(42) *ppm* smaller than the true value for RUN I(II).

The Stark effect

As will be mentioned in Appendix A.1, the electric field on the grain surface of the SiO_2 powder can stretch the lifetime of the Ps atoms. These contributions from the Stark shift are estimated with simple models which are based on the peculiar powder characteristics. For RUN I, typically −21 ppm contribution is expected, while −6 ppm is expected for RUN II. See Appendix A.1 for detail discussions.

Excited state of Ps

Probability that the excited state (n=2) of Ps is produced is about 3×10^{-4} [75] and a half of the excited state have a low decay rate of $\frac{1}{8}\lambda_{3\gamma}$. Due to this low decay rate component, the measured $\lambda_{3\gamma}$ could be 19 *ppm* smaller than the true value.

Above systematic errors are considered to be independent with each other, thus the total systematic is calculated as a quadratic sum of them. These systematic effects are summarized in Table 4.13.

Source of the Contributions	For RUN I (ppm)	For RUN II (ppm)
TDC module dependence		
– Calibration	< 1	< 1
– Stability	$2 \sim 3$	$2 \sim 3$
– Integral Non Linearity	< 15	< 15
– Differential Non Linearity	Negligible	Negligible
Cut condition dependence		
– Energy Selection	not assigned	not assigned
– Base Line Selection	-17 and $+89$	-11 and $+23$
– WD-NW condition	-6 and $+45$	-20
– Trigger threshold	not assigned	not assigned
Monte Carlo dependence		
– Normalization	± 99	± 113
– Relative efficiency of NaI(Tl) scintillator	$+7$	$+7$
– Inhomogeneity of SiO_2 powder	$< \pm 55$	$< \pm 88$
Other Sources		
– Zeeman effect	-5	-5
– Three-photon annihilation	-26	-42
– Stark effect	-21	-6
– $n = 2$ excited state	$+19$	$+19$
Total	-120 and $+153$	-151 and $+148$

Table 4.13: Summary of the systematic errors

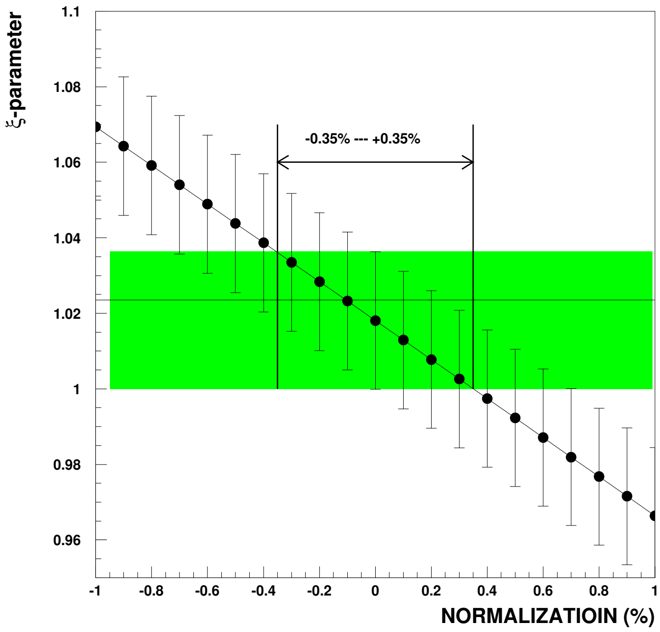

Figure 4.42: The ξ_{asym}-parameters for RUN I are plotted as a function of the deviation from the optimal noramlization. The horizontal band represents a 1σ error region at 0.0%.

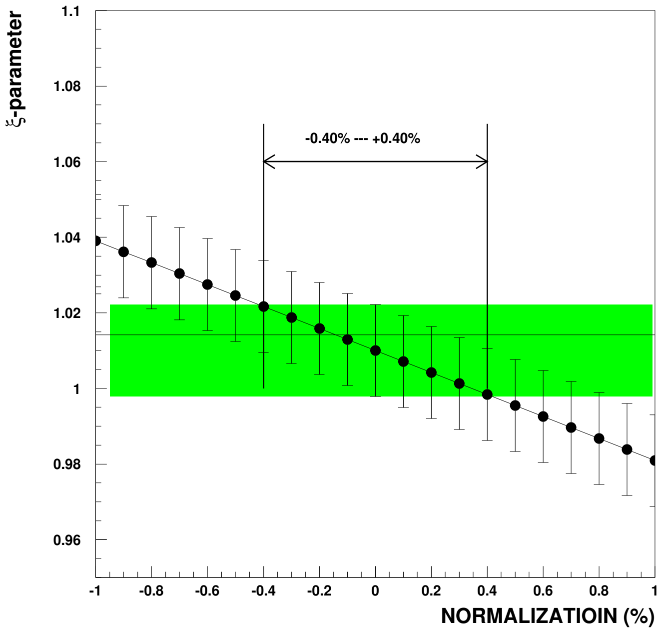

Figure 4.43: The ξ_{asym}-parameters for RUN II are plotted as a function of the deviation of normalization factor.

Chapter 5

Conclusions

5.1 Final Results

To summarize the results from the previous chapter, the following o-Ps decay rates are obtained for two runs,
for RUN I,

$$\lambda_{\text{o-Ps}}(\text{RUN I}) = 7.03991 \pm 0.0017(stat.)^{+0.0011}_{-0.0008}(sys.)\ \mu s^{-1}, \tag{5.1}$$

and for RUN II,

$$\lambda_{\text{o-Ps}}(\text{RUN II}) = 7.03935 \pm 0.0017(stat.)^{+0.0010}_{-0.0011}(sys.)\ \mu s^{-1}. \tag{5.2}$$

where the first error represents a statistic error, and the second one is for systematic.

The final result for the measurement of the o-Ps decay rate is obtained by combining the results from the two runs for different powders. The weighted average value with respect to the error is:

$$\underline{\lambda_{\text{o-Ps}} = 7.0396 \pm 0.0012(stat.) \pm 0.0011(sys.)\ \mu s^{-1}.} \tag{5.3}$$

This result is <u>1.8 times more precise</u> than that of the previous measurement [7] which utilizes the SiO_2 powder, and this total error of about 230 ppm enables us to discuss the non-logarithmic α^2 correction on the o-Ps decay rate.

The decay rates are obtained independently of the fitting start time, from $t_{start} = 90(80)$ ns for RUN I(II). The origin of systematic increasing before $t_{start} = 200$ ns observed in the previous measurement is now understood and solved; this phenomena restricted the statistical precision in the last measurement.

These values are obtained independently with two types of SiO_2 powder which show quite different features as to the thermalization of o-Ps; this can be clearly seen in Fig. 5.1. In spite of this large difference in correction,

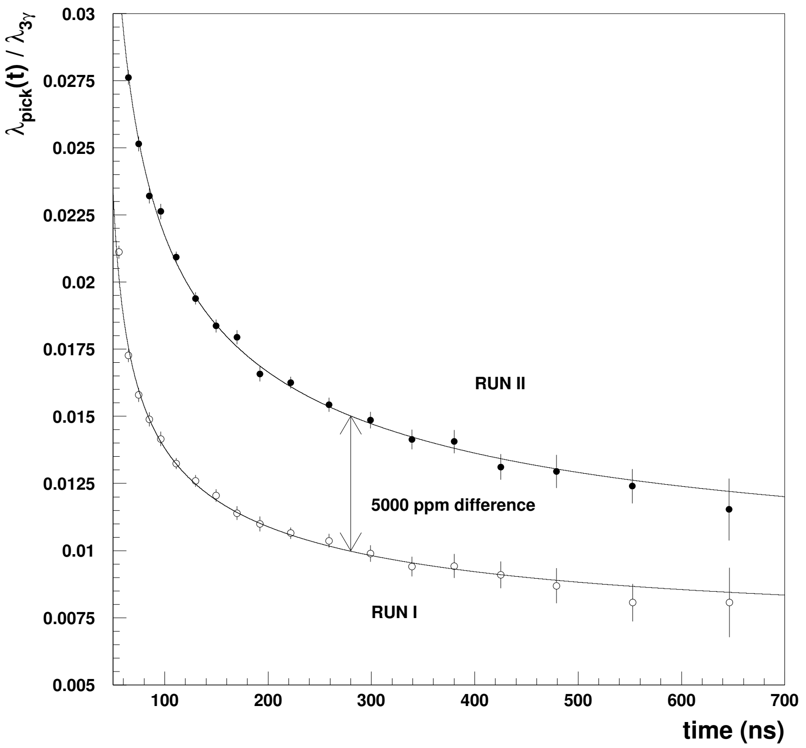

Figure 5.1: A comparison of $\lambda_{pick}/\lambda_{3\gamma}$ ratio curves for two different powders. Open and close circles represent the curves for RUN I and RUN II respectively. As indicated in the figure, the average difference between the two curves, i.e. the correction magnitudes are about 5000 ppm. It is important to note that the error propagated from $\lambda_{pick}(t)$ to $\lambda_{3\gamma}$ is suppressed, because the ratio $\lambda_{pick}(t)/\lambda_{3\gamma}$ is a small value of about 0.01.

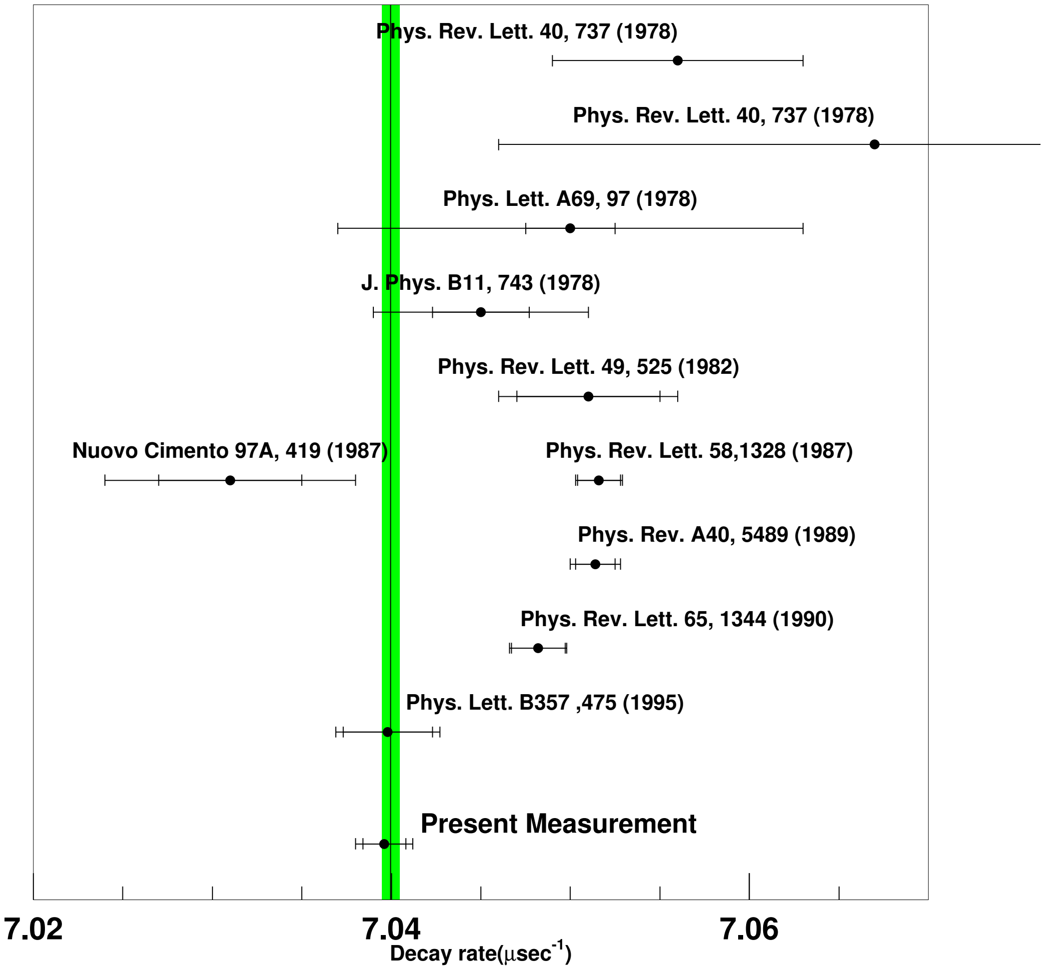

Figure 5.2: The history of the o-Ps decay rate measurements including the present measurement. Vertical band represents the $O(\alpha^2)$-corrected NRQED prediction of 7.039 960 μs^{-1}. The uncertainty width of ± 70 ppm is assigned. The small line at the inside of an each error bar represents a error solely due to statistics.

above results show a excellent agreement between the runs.

As illustrated in Fig. 5.2, the current result agrees well with the NRQED prediction corrected up to an $O(\alpha^2)$ term. The result agrees well with the previous measurement [7], while disagrees with the other recent high precision measurements by 5.6 σ [5] and 3.8 σ [6] respectively.

5.2 Theoretical Implications

By comparing the obtained result with the values in Table 2.4, the result agrees with the QED prediction within a 1σ level regardless of B_o presence.

Nevertheless, as in Fig. 5.3, the result differs from the $O(\alpha^2)$ corrected QED prediction by 0.23 σ while differs from $O(\alpha)$ corrected value by 0.86 σ.

Therefore one can conclude that this is the first measurement that catches the indication from the two-loop effect of o-Ps decay. The measured value favors the $O(\alpha^2)$ corrected QED value rather than that of $O(\alpha)$ correction.

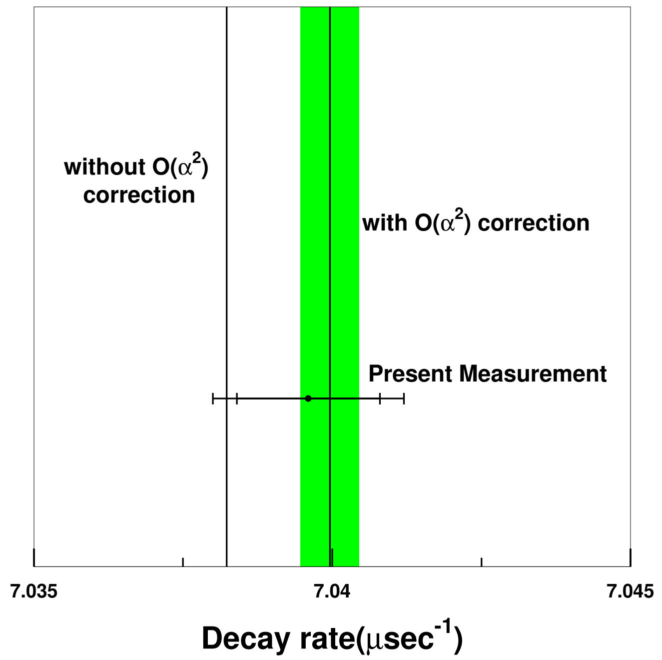

Figure 5.3: The relation between the present result and the theoretical prediction. The right vertical line shows the $O(\alpha^2)$-corrected NRQED prediction of 7.039 960 μs^{-1} with ± 70 ppm uncertainty. The left vertical line represents the QED prediction with $B_o = 0$, that is 7.038 228 μs^{-1}.

Appendix A

A.1 Stark Shifts

In this appendix the influence of the oxide powder environment on the o-Ps decay rate is discussed. This effect was concerned in 1976 when the decay rate was measured by 2% level. In that level of accuracy, as a conclusion of reference [76], the Stark effect could play no role because they were estimated to be considerably small. However when it comes to a case of 200 *ppm* measurement, they cannot be simply ignored from the beginning.

A.1.1 Stark Effects on o-Ps Decay Rate

In the lowest order calculation of decay rate $\lambda_o^{(0)}$ in Eq. (2.5), the contribution of α^3 originate from a flux factor representing the probability of overlapping between the wave-functions of electron and positron at the origin in the center-of-mass frame. Thus the decay rate of o-Ps is proportional to the Ps wave-function at the origin, i.e.,

$$\lambda_{3\gamma} \propto \text{Flux Factor} \propto |\phi(r=0)|^2. \tag{A.1}$$

If a uniform electric field E is applied to the Ps, here the absolute value of this field is assumed to be not too large as to excite or to ionize the Ps, the wave function of the Ps, ψ, is perturbed to be,

$$\psi = \psi_0 + E\psi_1 + E^2\psi_2 + \cdots, \tag{A.2}$$

where ψ_0 is the unperturbed ground state wave function, and $\psi_1, \psi_2, \cdots$ stand for the higher order perturbed terms. Simple calculation by the perturbation method shows the relative shift of the decay rate as a function of E [76, 77, 78],

$$\begin{aligned} \frac{\triangle\lambda_{3\gamma}}{\lambda_{3\gamma}} &= E^2\frac{|\psi_1|^2}{|\psi_0|^2} && \text{(A.3)} \\ &= 248\cdot(E/E_0)^2, && \text{(A.4)} \end{aligned}$$

where $E_0 = m_e^2 e^5/\hbar^4 \approx 5.14 \times 10^9\ V/cm$. In these expressions, the field E should be interpreted as the root-mean-square electric field sensed by Ps during the period of its existence.

A.1.2 Assessment of the Charge Up on Primary Grains.

In the first place, let us consider the situation where the primary grain of the SiO_2 powder is charged up and makes the electric field on its surface.

The quantity of electric charge for manufactured SiO_2 product is well known. Nominal value for Powder I (300CF) is about $-500\ \mu C/g$, and for Powder II (R812) it amounts to about $-400\ \mu C/g$ [59].

Of course, positron deposition on the powder grain from the ^{22}Na β^+ source must be taken into account; although we adopt the very weak source, the accumulation among the long term measurement of about six-month cannot be ignored from the first place. Here we assume that the ^{22}Na source with the strength about 0.03 μCi is used during six-month, the positron can penetrate 2-mm thick into the powders (equivalent to 7.4×10^{-2} [g]). Then we can estimate an average amount of the charge accumulation on the powder grain as,

$$\begin{aligned} & \text{Accumulation of } e^+ \\ = \;& e \times\ 0.03 \times 3.7 \times 10^4 \ [\ s^{-1}\ ] \ \times\ 3600 \times 24 \times 180 \ [\ s\ ] \ /\ 7.4 \times 10^{-2} \ [\ g\ ] \\ = \;& 3.7 \times 10^{-2} \ [\ \mu C/g\ ] \qquad \text{(A.5)} \end{aligned}$$

This value is sufficiently small compared with the intrinsic charge-up values described above.

Provided that the primary grains are the sphere of 7 nm-diameter, and are made up from the pure SiO_2, the mass of a grain will be,

$$m_{grain} = 2.20\ [\ g/cm^3\ ] \times \frac{3}{4}\ \pi r^3 \sim 4.0 \times 10^{-19}\ [\ g\ ]. \qquad \text{(A.6)}$$

Thus the charge accumulation on a one grain is estimated to be,

$$\begin{aligned} C_{grain} &= -500(-400) \times 10^{-6}\ [\ C/g\ ] \times 4.0 \times 10^{-19}\ [\ g\ ] \\ &\simeq 2(1.6) \times 10^{-22}\ [\ C\ ] \\ &\simeq 1.3(1.0) \times 10^{-3}\ [\ electron\ ] \qquad \text{(A.7)} \end{aligned}$$

for the powder I(II); inversely, in average the one electron exists per about 770(1000) powder grains. If one assumes the powder grains uniformly spread over the volume, the volume per one grain L'^3 can be estimated as,

$$\begin{aligned} L'^3 &= \frac{4}{3}\pi r^3 \times 2.2\ [\ g/cc\ ]\ /\ 0.03\ [\ g/cc\ ] \\ &= 310\ r^3 \quad [\ r = 3.5\ nm\ ]. \qquad \text{(A.8)} \end{aligned}$$

Then one can estimate the volume L^3 which the one electron can possess in average as, $L^3 = 770(1000) \times L'^3 = 100(130) \times 10^5$ [nm^3].

If the distance between the Ps and the electron is x, the square of the electric field at the position of Ps would be,

$$
\begin{aligned}
|E|^2 &= \left(\frac{e}{4\pi\varepsilon_0 x^2}\right)^2 \\
&= \frac{\tilde{e}^2}{x^4} \quad \left[\, \tilde{e} = 1.4 \times 10^{-9}\ [V \cdot m\,] \right].
\end{aligned} \tag{A.9}
$$

Since the Ps is freely traveling around the whole space between the grains, the average field sensed by the Ps should be estimated by averaging over the whole volume as,

$$
\begin{aligned}
\overline{|E|^2} &= \int dV |E|^2 / L^3 \\
&= 4\pi \int_{\varepsilon}^{L} dx x^2 \frac{\tilde{e}^2}{x^4} / L^3 \\
&\simeq \frac{4\pi\tilde{e}^2}{\varepsilon L^3},
\end{aligned} \tag{A.10}
$$

where ε is a minimum distance the Ps can get close to the electron. Bohr radius of the Ps $r_{Ps} = 1.1 \times 10^{-10}$ [m] (twice the Bohr radius of atomic hydrogen) is quite a good approximation value for ε since the value estimated from the e^--Ps elastic scattering cross section is about $r = 7.7 \times 10^{-10}$ [m], and from the ortho-para conversion cross section, the value would be $r_c = 1.9 \times 10^{-10}$ [m] [79, 80].

Thus an average of the squared electric field would be, $\overline{|E|^2} = 2.2 \times 10^{13}$ [V^2/m^2]; from Eq. (A.4) this could contribute to the decay rate, by a 2.1×10^{-2} ppm level. Clearly we can neglect this quantity.

A.1.3 Contribution of Dipole Moment on the Surface of Powder Grain

SiO_2 powder has mainly two types of functional groups, i.e. silanol groups ($-$Si (OH)) and siloxan groups ($-$Si (O) Si$-$). The hydrophilia of the powder is attributed to this silanol groups, and this groups are substituted with certain functional groups such as, the tri-methyl-silyl groups, the dimethyl-silyl groups, etc. in order to obtain the hydrophobe character.

The average density of the silanol groups on the surface of grains are investigated, and are yielding 2.5 $/nm^2$ and 0.44 $/nm^2$ for powder types of $300CF$ and $R812$ respectively [59]. Figure A.1 shows the schematic diagram of one SiO_2 grain. The silanol groups are existing on the surface of the grain. A typical size of dipole moment for the groups $-$(OH) is $1.7 \times 10^{-18} [esu \cdot cm]$ [81].

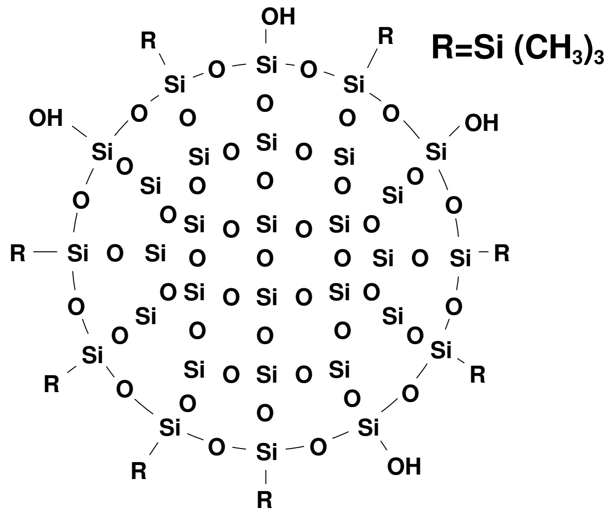

Figure A.1: Schematic diagram of SiO_2 grain. Part of the surface functional groups are substituted, while there are still silanol groups left.

Since we are assuming a simple model and respecting the symmetry, it is not going too far if one assumes the dipole moment is directed outward on the surface of the grain as a vector $\boldsymbol{p}$ in Fig. A.2

For a simplicity, now let us assume a dipole moment $\vec{p}$ on the surface of grain, then the electric field at the point O outside the grain as in Fig. A.2 is expressed as,

$$\vec{E} = \frac{1}{4\pi\varepsilon_0} \cdot \frac{3\ (\vec{n}\cdot\vec{p})\cdot\vec{n} - \vec{p}}{R_0^3}, \tag{A.11}$$

where some variables r, R, R_0, $\vec{p}$, $\vec{n}$, α and θ are defined as in the figure. Then the squared electric field would be,

$$\begin{aligned} |E|^2 &= \frac{p^2}{R_0^6}\left(3\cos^2\alpha + 1\right) \\ &= \cdots \\ &= \frac{p^2}{R_0^8}\left(R_0^2 + 3\,(r - R\cos\theta)^2\right), \end{aligned} \tag{A.12}$$

defining the area density of the silanol-group as σ and integrating on the surface of one grain, the squared electric field at the position O would be,

$$\begin{aligned} |E|_o^2 &= 2\pi\sigma r^2 \int_0^\pi \sin\theta d\theta |E|^2 \\ &= 2\pi\sigma r^2 p^2 \int_{-1}^1 dx \left(\frac{1}{R_0^6} + 3\frac{(r+Rx)^2}{R_0^8}\right) \\ &\qquad \text{(substituted } x \text{ as } x = -\cos\theta). \end{aligned} \tag{A.13}$$

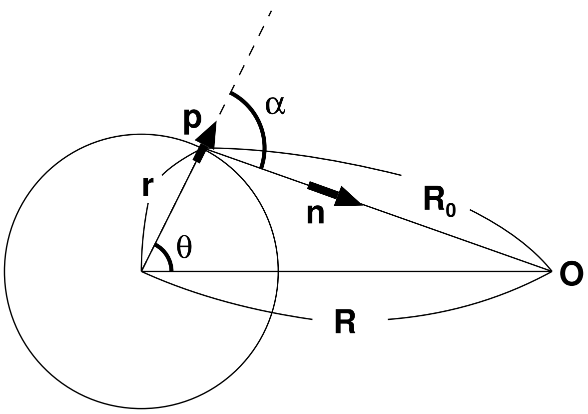

Figure A.2: A definition of the variables used for calculation in the context. $\vec{n}$ is a unit vector directing from dipole moment $\vec{p}$ to the observe point O.

Lengthy but simple calculation yields the final form as,

$$\begin{aligned} |E|_o^2 &= \pi\sigma p^2 \frac{r}{R}\left(\frac{3}{2}\left(\frac{1}{(R-r)^4} - \frac{1}{(R+r)^4}\right) - \frac{1}{2r}\left(\frac{1}{(R-r)^3} - \frac{1}{(R+r)^3}\right)\right. \\ &\quad \left. + \frac{1}{4Rr}\left(\frac{1}{(R-r)^2} - \frac{1}{(R+r)^2}\right)\right). \qquad \text{(A.14)} \end{aligned}$$

As in the previous section, the Ps is assumed to be freely travelling between the grains. However in this case, the Ps is moving between the grains (average distance is calculated as a mean free path between the grains, $\overline{L}$; this length has been already obtained as in Table 3.1), continuing to collide with the grains. Thus the integration is carried out in one dimension from the nearest distance to the powder ε (again the Bohr radius of Ps is used as ε), to the mean distance between the grains $\overline{L}$.

In integrating Eq. (A.14) with variable R ($r + \varepsilon \leq R \leq \overline{L}$), Almost all contribution comes from the first term of Eq. (A.14) as R approaches to $r + \varepsilon$, thus if one neglects the other terms and integrates over the defined range, the average squared electric field would be,

$$\begin{aligned} \overline{|E|_o^2} &= \int_{r+\varepsilon}^{\overline{L}} dR |E|_o^2 \,/\, \overline{L} \\ &= \frac{3\pi\sigma p^2 r}{2\overline{L}} \int_{r+\varepsilon}^{\overline{L}} dx \frac{1}{x(x-r)^4} \\ &\simeq \frac{3\pi\sigma p^2 r}{2\overline{L}} \cdot \frac{1}{r}\left[\frac{1}{-3(x-r)^3}\right]_{r+\varepsilon}^{\overline{L}} \\ &\simeq \frac{\pi\sigma p^2}{2\overline{L}\varepsilon^3}. \qquad \text{(A.15)} \end{aligned}$$

For powder I (300CF) the following values are substituted into Eq. (A.15); the area density of the silanol-group, $\sigma = 2.5\ [nm^{-2}]$, the dipole moment of -OH group, $p = 1.7 \times 10^{-18}\ [esu \cdot cm] = 0.050\ [V \cdot nm^2]$, the mean distance of the grains, $\overline{L} = 340\ [nm]$, the minimum distance between the grain and the Ps, $1.1 \times 10^{-1}\ [nm]$.

Yielding, $\overline{|E|_o^2} = 2.2 \times 10^{16}\ [V^2/m^2]$, and with Eq. (A.4) one can estimate the contribution of Stark shift to the decay rate; for powder I, it would be $\underline{21\ ppm}$.

The same calculation could be applied for powder II. In this case, values for the two variables are changed, i.e. $\sigma = 0.44\ [nm^{-2}]$, $\overline{L} = 200\ [nm]$, resulting, $\overline{|E|_o^2} = 6.5 \times 10^{15}\ [V^2/m^2]$ that is $\underline{6.2\ ppm}$ contribution to the decay rate of o-Ps.

A.1.4 Comparison of the Result with the Measurement

An independent evidence concerning the size of electric fields comes from a measurement of the HFS (hyper-fine-structure) interval, $\triangle\nu$, in the ground state of positronium in SiO_2 powder.

Since the HFS interval is, like the decay rate, proportional to the square of the wave function at the origin. Hence the relative Stark shift of $\triangle\nu$ should be same as that of the decay rate.

Observed relative shifts [82] in 1976 are summarized in Table A.1. The value $\triangle\nu$ for free Ps is taken from the recent theoretical result [1]: $\triangle\nu(Ps) = 203.392\ 01(46)\ GHz$.

Sample	Density of pellet (g/cm^3)	Mean radius (nm)	Measured $\triangle\nu$ (GHz)	Relative shift (ppm)
SiO_2(380)	0.51(5)	3.5	203.268(15)	610
SiO_2(300)	0.51(5)	3.5	203.235(15)	770
SiO_2(130)	0.51(5)	8.0	203.313(17)	390

Table A.1: Summary of the HFS measurement. The values are quoted from the Ref. [82], where the values of relative shift are modified by updating $\triangle\nu$ value by the recent calculation [1].

It is important to note that the density of the powder is much larger than the current measurement, as they pressed the sample into cylindrical pellets. Since the mean distance of the grains, $\overline{L}$ is inversely proportional to the density of the powder as in Eq. (3.10), the size of Stark shift must scale according to the density of the sample.

Fortunately the samples in their measurements are supplied by Degussa Inc.; The samples have basically the same characteristics with the ones from

Nippon Aerosil Ltd., the figures needed to calculate the Eq. (A.15) is thus well known. Hence one can perform the same calculation as in the previous section. The result is 300 *ppm* for SiO_2 (380), indicating the evaluation was quite a success to be within a factor of 2 (see the last column of Table A.1).

As in the reference [82], the significant decrease of the shift for SiO_2 (130) is due to its small specific surface area; the size is denoted in the parenthesis, i.e. for SiO_2 (130) the surface area per gram is 130 $[m^2 g^{-1}]$, which effectively renders the mean distance $\overline{L}$ longer and yields rather small Stark shift.

Appendix B

B.1 Evaluating the Reliability of the Monte Carlo Simulation

In this appendix, the validity of the Monte Carlo simulation for o-Ps used in this thesis is examined (from now on this original simulation will be referred to as MC-o).

As illustrated in Sec. 3.3, the MC-o has been developed to handle only γ-ray energy information. Thus different from the general purpose low-energy simulation package such as EGS4 code system [83], MC-o has following advantages,

- The geometric information of the experimental setup can easily be implemented. The geometry code for EGS4 is much intricate and it is almost impossible to describe the code for some peculiar shape or complicated structure with EGS4.
- Regardless to say, MC-o is much faster.
- Not only the user-code geometry part but also the particle interaction part can be managed by user.

It is strongly desired to verify the validity or correctness of the MC-o by comparing with well-established simulation code such as EGS4.

B.1.1 Comparing the Ge Energy Response with the EGS4

Since it is hard to implement a complicated setup geoemetry for EGS4, the comparison is carried out by assuming a simple setup, that is,

- Isotropic point source, assuming ^{85}Sr that emits monochromatic 514 keV γ-ray, is placed 10.0 cm away from the detector. This radioactive source has been chosen because the shape and the energy scale of the Compton spectrum of this monochromatic γ-ray source is almost same with that of the ^{22}Na.

- One germanium detector is placed right in front of the source. The germanium detector has the same geometry as in Fig. 3.4 and equipped with the 2.0 mm-thick lead sheet in front.

The energy response distributions from both simulation (MC-o, EGS4) are normalized by the number of photoelectric peak events at 514 keV. The Compton scattered spectra are compared at the energy range of 100–510 keV.

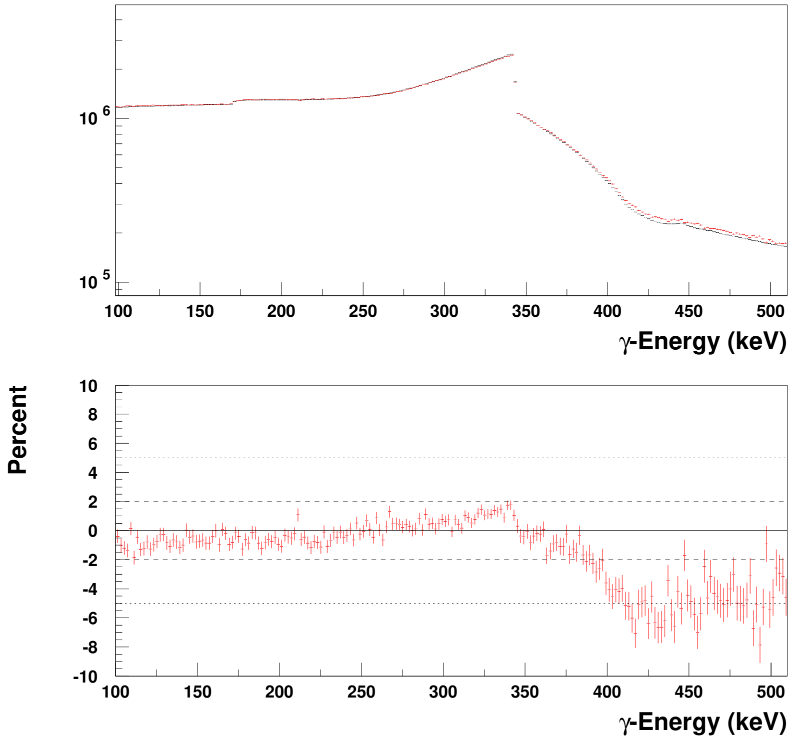

Figure B.1: The comparison of the two simulations for the Ge energy response. (a) Logarithmic plot of the energy spectrum for MC-o and EGS4. (b) $(N_{\text{MC-o}} - N_{\text{EGS4}})/N_{\text{MC-o}}$ is plotted against the energy, where $N_{\text{MC-o}}$ and N_{EGS4} are event contents inside each bin generated by MC-o and EGS4 respectively.

Figure B.1 (a) is the logarithmic plot of the two spectra showing a good agreement between them. Figure B.1 (b) shows the relative difference divided by the contents of MC-o spectrum. As can be seen from the figure, the MC-o and EGS4 give a good accordance below 370 keV within 2% level, while showing a disagreement over 380 keV region by 5% level.

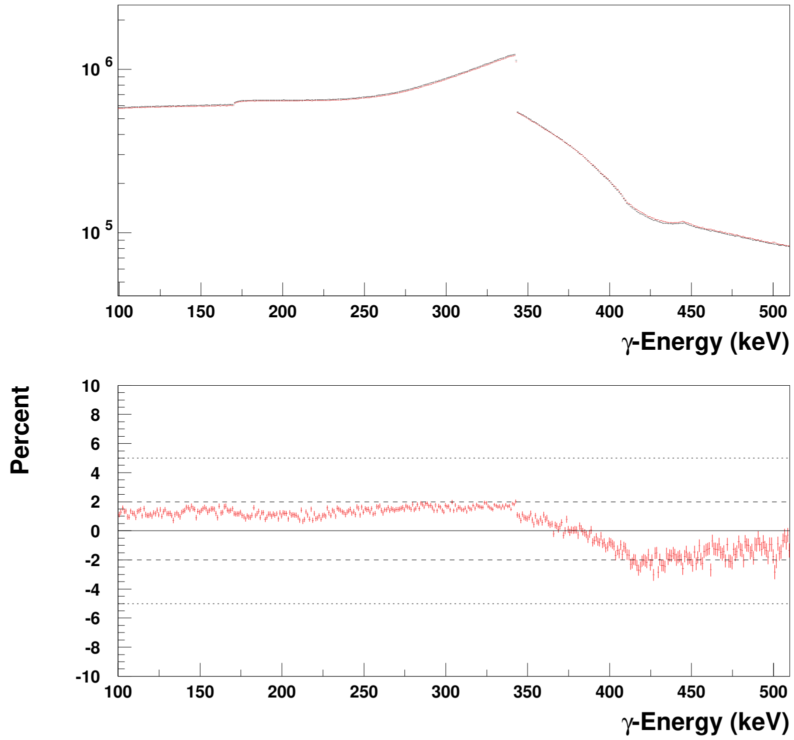

Figure B.2: The comparison of the two simulations for the Ge energy response. The same plots as Fig. B.1 except the Compton scattered electrons are stopped immediately after their appearance.

This diminution of the events at the multi-Compton region is conjectured as *not the reduction of MC-o but the increase of EGS4*. This can be understood as follows,

Since the transfer of the Compton scattered electrons or photo-electrons has not been implemented in MC-o, it is assumed that the electron deposit all of its energy at the interaction point. This assumption is a good approximation as far as the components of detector are enough size. But note that the inactive volume of germanium detector is thin layer of 700-μm. The photo electron can move into a adjacent active-germanium region and deposit part of its energy on the active region. This phenomenon is taken into account in EGS4, thus the excess counts at the multi-Compton region is conjectured to be due to this phenomenon.

Above inference can be ascertained by modifying the EGS4 optional parameters. The parameter *ECUT*, then defines the cut-off energy of the electrons; if the energy of electron becomes smaller than *ECUT* all kinetic energy of the electron is treated as energy deposition at the point. Therefore by defining $ECUT = 600$ keV, the electrons are bound to deposit all of its energy at the interaction point.

Figure B.2 shows the result of the modification. Now that outputs from the MC-o and the EGS4 give a quite good agreement over the all energy region within 2% level. Thus one can conclude the distinction in Fig. B.1 is attributed to the difference in treatment of electron transfer.

Considering that the table of absorb coefficients for each interaction are provided in the form of coefficients (logarithmic) – energy (logarithmic), this 2%-level agreement represents the validity of the MC-o.

The uncertainty of the MC-o for Ge energy response is estimated to be within 2% for Compton scattering event below 370 keV, while 5% deviation is assigned for multi-Compton region.

B.1.2 Comparing the NaI(Tl) Energy Response with the EGS4

In the same way as the last section, the comparisons as to the NaI(Tl) case are carried out. The assumed common setup is,

- The monochromatic γ-ray source (514.0 keV) is placed in front of a NaI(Tl) scintillator. The distance between them is 10.0 cm.
- The same geometry and materials but the optical window and the PMT part as in the Fig. 3.7 are used in the simulations.

As in the Ge case, the energy response distributions from both simulations (MC-o, EGS4) are normalized by the number of count ratio at 514.0 keV. As in Fig. B.3, a good agreement between the two distributions can be seen in the energy range, 200 – 340 keV. At the range of interest, 370 – 440 keV, that is in the multi-Compton region, they showed a agreement within the 5% level. The difference shows a similar behavior as in the Ge case, which may be attributed to the same reason, that is, the electrons which is scattered off from the Al cover in front (about 800 μm) deposit their energy on NaI(Tl) region at last.

This assumption can be verified by defining $ECUT = 600$ keV as in the Ge energy response study. Figure B.4 represents the comparison of two distributions after the $ECUT$ definition.

The uncertainty of the MC-o for NaI(Tl) scintillator energy response is estimated to be within about 2% below 340 keV. In the multi-Compton region, it is estimated to be 5% deviation.

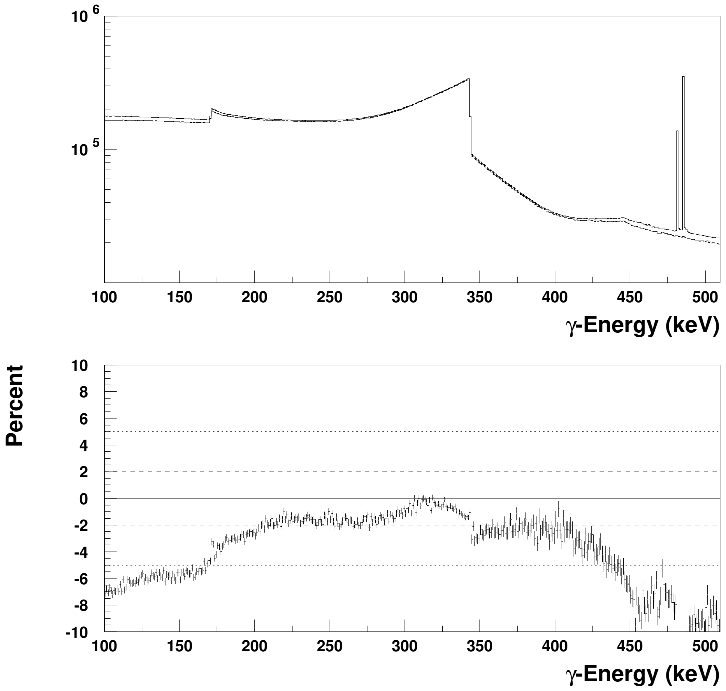

Figure B.3: The comparison of the two simulations for the NaI(Tl) energy response. (a) Logarithmic plot of the energy spectrum for MC-o and EGS4. (b) $(N_{\text{MC-o}} - N_{\text{EGS4}})/N_{\text{MC-o}}$ is plotted against the energy.

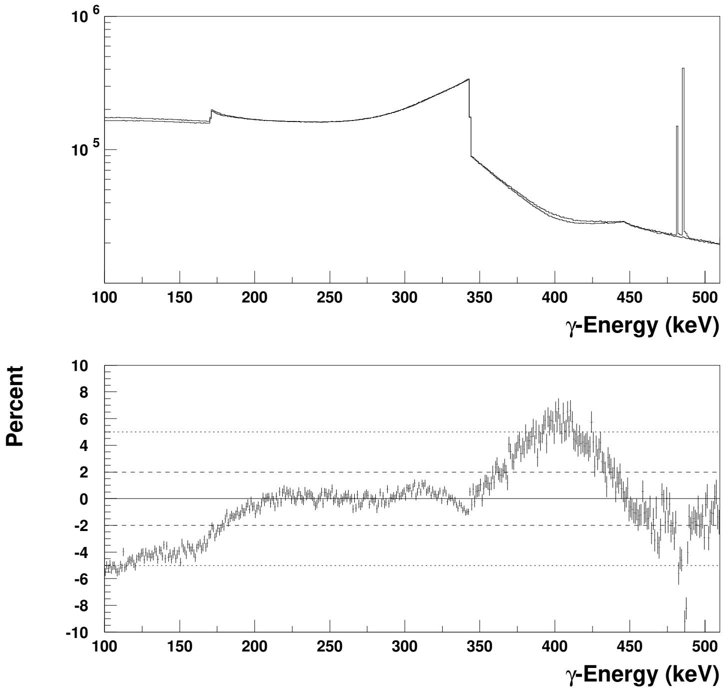

Figure B.4: The comparison of the two simulations for the NaI(Tl) energy response. Compton scattered electrons are stopped immediately after their appearance.

Bibliography

[1] A. Czarnecki, K. Melnikov, and A. Yelkhovsky, Phys. Rev. A **59**, 4316 (1999).

[2] A. H. Al-Ramadhan and D. W. Gidley, Phys. Rev. Lett. **72**, 1632 (1994).

[3] A. Czarnecki, K. Melnikov, and A. Yelkhovsky, Phys. Rev. Lett. **83**, 1135 (1999).

[4] G. S. Adkins, R. N. Fell, and J. Sapirstein, Phys. Rev. Lett. **84**, 5086 (2000).

[5] C. I. Westbrook, D. W. Gidley, R. S. Conti, and A. Rich, Phys. Rev. **A40**, 5489 (1989).

[6] J. S. Nico, D. W. Gidley, A. Rich, and P. W. Zitzewitz, Phys. Rev. Lett. **65**, 1344 (1990).

[7] S. Asai, S. Orito, and N. Shinohara, Phys. Lett. **B357**, 475 (1995).

[8] G. S. Adkins and F. R. Brown, Phys. Rev. A **28**, 1164 (1983).

[9] T. Matsumoto, M. Chiba, R. Hamatsu, and T. Hirose, Phys. Lett. A **54**, 1947 (1996).

[10] A. Öre and J. L. Powell, Phys. Rev. **75**, 1696 (1949).

[11] W. E. Caswell, G. P. Lepage, and J. Sapirstein, Phys. Rev. Lett. **38**, 488 (1977).

[12] G. S. Adkins, Ann. Phys. (NY) **146**, 78 (1983).

[13] C. itzykson and J. Zuber, *Quantum Field Theory*, McGeaw-Hill, 1986.

[14] G. S. Adkins, Phys. Rev. Lett. **76**, 4903 (1996).

[15] W. E. Caswell, G. P. Lepage, and J. Sapirstein, Phys. Rev. Lett. **38**, 488 (1977).

[16] G. S. Adkins, Ann. Phys. (NY) 146 , 78 (1983).

[17] G. S. Adkins, A. A. Salahuddin, and K. E. Schalm, Phys. Rev. A **45**, 7774 (1992).

[18] I. Harris and L. M. Brown, Phys. Rev. **105**, 1656 (1957).

[19] W. E. Caswell and G. P. Lepage, Phys. Rev. A **20**, 36 (1979).

[20] I. B. Khriplovich and A. S. Yelkhovsky, Phys. Lett. B **246**, 520 (1990).

[21] A. I. Milstein and I. B. Khriplovich, JTEP **79**, 379 (1994).

[22] S. G. Karshenboim, JTEP **76**, 541 (1993).

[23] S. G. Karshenboim, Phys. At. Nucl. **1710**, 1993 (1993).

[24] B. A. Kniehl and A. A. Penin, hep-ph/0004267, 2000.

[25] K. Melnikov and A. Yelkhovsky, hep-ph/0008099, 2000.

[26] A. P. Burichenko, Phys. At. Nucl. **56**, 640 (1993).

[27] P. Labelle, G. P. Lepage, and U. Magnea, Phys. Rev. Lett. **72**, 2006 (1994).

[28] R. N. Faustov, A. P. Martynenko, and V. A. Saleev, Phys. Rev. A **51**, 4520 (1995).

[29] A. Czarnecki, K. Melnikov, and A. Yelkhovsky, hep-ph/9910488, 1999.

[30] R. Hill and G. P. Lepage, hep-ph/0003277, 2000.

[31] G. L. Castro, J. Petieau, and C. Smith, hep-ph/0004209, 2000.

[32] S. Asai, *New Measurement of Orthopositronium Lifetime*, Ph. D. thesis, 1995, University of Tokyo.

[33] C. I. Westbrook, *Precision Measurement of the Decay Rate of Ortho-Positronium*, Ph. D. thesis, 1987, University of Michigan.

[34] R. H. Beers and V. W. Hughes, Am. Phys. Soc. **13**, 633 (1968).

[35] D. W. Gidley, K. A. Marko, and A. Rich, Phys. Rev. Lett. **36**, 395 (1976).

[36] D. W. Gidley, P. W. Zitzewitz, K. A. Marko, and A. Rich, Phys. Rev. Lett. **37**, 729 (1976).

[37] D. W. Gidley, A. Rich, P. W. Zitzewitz, and D. A. L. Paul, Phys. Rev. Lett. **40**, 737 (1978).

[38] D. W. Gidley and P. W. Zitzewitz, Phys. Lett. A **69**, 97 (1978).

[39] K. F. Canter et al., Phys. Lett. A **65**, 301 (1978).

[40] T. C. Griffith, G. R. Heyland, K. S. Lines, and T. R. Twomey, J. Phys. B **11**, 743 (1978).

[41] D. W. Gidley, A. Rich, E. Sweetman, and D. West, Phys. Rev. Lett. **49**, 525 (1982).

[42] P. Hashbach, G. Hilkert, E. Klempt, and G. Werth, Nuovo Cimento **97A**, 419 (1987).

[43] C. I. Westbrook, D. W. Gidley, R. S. Conti, and A. Rich, Phys. Rev. Lett. **58**, 1328 (1987).

[44] J. S. Nico, *Precision measurement of the orthopositronium decay rate using the vacuum technique*, Ph. D. thesis, 1991, University of Michigan.

[45] S. Orito, K. Yoshimura, T. Haga, M. Minowa, and M. Tsuchiaki, Phys. Rev. Lett. **63**, 597 (1989).

[46] S. Asai, S. Orito, K. Yoshimura, and T. Haga, Phys. Rev. Lett. **66**, 2440 (1991).

[47] S. Asai, K. Shigekuni, T. Sanuki, and S. Orito, Phys. Lett. B **323**, 90 (1994).

[48] M. Tsuchiaki, S. Orito, T. Yoshida, and M. Minowa, Phys. Lett. B **236**, 81 (1990).

[49] T. Maeno, M. Fujikawa, J. Kataoka, Y. Nishihara, S. Orito, K. Shigekuni, Y. Watanabe, Phys. Lett. B **351**, 574 (1995).

[50] T. Mitsui, K. Maki, S. Asai, Y. Ishisaki, R. Fujimoto, N. Muramoto, T. Sato, Y. Ueda, Y. Yamazaki and S. Orito, Europhys. Lett. **33**, 111 (1996).

[51] T. Mitsui, R. Fujimoto, Y. Ishisaki, Y. Ueda, Y. Yamazaki, S. Asai, and S. Orito, Phys. Rev. Lett. **70**, 2265 (1993).

[52] S. Asai, S. Orito, T. Sanuki, M. Yasuda, and T. Yokoi, Phys. Rev. Lett. **66**, 1298 (1991).

[53] D. W. Gidley, J. S. Nico, and M. Skalsey, Phys. Rev. Lett. **66**, 1302 (1991).

[54] K. Marko and A. Rich, Phys. Rev. Lett. **33**, 980 (1974).

[55] M. Skalsey, J. J. Engbrecht, R. K. Bithell, R. S. Vallery, and D. W. Gidley, Phys. Rev. Lett. **80**, 3727 (1998).

[56] R. S. Vallery, A. E. Leanhardt, M. Skalsey and D. W. Gidley, J. Phys. B: At. Mol. Phys. **33**, 1047 (2000).

[57] Y. Nagashima, T. Hyodo, K. Fujiwara, and A. Ichimura, J. Phys. B **31**, 329 (1998).

[58] Y. Nagashima, M. Kakimoto, T. Hyodo, K. Fujiwara, A. Ichimura, T. Chang, J. Deng, T. Akahane, T. Chiba, K. Suzuki, B. T. A. McKee, and A. T. Stewart, Phys. Rev. A **52**, 258 (1995).

[59] Nippon Aerosil Co. Ltd., The basic characteristics of AEROSIL, Aerosil technical report No.17.

[60] M. Charlton, Rep. Prog. Phys. **48**, 737 (1985).

[61] METROLAB Instruments SA, *THM 7025 3-AXIS HALL MAGNETOMETER User's Manual.*

[62] S. Berko and H.N. Pendleton, Ann. Rev. Nucl. Part. Sci. **30**, 543 (1980).

[63] R. B. Firestone and V. S. Shirley, *Table of Isotopes [8th Edition]*, John Wiley & Sons, Inc., 1999.

[64] EG & G ORTEC, *Principles and Applications of Timing Spectroscopy*, AN-42.

[65] W. R. Leo, *Techniques for Nuclear and Particle Physics Experiments : A How-to Approach, 2nd. rev. ed.*, Springer-Verlag, 1994.

[66] R. Paulin, Proc. 5th Int. Conf. Positron Annihilation, (1979), 601.

[67] G. S. Adkins, private communication.

[68] NIST, Physics Laboratory, Office of Electronic Commerce in Scientific and Engineering Data.

[69] IT/ASD CERN, *GEANT Detector Description and Simulation Tool, version 3.21*, (1993), W5103 CERN Program Library.

[70] M. A. Hammed, P. W. Gray, A. H. Naboulsi and T. D. Mac Mahon, Nucl. Inst. Methods A **334**, 543 (1993).

[71] H. H. Jorch and J. L. Campbell, Nucl. Inst. Methods A **143**, 551 (1977).

[72] IT/ASD CERN, *MINUIT Function Minimization and Error Analysis, version 94.1*, (1998), D506 CERN Program Library.

[73] IT/ASD CERN, *CERN Program Library Short writeups*, (1996).

[74] J. A. Rich, Phys. Rev. **61**, 140 (1951).

[75] S. Hatamian, R. S. Conti, and A. Rich, Phys. Rev. Lett. **58**, 1833 (1987).

[76] G. W. Ford, L. M. Sander, and T. A. Witten, Phys. Rev. Lett. **36**, 1269 (1976).

[77] L. I. Shiff, *Quantum Mechanics*, McGraw-Hill, New York, 1949.

[78] G. L. Sewell, Proc. Cambridge Philos. Soc. **45**, 678 (1949).

[79] H. Saito and T. Hyodo, Phys. Rev. B **60**, 11070 (1999).

[80] A. A. Kvitsinsky, J. Carbonell, and C. Gignoux, Phys. Rev. A **46**, 1310 (1992).

[81] E. M. Purcell, *Electricity and Magnetism 2nd edition, Berkley Physics Course. Volume 2*, McGrow-Hill, Inc. New York.

[82] M. H. Yam, P. O. Egan, W. E. Frieze, V. W. Hughes, Phys. Rev. A **18**, 350 (1978).

[83] W. R. Nelson, H. Hirayama and D. W. O. Rogers, THE EGS4 CODE SYSTEM, (1985), SLAC-265.